Structural phase transitions and proton conduction in $M_3H(SO_4)_2$ ($M = NH_4^+$, K^+) compounds with hydrogen disorder

Von der Fakultät für Georessourcen und Materialtechnik
der Rheinisch-Westfälischen Technischen Hochschule Aachen

zur Erlangung des akademischen Grades eines
Doktors der Naturwissenschaften

genehmigte Dissertation
vorgelegt von Dipl.-Min.

Yoo Jung Sohn

aus Seoul, Südkorea

Berichter: Univ.-Prof. Dr. rer. nat. Gernot Heger
Univ.-Prof. Dr. rer. nat. Georg Roth
apl. Prof. Dr. rer. nat. Ullrich Englert

Tag der mündlichen Prüfung: 26. April 2012

Diese Dissertation ist auf den Internetseiten der Hochschulbibliothek online verfügbar.

Acknowledgements

It is a great pleasure for me to thank those who made this thesis possible at all, from the initial to the final level.

In the first place I would like to express my deepest gratitude to Prof. Dr. Gernot Heger for his supervision, encouragement, guidance and support throughout the work. His everlasting enthusiasm in research kept me motivated on the subject. He is the one who helped me to set myself a target and to strive for it. Nevertheless his long-range order perspective prevented me from becoming narrow-minded in the scientific as well as non-scientific world. Many thanks also for the opportunity he gave me to work as a scientific co-worker at the Institut für Kristallographie of the RWTH Aachen.

I gratefully acknowledge Prof. Dr. Georg Roth for his valuable advice in many scientific discussions and kind supervision in conductivity measurements. His helpful guidance to challenging conferences and workshops during my doctoral studies allowed me to obtain well-balanced nourishment. I am among his many other students who appreciate his unique humour that rearranged our cubic or hexagonal close-packed heads. Heartily thanks also for hiring me as a scientific co-worker after my scholarship had ended; by this, he spared me some additional wrinkles on my forehead.

Special acknowledgements are also conveyed to Prof. Dr. Theo Hahn and Prof. Dr. Helmut Klapper for their continued interest in my doctoral studies and valuable advice. I am most honoured to have had the opportunity to attend their lectures in symmetry of crystals and crystal growth, since they are true experts in their field.

To Dr. Karine Sparta, I am indebted to her more than she can imagine. About her great support in many details throughout my work at the Institut für Kristallographie I could write another thesis. With her sunshiny character, she, in fact, changed many cloudy and gloomy days of Aachen to sunny ones. She also opened my eyes for beautiful beads artwork and she is actually making her first 3D fullerene pendant for her necklace.

My further heartfelt appreciation goes to Dr. Sebastian Prinz for his useful advice and practical help for X-ray laboratory works. He probably hides a cryostat somewhere

in his body, because he always managed to keep cool for error messages popping up out of the blue. His optimistic choice of beer enriched my beer to-drink-list but also to-drop-list. However, I am sure that it was his optimism that carried him to the new opportunities.

Collective and individual acknowledgements are also owed to my further colleagues at the Institut für Kristallographie. To Dipl.-Min. Ellen Nowack, I am deeply thankful for her careful assistance in so many ways. Her open-hearted character pulls people like a magnet, so that we sometimes had to deal with the traffic jam in front of her office. I am also very much thankful to Angelika von Berg for her practical support in many lab works. With her, I enjoyed, above all, the Monday morning coffee break, because we both need stronger coffee on Mondays. Having spoken about the coffee break, I appreciate further coffee-colleagues very much for the joyful breaks we shared in the morning. Sometimes, on their hilarious jokes, I really had to struggle with fresh coffee in my mouth not to spit it out or swallow it at the wrong moment. To Erika Appel, I would like to thank for her practical help in office works. I also enjoyed her vivid report on her lovely grandchildren. Further thanks go to Katharina Siebericchs for her useful guides in the library. Her charming character was always welcome to every celebration that we had. To Dipl.-Ing. Franz-Dieter Scherberich, I would like to thank him for all the lab works that would have been impossible without his top-class support and fresh ideas. I still have to learn from his very well balanced work and holiday system, so I can manage a long-term healthy life with such effectiveness that he has. I also benefited by outstanding help from Rolf Becker. His precise and creative working style, from the preparation to the final, made all the fine arts of my doctoral studies possible. He is in so many ways multi-talented and I am especially keen on his music and paintings. I hope he can publish his precious treasures one day, so that more people can admire them. To Egon Heidrich, I would like to thank for his quick help in many practical ways and for his pleasant wit and humour. His decent cooking guide improved my poor German dishes. To Josef Ernst, I am very grateful for his practical support in using and calibrating furnaces. I also appreciate his informative advice for balanced diet and sports. I also thank Bernd Laschet for his rapid operation to order liquid nitrogen even if I had to order it once on a Friday afternoon. He is the vital evidence that there are people working on Friday afternoons. My further appreciation goes to Dipl.-Min. Jörg Thar who helped me with single-crystal growth and gave me valuable advice. His great organizing skills and cheerful character are really admirable. I wish him all the best for his future. Dipl.-Phys. Jan Simons was an excellent troubleshooter in many irritating

computer problems and I also appreciate his company as another postgraduate student. I am still waiting for the top secret recipe of his extraordinary Glühwein (hot spiced wine). I would also like to thank Dr. Lars Peters for his willingness and kindness to read and check this thesis from beginning to the end. Although his time schedule is horribly packed, he somehow managed to go through this thesis with a fine-tooth comb. Without his help, this thesis would have ended up in a nice pot at a flower shop, next to roses and lilies with my ever so flowery writings. Many thanks also go to the further co-workers at the Institut for their excellent teamwork.

Further special thanks go to Dr. Martin Meven for his great support in single-crystal neutron diffraction at the FRM II in Munich. He was always patient with my endless questions, no matter if they came in-situ or via numerous emails, helpful answers were given promptly all the time. I really and truly benefited by his outstanding skills in collecting, sorting and presenting data. He belongs to the fascinating scientists who understand what they are doing.

At this point in my acknowledgements, I would like to thank FRM II for the allowed beam time with just in time excellent weather in Munich. Furthermore, I would like to convey my sincere gratitude to the RWTH Aachen for the granted scholarship in the form of the Graduiertenförderung.

Words fail me to express my deepest appreciation to my dear family and friends. The more I think about my parents, the more I realize how fortunate I am to be their daughter. My father is one who has been teaching his children how to catch a fish rather than give them one directly. This helped me a lot especially in tough times, because I could sit back with the fishing rod in my hand and wait for the fish to bite. The soothing and encouraging words from my mother have enchanted me throughout my whole life, so that I now possess the ability to see the light at the end of the tunnel. I am most privileged to have two wonderful sisters who I can share my laughs and tears with. They have always been very honest with me and gave me their subjective as well as objective opinions from my hair styling to my behaviour disorder. To my parents-in-law, I would like to thank them wholeheartedly for their great love and support ever since I became their family member. They gave me strength through plenty of long-distance calls and I really appreciate every visit they made to Aachen. After all, I have to confess, that there are family members who had to suffer most from my doctoral studies, and ironically, they are the ones who are the nearest to my heart. I thank my wonderful husband for bearing with me going through countless phase transitions and for being always there for me and our children. To the gifts from heaven, whether my

two beautiful sons realize it or not, I am the happiest mom in the world. In my daily work, I have been blessed with my dear friends here in Aachen as well as abroad. I thank all those who helped me with practical and unseen hands and open hearts and ears during my doctoral studies.

Finally, I thank Thee for Thy love.

Kurzfassung

Triammoniumhydrogendisulfat $(NH_4)_3H(SO_4)_2$ (TAHS) gehört zu der bekannten Strukturfamilie mit der Zusammensetzung $M_3H(XO_4)_2$ ($M = NH_4^+$, K^+, Rb^+, Cs^+; $X = S$, Se). Diese Verbindungen zeichnen sich durch eine starke Wasserstoffbrückenbindung zwischen zwei XO_4^{2-}-Ionen aus und zeigen Superprotonenleitfähigkeit in der Hochtemperaturphase. TAHS hat fünf sukzessive strukturelle Phasenübergänge. Obwohl dies schon seit mehreren Jahrzehnten bekannt ist, wurde wenig über die Kristallstrukturen und strukturellen Phasenübergänge in Bezug auf Wasserstoff-Fehlordnung untersucht. Daher liegt das Hauptthema dieser Dissertation darin, die spezifische Rolle der Wasserstoff-Fehlordnung anhand von Neutronenbeugung zu untersuchen. Für diesen Zweck wurden bis zu einige Zentimeter große Einkristalle aus der Lösung gezüchtet. Mittels temperaturabhängiger Röntgenpulverdiffraktion sowie DSC/TG-Untersuchungen wurden die einzelnen Phasenübergänge verifiziert. Als Ergebnis wurden die Phasenübergangstemperaturen beim Abkühlen und Aufheizen bestimmt, die mit den Literaturwerten sehr gut übereinstimmen. Außerdem wurden die Phasenübergänge mit typischen Merkmalen als Phasenübergänge erster oder zweiter Ordnung charakterisiert.

Die Kristallstrukturanalyse von TAHS für verschiedene Phasen (I bis V) wurde mittels Röntgen- und Neutronenbeugung an Einkristallen durchgeführt. In der Hochtemperaturphase I oberhalb von 413 K kristallisiert TAHS in der rhomboedrischen Raumgruppe $R\bar{3}m$. Durch die fehlgeordneten Sauerstoffatome wird ein pseudo-hexagonales Netzwerk der Wasserstoffbrücken von SO_4–H–SO_4 in der (001)-Ebene gebildet. Zusätzlich wurde eine Aufspaltung der H-Atompositionen in dieser O–H–O-Bindung anhand einer Differenz-Fourier-Analyse vorgeschlagen. Die teilbesetzten Protonenlagen ermöglichen eine Protonendiffusion in der (001)-Ebene. Außerdem deuten die kurzen H–H-Abstände zwischen NH_4 und SO_4–H–SO_4 sowie eine Darstellung der Protonendichte um die beteiligten NH_4-gruppen auf einen möglichen zusätzlichen Protonenaustausch zwischen NH_4 und O–H–O-Bindung hin. Für die Ammoniumgruppen der Hochtemperaturphase I wurde eine reorientierende Bewegung aufgrund ihrer thermischen

Ellipsoide und der Rigid-body-Analyse vorgeschlagen. Der I/II-Hochtemperaturphasenübergang ist ein Phasenübergang erster Ordnung und zeigt eine deutliche Hysterese. Die Raumtemperaturphase II ist monoklin mit der Raumgruppe $C2/c$, und isolierte $(SO_4)H(SO_4)$ Dimere mit einer symmetrischen O–H–O-Bindung werden gebildet. Die Wasserstoff-Atompositionen wurden dabei wie in der Hochtemperaturphase I durch ein Split-Atom-Modell verfeinert. Weiterhin gibt es zwei symmetrieunabhängige NH_4-Gruppen in Phase II. Diese bilden konkurrierende N–H$\cdots$O-Wasserstoffbrückenbindungen zu den benachbarten Sauerstoffatomen von SO_4. Bei 265 und 141 K handelt es sich um Phasenübergänge zweiter Ordnung. Beide Phasen, III und IV, haben die gleiche monokline Raumgruppensymmetrie ($P2/n$), wobei die Elementarzelle für die Phase IV in **b**-Richtung verdoppelt ist. Der IV/V-Phasenübergang bei 133 K beim Abkühlen ist von erster Ordnung. Mit Röntgenbeugungsdaten wurde eine trikline Raumgruppe ($P\bar{1}$) für die Kristallstruktur von TAHS-V festgestellt. Bei den Einkristall-Neutronenbeugungsmessungen wurde dementsprechend eine Verzwillingung bei diesem Phasenübergang beobachtet. Eine zunehmende Protonenordnung mit sinkender Temperatur wurde für die Tieftemperaturphasen III bis V bestätigt. Mittels Röntgenpulverdiffraktion wurde der V/VII-Phasenübergang bei 70 K beim Abkühlen als ein Phasenübergang erster Ordnung charakterisiert. Dabei entstehen zusätzliche Reflexe, die eine Verdoppelung der Elementarzelle in allen kristallographischen Richtungen aufweisen.

Parallel zu den drei unterschiedlichen monoklinen Richtungen wurden die Leitfähigkeitsmessungen in dem Temperaturbereich von RT bis 441 K durchgeführt. Dabei wurde eine Anisotropie der Leitfähigkeit in der monoklinen Phase festgestellt, wobei eine ausgeprägte hohe Protonenleitfähigkeit in der (001)-Ebene für die Hochtemperaturphase von TAHS beobachtet wurde.

Für das Referenzsystem, $K_3H(SO_4)_2$ (TKHS), wurde der Hochtemperaturphasenübergang mit DSC/TG und Röntgenpulverdiffraktion untersucht. Eine analoge rhomboedrische Hochtemperaturphase wurde beobachtet, die aber gleichzeitg von einer thermischen Zersetzung der Probe begleitet wurde. Im Unterschied zu TAHS zeigt der Hochtemperaturphasenübergang von TKHS eine ausgeprägte Übergangskinetik.

Abstract

Triammonium hydrogen disulphate $(NH_4)_3H(SO_4)_2$ (TAHS) belongs to the well known structure family of compounds with the general formula $M_3H(XO_4)_2$ ($M = NH_4^+$, K^+, Rb^+, Cs^+; $X = S^{6+}$, Se^{6+}). The characteristics of these compounds are the strong hydrogen bonds between two XO_4^{2-} ions and the superprotonic conductivity in the high-temperature phases. TAHS undergoes five successive structural phase transitions. Although the rich polymorphism of TAHS has been established for several decades, little is known about its crystal structures and structural phase transitions with respect to the H-ordering. Therefore, the main focus of this dissertation was to investigate the specific role of the H-ordering using single-crystal neutron diffraction. For this purpose, single crystals were grown from aqueous solution up to several cm in size. For the studies of phase transitions, temperature-dependent X-ray powder diffraction as well as DSC/TG were carried out on polycrystalline samples. As a result, the phase transition temperatures were determined on cooling and heating. These temperatures are in close agreement with the literature values. Moreover, the phase transitions are characterized as either first- or second-order phase transitions due to their observed specific features.

The crystal structure analyses of TAHS for different phases (I to V) were performed using single-crystal X-ray and neutron diffraction. In the high-temperature phase I above 413 K, TAHS crystallizes in the rhombohedral space group $R\bar{3}m$. A pseudo-hexagonal network of SO_4–H–SO_4 hydrogen bonds is formed in the (001) plane by the disordered O atoms. In addition, a difference Fourier map suggests a splitting of H-atom positions in these O–H–O hydrogen bonds. The only partially occupied H-atom positions enable proton diffusion in the (001) plane. Moreover, possible supplementary proton exchange between NH_4 and SO_4–H–SO_4 was suggested according to the short H–H distances and the proton density around the involved NH_4 groups. Regarding the thermal ellipsoids of the ammonium groups as well as the rigid-body analysis, reorientational motion of these groups is assumed in phase TAHS-I. The I/II-phase transition is of first-order and shows a clear hysteresis. The room-temperature phase

II is monoclinic with space group $C2/c$ and features isolated $(SO_4)H(SO_4)$ dimers with symmetric O–H–O hydrogen bonds. Like in the high-temperature phase I, the H-atom positions are split. There are two symmetrically independent NH_4 groups which form competing N–H$\cdots$O hydrogen bonds with O atoms of the surrounding SO_4 groups. At 265 and 141 K, TAHS undergoes second-order phase transitions. Both phases III and IV have the same monoclinic space group symmetry ($P2/n$), however, the unit cell is doubled in **b** direction in phase IV. The IV/V-phase transition at 133 K on cooling is of first-order. Using X-ray diffraction data, it was shown that TAHS-V crystallizes in the triclinic space group $P\bar{1}$. The corresponding twinning was observed in single-crystal neutron diffraction studies. For the low temperature phases III to V, an increase of H-ordering with decreasing temperature is observed. According to X-ray powder diffraction, the V/VII-phase transition at 70 K on cooling indicates a first-order character with a doubling of the unit cell in all crystallographic directions.

Conductivity measurements were performed in the temperature range between room temperature and 441 K parallel to the three different monoclinic directions. There is an anisotropy in the proton conduction in the room-temperature phase, whereas a distinct high proton conduction exists in the (001) plane for the high-temperature phase of TAHS.

For the reference system, $K_3H(SO_4)_2$ (TKHS), the high-temperature phase transition was investigated by DSC/TG and X-ray powder diffraction. An analogous rhombohedral high-temperature phase was observed along with a thermal decomposition. Contrary to TAHS, the high-temperature phase transition of TKHS shows pronounced transition kinetics.

Contents

1 Introduction **1**

1.1 Crystal structure analysis with X-ray and neutron diffraction methods . 2

1.2 Structural phase transitions 4

1.3 Literature review and motivation 6

2 Sample preparation **13**

2.1 Single crystal growth 13

2.2 Preparation of polycrystalline samples (powders) 14

3 Experimental **17**

3.1 X-ray single-crystal diffraction 17

3.2 X-ray powder diffraction 19

3.3 Neutron single-crystal diffraction 21

3.4 Differential scanning calorimetry/Thermogravimetry 22

3.5 Conductivity measurements 23

4 Crystal structure of $(NH_4)_3H(SO_4)_2$ **25**

4.1 High-temperature phase I 25

4.2 Room-temperature phase II 39

4.3 Low-temperature phase III 47

4.4 Low-temperature phase IV 61

4.5 Low-temperature phase V 75

5 Structural phase transitions in $(NH_4)_3H(SO_4)_2$ **89**

5.1 Differential scanning calorimetry/Thermogravimetry 90

5.2 Temperature-dependent X-ray powder diffraction 92

5.3 Temperature-dependent neutron single-crystal diffraction 98

6 Conductivity measurements on $(NH_4)_3H(SO_4)_2$ 107

7 Investigation on the reference system, $K_3H(SO_4)_2$ 113

7.1 Differential scanning calorimetry/Thermogravimetry 113

7.2 Temperature-dependent X-ray powder diffraction 118

8 Conclusion 121

References 125

Lebenslauf 129

Chapter 1

Introduction

Polymorphism is an interesting feature of a crystalline material where there exist different crystal structures without a change of its chemical composition. Since many material properties are closely related to the crystal structure, it is very helpful to understand how the atoms within the unit cell are arranged and how they behave at different conditions as e.g. temperature, pressure. In the case of polymorphism, verifying the driving force, the mechanism of structural phase transitions, also belongs to the fundamental studies. The main purpose of this dissertation is to verify the polymorphism of $M_3\mathrm{H}(\mathrm{SO}_4)_2$ ($M = \mathrm{NH}_4^+$, K^+) compounds for a better comprehension with regard to both, the crystal structure in each phase, and the mechanism of the structural phase transitions. In this introductory chapter, the principle of crystal structure analysis with diffraction methods is briefly summarized, and the difference between X-ray and neutron diffraction due to their scattering properties is discussed. Then, a short comment is given on the thermodynamical classification of phase transitions and the structural phase transitions of order and disorder type are introduced. Finally, a literature review is given, from which the current state of research and the motivation for this dissertation is deduced. In the experimental part, the sample preparation including crystal growth and the various measurement methods used are explained and presented. The results are then divided into crystal structure analysis and structural phase transitions. The outcome of conductivity measurements is reported in the end. The final chapter is attributed to the conclusion.

1.1 Crystal structure analysis with X-ray and neutron diffraction methods

A crystal is a homogeneous and anisotropic solid material in which atoms, ions or molecules are arranged periodically in all three dimensions. Analysis of crystal structure therefore means, to describe the exact arrangement of those chemical components within a unit cell that is the smallest building block of a crystal. This unit cell can be repeated infinitely through translation, spanning a crystal lattice in three dimensions. The three-dimensional periodicity of a crystal enables radiation interference which was discovered for the first time by Max von Laue in 1912. X-ray and neutron diffraction methods for crystal structure analysis are based on the fact that those wavelengths have the same order of magnitude as interatomic distances, and a beam that reaches a crystal diffracts into different directions, delivering many observable reflections. The energy of incident and scattered beams remains the same in this process, therefore it is a form of elastic scattering. To observe a reflection after a beam strikes the sample, a certain condition expressed by Bragg's law must be fulfilled:

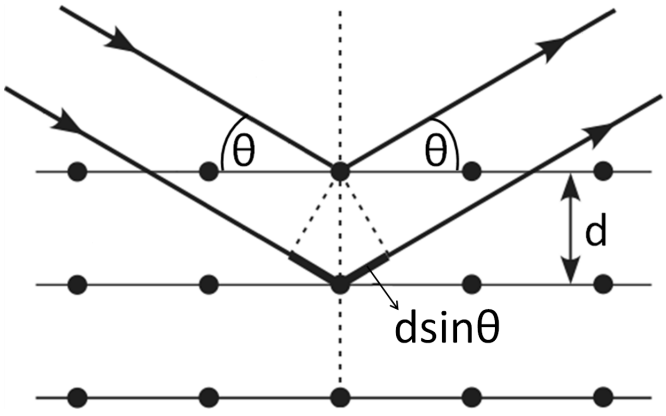

Figure 1.1: Diffraction of an incident beam at the lattice planes.

$$n\lambda = 2d \sin \Theta$$

where n is an integer, λ is the wavelength of the incident beam, d is the spacing between diffracting planes, and Θ is the incident/scattering angle. Constructive interference can only be achieved, if the path difference between the waves is an integer multiple n of the incident wavelength λ. In those diffraction methods, where the wavelength λ remains constant, the angle Θ can vary to obtain different d-spacings. In order to calculate the scattering angle Θ, information about the crystal system and the lattice parameters of

the unit cell for the measured crystal is needed. The d-spacing can then be formulated in terms of hkl-indices, for example, in the case of the monoclinic crystal system:

$$\frac{1}{d^2} = \frac{h^2}{a^2 \sin^2 \beta} + \frac{k^2}{b^2} + \frac{l^2}{c^2 \sin^2 \beta} - \frac{2hl \cos \beta}{ac \sin^2 \beta}$$

For any set of hkl-indices, the d-spacing can be determined, and using the Bragg equation above, the scattering angle Θ can be obtained. Combination of those two equations provides the quadratic form of the Bragg equation. In the monoclinic crystal system the following applies:

$$\sin^2 \Theta = \frac{\lambda^2}{4}\left(\frac{h^2}{a^2 \sin^2 \beta} + \frac{k^2}{b^2} + \frac{l^2}{c^2 \sin^2 \beta} - \frac{2hl \cos \beta}{ac \sin^2 \beta}\right)$$

Further crystal structure information can be obtained from the reflection intensity which is proportional to the square of the amplitude of the scattered wave for a crystal:

$$I \sim |F|^2$$

For each reflection hkl, the structure factor is calculated through the summation over all atoms in the unit cell as follows:

$$F_{(h,k,l)} = \sum_{j=1}^{N} f_{(j)} exp[2\pi i(hx_{(j)} + ky_{(j)} + lz_{(j)})]$$

where N is the number of atoms in the unit cell and $f_{(j)}$ is the atomic form factor of the j-th atom in the case of X-ray diffraction. It is the Fourier transformed electron density of the scattering atom and its amplitude relates to the atomic number, Z. The atomic form factor decreases with increasing diffraction angle, Θ. Neutrons, on the other hand, interact with the nucleus of the atom and the amplitude of this scattering is expressed with the scattering length, b, which is independent of the scattering angle and remains constant. Since with diffraction experiments only the absolute value of the structure factor can be derived from the intensity, the phase information is lost, known as the phase problem of crystallography. The structure solution of a crystal hence refers to the solution of this phase problem. There are several methods to solve the phase problem, and once it is solved, the electron density can be derived from Fourier synthesis. From this electron density, atom positions in a unit cell can be obtained, building an initial structure model. With this model, the crystal structure can be further refined by fitting the atomic positions and the ADPs (Atomic Displacement Parameters). This refinement process is repeated until a good and reasonable agreement between observed

and calculated $F, F^2 or I$ values is reached. The crystallographic R-factor is a measure of this agreement between the calculated model and the observed diffraction data:

$$R = \frac{\sum ||F_{obs}| - |F_{calc}||}{\sum |F_{obs}|}$$

The weighted R-factor is often used in the least-squares refinement and by using a reasonable weighting scheme, the refinement result improves:

$$wR_2 = \sqrt{\frac{\sum w(F_{obs}^2 - F_{calc}^2)^2}{\sum w(F_{obs}^2)^2}}$$

X-ray diffraction can be described as an interaction between X-rays, electromagnetic waves, and the electron shell of the atom, whereas in case of neutron diffraction, neutrons interact directly with the nucleus of the atom. This different scattering process of neutron diffraction provides other complementary information in the field of crystal structure analysis. The scattering length of neutrons varies individually, even from isotope to isotope, and this also enables to distinguish between two neighbouring elements in the periodic table. Hydrogen, for example, owns a relatively large scattering length for neutrons, whereas light atoms such as hydrogen cannot be effectively detected with X-ray diffraction. Therefore, a precise localization of protons is possible with neutron diffraction. A further important application of neutron diffraction is the investigation of the magnetic structure of a crystal, due to the fact that neutrons, though uncharged, have a magnetic moment and can be diffracted by three-dimensionally ordered magnetic moments. To carry out an experiment with neutrons, a relative large size or amount of sample is typically needed and permission for beam time at a research reactor is required as well.

1.2 Structural phase transitions

The study of structural phase transitions is, to examine the initial and transformed crystal structures before and after a phase transition. The relation between those two structures provide information about the mechanism of the transformation. During a phase transition, thermodynamic quantities, for example, entropy, volume, heat capacity etc. may undergo discontinuities. Ehrenfest classified phase transitions through the relation between the thermodynamic discontinuity and the Gibbs free energy function. A first-order phase transition is characterized by discontinuous changes in the

first derivatives of the Gibbs free energy:

$$\left(\frac{\partial G}{\partial P}\right)_T = V \qquad \left(\frac{\partial G}{\partial T}\right)_P = -S$$

A difference in volume and entropy (equivalent to the occurrence of a latent heat of transition) occurs during a first-order phase transition. The drastic structural changes, existence of hysteresis and coexistence of both phases at the transition are characteristics of a first-order phase transition. The second derivatives of the free energy may be expressed as:

$$\left(\frac{\partial^2 G}{\partial P^2}\right)_T = \left(\frac{\partial V}{\partial P}\right)_T = -V\beta$$

$$\left(\frac{\partial^2 G}{\partial P \partial T}\right) = \left(\frac{\partial V}{\partial T}\right)_P = V\alpha$$

$$\left(\frac{\partial^2 G}{\partial T^2}\right)_P = -\left(\frac{\partial S}{\partial T}\right)_P = -\frac{C_p}{T}$$

where β, α and C_p are the compressibility, volume thermal expansivity and heat capacity, respectively. During a second-order phase transition, the volume and entropy remain continuous while the compressibility, thermal expansivity and heat capacity undergo a discontinuous change. The space group symmetries of the two phases are related as a group and subgroup in a second-order transition and the low-symmetry phase approaches the high-symmetry phase continuously throughout the transition. Landau proposed a theory and introduced the order parameter, η. As shown in Fig. 1.2, the order parameter decreases continuously with increasing temperature and becomes zero at the transition temperature. In other words T_c of a second-order transition corresponds to the onset of an ordering process. This phenomenon can be described with a parameter known as a critical exponent (β) in the following equation:

$$\eta \sim |T - T_c|^{\beta} \qquad \text{(for} \quad T < T_c)$$

In a classical model β has the value of 1/2 and in the case of tricritical behaviour 1/4. However, experimental values of β can vary widely and they also depend on the dimensionality. For example, β of 0.125 has been reported for a two-dimensional model whereas for a three-dimensional model $\beta = 0.33$ is known.

For the study of phase transitions there are many different methods, where the change of physical quantities can be measured and analysed. In order to gain specific structural information related to a phase transition, methods such as X-ray and neutron diffraction at various temperatures can provide essential knowledge about structural

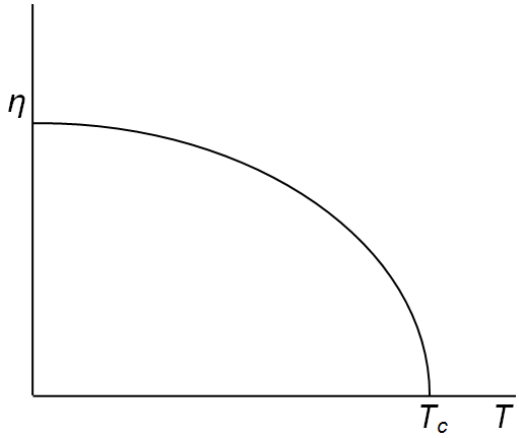

Figure 1.2: Variation of order parameter in a second-order phase transition.

phase transitions. The study of atomic arrangements within a certain unit cell can explain whether, for example, positional or orientational changes take place during a phase transition, whereas from the temperature-dependent observation of ADPs a distinction between statical or dynamical disordering can be made.

1.3 Literature review and motivation

The well known family of compounds with the general formula $M_3\mathrm{H}(X\mathrm{O}_4)_2$ ($M = \mathrm{NH}_4^+$, K^+, Rb^+, Cs^+; $X = \mathrm{S}$, Se) is characterized by the strong hydrogen bond between two $X\mathrm{O}_4^{2-}$ ions forming a $(X\mathrm{O}_4)\mathrm{H}(X\mathrm{O}_4)$ dimer. The dynamically disordered hydrogen bonds in these compounds build a network in the high-temperature phases and allow for a superprotonic conductivity [1]. Since the first dielectrical studies of triammonium hydrogen disulphate $(\mathrm{NH}_4)_3\mathrm{H}(\mathrm{SO}_4)_2$ (TAHS) showed five successive structural phase transitions at standard atmospheric pressure [2, 3, 4], there has been a constant interest in investigating TAHS concerning the crystal structure of the different phases and their physical as well as chemical properties using various experimental methods. The reported six different phases of TAHS at 1 atm are shown in the following with their denotation and the phase transition temperatures:

$$\mathrm{VII} \overset{63\mathrm{K}}{\longleftrightarrow} \mathrm{V} \overset{133\mathrm{K}}{\longleftrightarrow} \mathrm{IV} \overset{141\mathrm{K}}{\longleftrightarrow} \mathrm{III} \overset{265\mathrm{K}}{\longleftrightarrow} \mathrm{II} \overset{413\mathrm{K}}{\longleftrightarrow} \mathrm{I}$$

There is a further phase VI found under higher pressure $> \sim 5$ kbar [5] and the phases VI and VII are suggested to be ferroelectric [6]. The pressure-temperature phase diagram of TAHS is shown in Fig. 1.3.

Crystal structure analyses of TAHS have been performed so far for phases I, II, III,

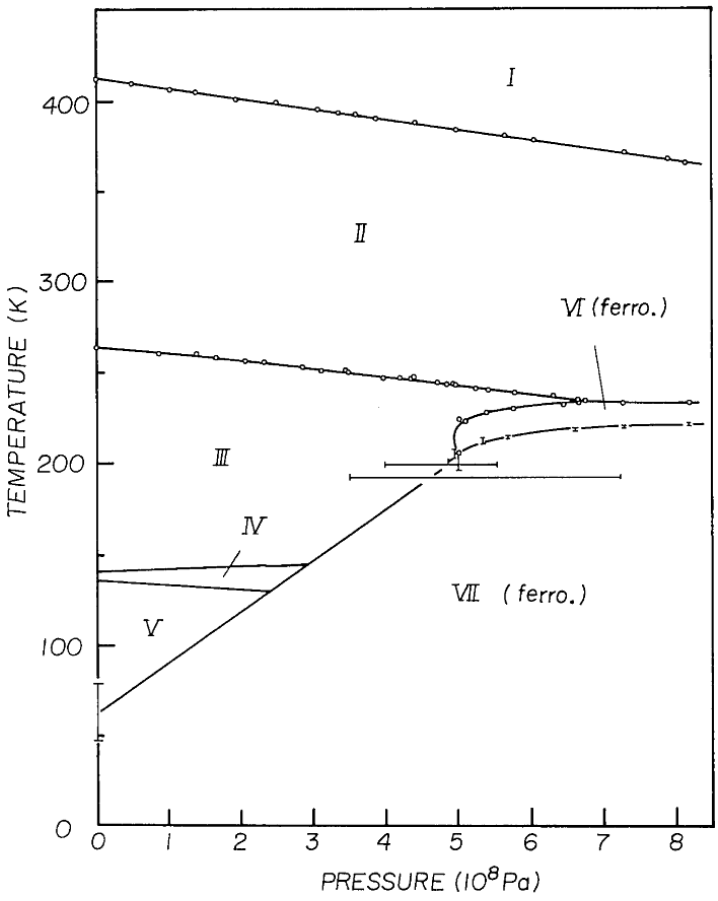

Figure 1.3: Pressure-temperature phase diagram of TAHS [3].

IV and V using X-ray and neutron diffraction [7, 8, 9, 10]. The high-temperature phase I crystallizes in space group $R\bar{3}m$ (No.166 [11]) [7, 9] and is a superprotonic conductor ($10^{-2} \leq \sigma_{(001)} \leq 10^{-1}$ S $\cdot$ cm^{-1}) [12, 13]. In contrast to the low-temperature phases, in which isolated $(SO_4)H(SO_4)$ dimers are formed through O–H–O hydrogen bonds, a two-dimensional hydrogen bond network exists perpendicular to c in the high-temperature phase I of TAHS. The H atoms of the hydrogen bonds in the (001) plane of the hexagonal lattice are dynamically disordered and their sites are not fully occupied. Therefore, a fast proton diffusion takes place between symmetrically equivalent H-atom positions. The O atom of these O–H–O hydrogen bonds is also disordered and split. Instead of being located on a threefold axis (6c-Wyckoff position), it occupies the 18h-Wyckoff position with an occupation probability of 1/3 [9]. Besides, the ammonium groups of the high-temperature phase I are also disordered. Another interesting aspect regarding the high-temperature phase I comes from the nuclear magnetic resonance (NMR) studies [14]. According to it, a chemical exchange between the ammonium protons and

the protons involved in the hydrogen bond of SO_4–H–SO_4 has been suggested. This observation also supports the idea of ammonium protons being involved in the proton conduction of TAHS-I as supposed by Merinov *et al.* [15]. One last thing that should be taken into careful consideration concerning the high-temperature phase is that there is a certain ambiguity of additional high-temperature phase transitions of TAHS reported earlier [13, 16]. From those reports it is not clear whether the results are reproducible. The additional phase transitions were observed at temperatures close to or even higher than the chemical decomposition temperature of TAHS. Hence, those reported results should be interpreted with caution.

The room-temperature phase II is monoclinic with centrosymmetric space group $C2/c$ (No. 15) and characterized by a strong hydrogen bond forming isolated $(SO_4)H(SO_4)$ dimers [8]. The reorientational behaviour of the ammonium groups of TAHS requires further treatment and analysis, since the ordering of those ammonium groups plays a significant role in the four successive structural phase transitions at lower temperatures [17].

The crystal structure of low-temperature TAHS-phases has been investigated so far only by X-ray diffraction [8]. The same monoclinic space group $P2/n$ (No. 13) is suggested for both the low-temperature phases III and IV with very little differences in lattice parameters. For phase V the triclinic space group $P\bar{1}$ is proposed [8]. Up to now, there has been no structural investigation for the phase VII of TAHS, however, from the statement of the phase VII being ferroelectric [4], the space group should be non-centrosymmetric.

The ammonium groups with their rotational disorder directly affect the structural phase transitions of TAHS, and furthermore, they are possibly involved in the proton conduction in the high-temperature phase. Hence, comparative studies of the reference system, tripotassium hydrogen disulphate $K_3H(SO_4)_2$ (TKHS) can help to elucidate the principal task of ammonium groups within the different TAHS phases. Since the ionic radii of NH^+ (1.43 Å) and K^+ (1.38 Å) are very similar, analogies between the crystal structures of TKHS and TAHS can be assumed especially at high temperatures. However, compared to TAHS, there has been relatively little information about TKHS regarding its phase transitions and crystal structures. Moreover, the findings are partly disputed.

The existence of the high-temperature phase is particularly controversial. The first observation of a possible high-temperature phase transition is reported in 1904 using

a polarizing microscope [18]. On heating, TKHS crystals became cloudy and hence a detailed analysis was impossible. However, a few clear spots on the sample indicated an uniaxial system under polarized light, which disappeared again on cooling. The further observed anomalies above room temperature are listed and compared in Table 1.1.

Table 1.1: Observed anomalies of TKHS above room temperature.

Ref.	Phase transition temperature [K]	Decomposition temperature [K]	Experimental method	Reproducibility
[19]	463, 500	543	DSC	not given
[20]	478	535	DSC	unknown
[21]	not observed	479	DSC	unknown
[22]	463	not given	Dielectric permittivity Magnetic susceptibility	given
[23]	481	522, 543	DSC	unknown
[24]	457	468, 473	X-ray diffraction	unknown
[25]	463	480	X-ray diffraction	given

The differences between those results may be explained by different sample types (single crystal, polycrystalline), preparation techniques of the sample, heating rates and also the anomalously slow kinetics of the structural transformation of TKHS. There is a certain difficulty in determining the high-temperature phase transition of TKHS, since, if there is any, the high-temperature phase exists only in a very small temperature range and the decomposition of the sample also begins more or less at the same time. For such a case, verification of the structural phase transitions is not easy due to the change in the chemical composition of the sample.

The crystal structure analysis of TKHS with single-crystal X-ray diffraction yielded a trigonal symmetry $R\bar{3}m$ for the high-temperature phase and a monoclinic symmetry $C2/c$ for the room-temperature phase [24, 26], which are isostructural with other members of the $M_3\mathrm{H}(X\mathrm{O}_4)_2$ family. In the high-temperature phase the O atoms forming O–H–O bonds are dynamically disordered. This phenomenon also leads to the formation of a dynamically disordered hydrogen bond network [24]. The conductivity measurements at 471 K and at 524 K yielded σ = 1.68 x 10^{-3} and σ = 2.19 x 10^{-2} S $\cdot$ cm^{-1}, respectively [19], and showed a superprotonic character similar to other $M_3\mathrm{H}(X\mathrm{O}_4)_2$ compounds exhibit in their high-temperature phases. The characteristic feature of the room-temperature phase is the hydrogen bonding linking two SO_4-tetrahedra as a $(\mathrm{SO}_4)\mathrm{H}(\mathrm{SO}_4)$ dimer. Both with X-ray and neutron diffraction studies, the H atom po-

sition in this O–H–O bonding was observed to be split [27]. Below room temperature, no other structural phase transitions of TKHS were found at atmospheric pressure. However, an interesting phenomenon was observed with decreasing temperature. The double minimum potential of the H atom in the O–H–O hydrogen bond becomes a single one at $\sim$ 100 K without any structural phase transition (see Fig. 1.4 [28]). The O–O distance shrinks with decreasing temperature due to the lattice contraction, and at $\sim$ 100 K, the distance of double minimum positions of the H atom drops to zero and the critical bond length was observed as $r_c(H) = 2.473\,(3)$ Å from X-ray diffraction data [28]. Three further phases III, IV and V have been found under higher pressure and at low temperatures according to Raman scattering measurements [29].

Among the various studies carried out so far, there still remain certain ambiguities regarding the structural investigation of the phase transitions of $M_3H(SO_4)_2$ ($M = NH_4^+$, K^+) compounds. Some of the findings need more explicit verification such as the existence of additional high-temperature phases in TAHS and the high-temperature phase transition in TKHS. Furthermore, a careful and strict inquiry is needed for conductivity measurements in the high-temperature phase to be absolutely sure that the sample does not undergo thermal decomposition during the experiments. In case of TAHS, half of the atoms consist of protons and the disorder of these protons is the main reason for the rich polymorphism of this compound. Therefore, to pinpoint the proton positions and to describe their behaviour properly, an investigation of the crystal structure with neutron diffraction is inevitable. The crystal structure analyses until now, have mostly been done with X-ray diffraction methods, where electron density of the sample can be obtained. The single electron of the H atom which takes part in the chemical (covalent) bonding is thus shifted from the proton position to the bonding partner, mostly oxygen. This results in a deformation of the electron density distribution and a precise localization of the proton is difficult with X-ray diffraction since X-rays interact with electrons and light atoms like H have very little contribution as well. On the other hand, neutrons directly interact with atomic nuclei and hence a precise determination of the proton position is possible with reference to that protons are normal scatterers comparable to other atomic nuclei. In addition, with temperature dependent X-ray powder diffraction series in the whole temperature range, covering the six different phases of TAHS, the change of the lattice parameters can be analysed in detail and the phase transitions can be observed and characterized. Besides, the difference between the crystal structures of TAHS-III and -IV is in question, and a possible modulation in the crystal structure

of TAHS in some phases [8] needs further investigation. The disagreements between different DSC (Differential Scanning Calorimetry) measurements can also be improved by choosing the experimental conditions more carefully. Altogether, the above contemplated issues as well as not yet fully investigated and understood crystal structures and phase transitions of $M_3H(SO_4)_2$ ($M = NH_4^+$, K^+) compounds, presented a decent challenge, and provided enough motivation for the accomplishment of this dissertation.

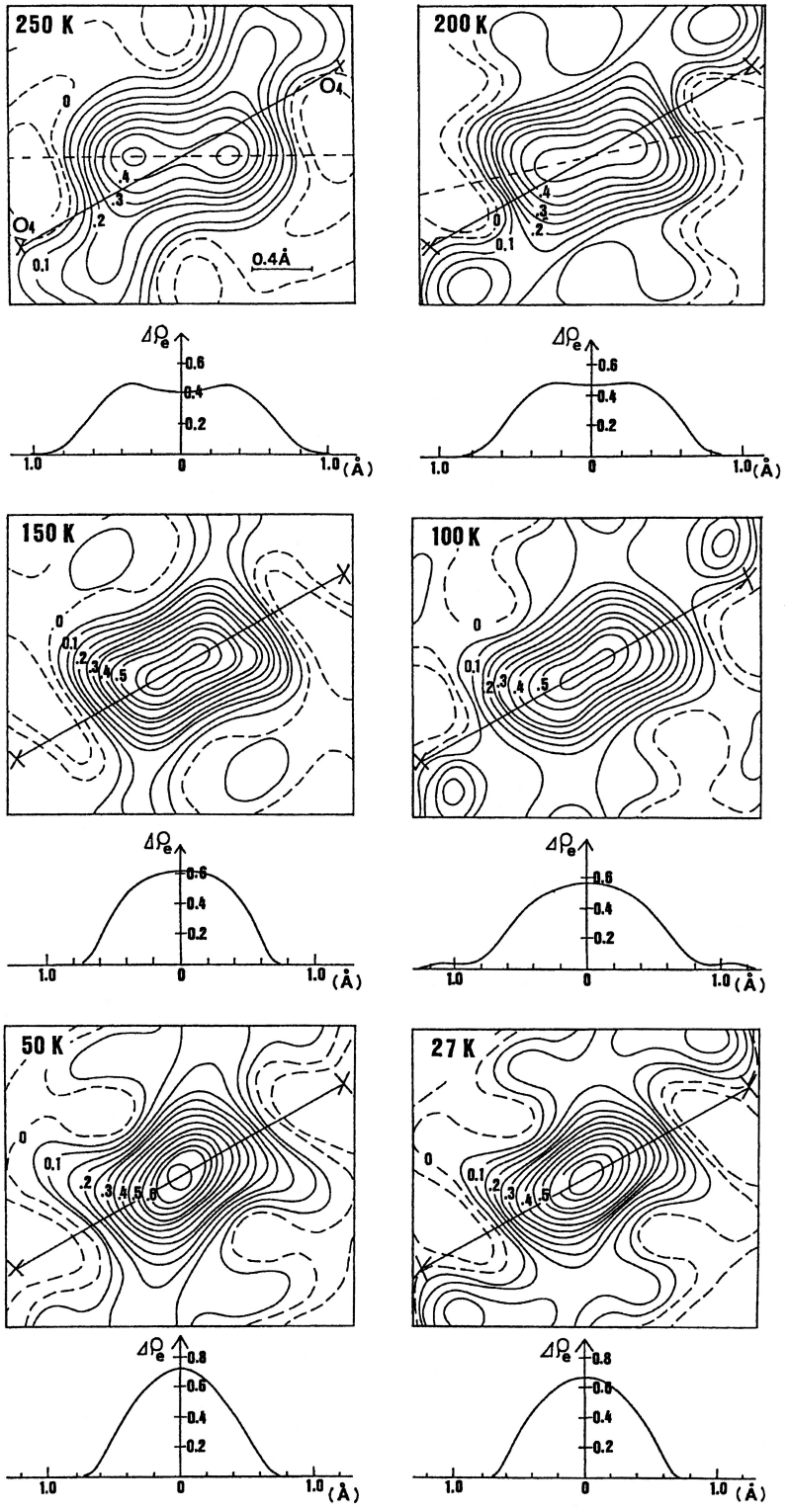

Figure 1.4: Electron density contour map of the H atom in the $(SO_4)H(SO_4)$ dimer in TKHS as a function of temperature [28].

Chapter 2

Sample preparation

2.1 Single crystal growth

Single crystals of TAHS were grown from aqueous solution by the temperature-cooling method. The correct stoichiometric molar ratio between $(NH_4)_2SO_4$ and H_2SO_4 should be 3:1 for the solution. However, it was proven by X-ray powder diffraction, that H_2SO_4 should be slightly in excess to obtain single-phase TAHS-crystals, otherwise needlelike $(NH_4)_2SO_4$ crystals were also formed and detected. With a careful selection of seed crystals showing optical quality, TAHS single crystals up to several cm in size were grown (see Fig. 2.1). The transparent platelet-like crystals show a pseudo-hexagonal habitus.

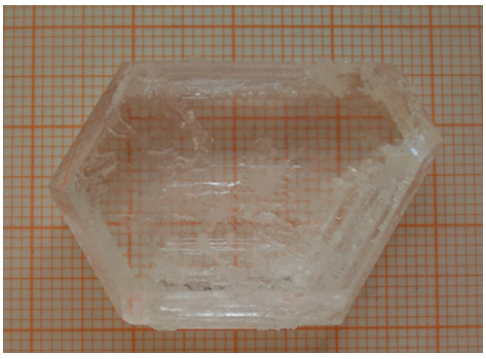

Figure 2.1: Single crystal of TAHS (approx. $30 \times 40 \times 15$ mm^3).

The growth of TKHS single crystals was more complicated than in the case of TAHS. Since the seed crystals of TKHS tend to build multidomains (see Fig. 2.2), both the slow evaporation and temperature-cooling method did not work out to grow monodomain TKHS-crystals of several cm in size. To obtain larger crystals, an extra slow nucleation

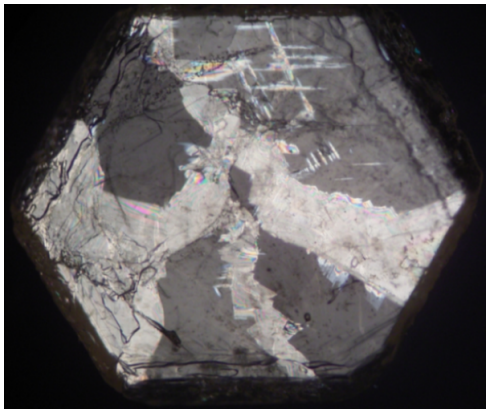

Figure 2.2: A TKHS crystal under the polarizing microscope (approx. $7 \times 6 \times 1$ mm^3).

process of seed crystals was undertaken. The aqueous solution of TKHS with 3 mol K_2SO_4 and 1 mol H_2SO_4 (a little in excess) in an Erlenmeyer flask was almost saturated at room temperature and heated up to $\sim$ 315 K. It was then stored in a closed box with a temperature controller and slowly cooled down to room temperature for several days. Finally, it was taken from the thermal cabinet and left at room temperature for a couple of weeks. Through this slow method, only a few seed crystals began to form at the bottom of the flask and continued growing in larger size. Though they also showed multidomains, a clear monodomain part could be cut out of it.

2.2 Preparation of polycrystalline samples (powders)

A good quality of powder samples is required for more accurate results of X-ray and DSC measurements. Therefore single crystals of TAHS and TKHS were ground in an agate mortar. At first, the preparation of TAHS-polycrystalline samples took place in air, which left rather soft and muddy impression by grinding. During a temperature-dependent X-ray powder measurements with those samples, strange anomalies were observed. When complete powder diffractograms were repeatedly taken at the same temperature, the intensities of some reflections changed irregularly whereas the reflection positions did not move at all [10, 30] (Fig. 2.3). Some of the peaks gained and others lost on their intensities. This observed anomaly, however, disappeared after the samples were heated up to the high-temperature phase and cooled down again and the repeated powder diffractograms showed no intensity variation any more. A hypothesis about this effect was that the crystal is exposed to a certain pressure by grinding and the already embedded solution is pressed out of the crystal. The aqueous solution,

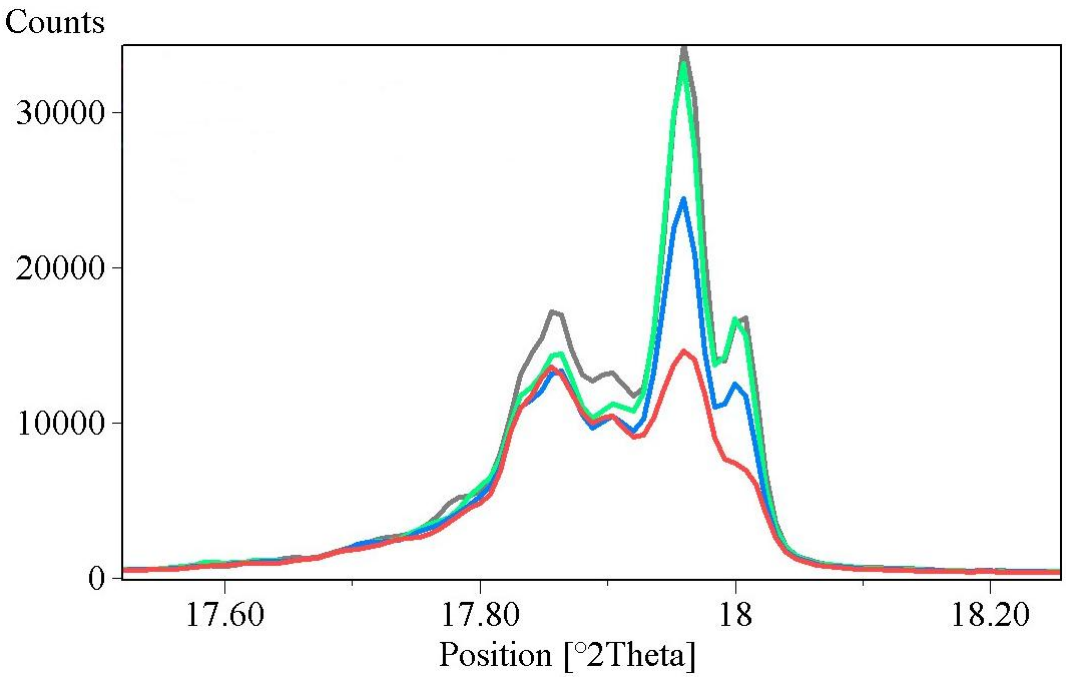

Figure 2.3: A section of repeated X-ray powder diffractograms from the sample prepared in air at 367.5 (1) K.

from which the crystals were grown, contains highly concentrated acid sulphur which is hygroscopic. The volume of the sample surface increases by grinding, and the sample now with hygroscopic solution is very likely to absorb humidity from the air, which left therefore a kind of muddy feeling at the grinding process. Through this humidity a recrystallisation of the polycrystallites occurred on the sample surface, which resulted in intensity changes of the reflections without changing their peak positions. However, when the sample was further heated up, the humidity evaporated from the sample surface and afterwards the diffractograms were absolutely stable. To avoid those effects, the polycrystalline samples were prepared in a glove box which provides a very dried air condition ($\sim 0.4 - 1.2$ % relative humidity). In fact, the humidity display at the glove box slightly increased at the beginning of the grinding process, which is caused due to the evaporation of minor solution in the crystals. Other than this small notice, the grinding of the sample crystals felt dry and sandy in a glove box. The X-ray powder diffractograms with the samples prepared in a glove box were indeed stable throughout the repeated X-ray scans on heating and cooling. The hypothesis described above was supported by TG (Thermogravimetry) measurements (see Fig. 2.4). A loss of weight was evidenced on heating when the sample was prepared in air whereas no changes were observed when the sample was ground and prepared in a glove box from the beginning.

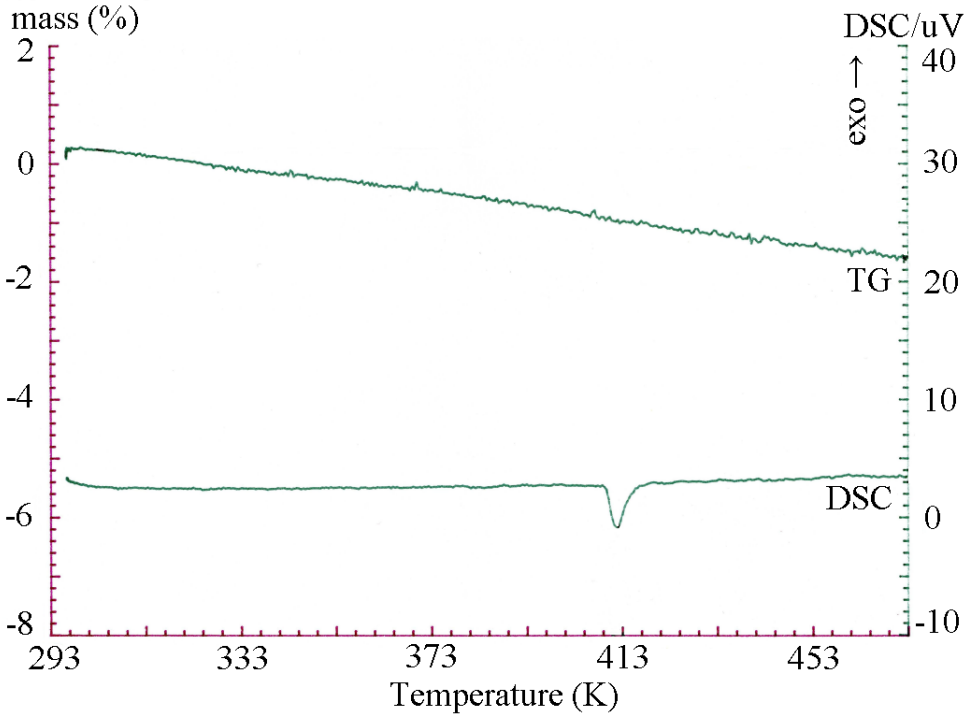

Figure 2.4: A DSC/TG measurement on the powder sample prepared in air shows a continuous loss of mass as the temperature rises.

In addition, fine Si-standard powder was mixed to the sample for X-ray powder diffraction. Using an internal standard is practical for the correction of the zero-point errors which may occur at temperature-dependent measurements. The prepared powders were then directly mounted on a sample holder in the glove box for X-ray powder diffraction. For later use (e.g. for DSC measurements) the powder sample was kept in a small plastic container.

Chapter 3

Experimental

3.1 X-ray single-crystal diffraction

To verify the possible modulation of TAHS reported by X-ray diffraction [8], similar experiments have been carried out with an imaging plate diffractometer STOE-IPDS II and MoKα radiation at various temperatures. A single-crystal of TAHS ($0.3 \times 0.3 \times 0.1$ mm^3) was fixed on top of a glass capillary ($\phi = 0.2$ mm) and placed onto a goniometer head. In the diffractometer the sample is centred in a beam of $\phi = 0.5$ mm (see Fig. 3.1) using a light microscope, so that the sample is completely irradiated by the X-ray beam during the whole measurement.

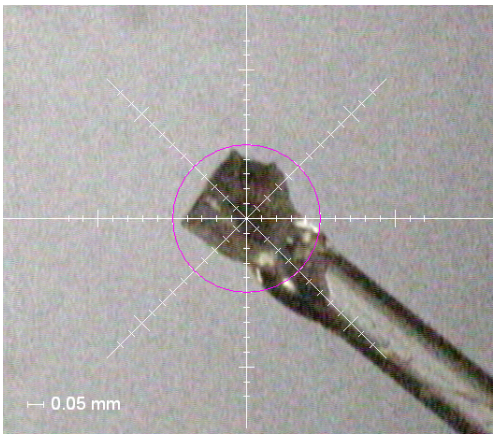

Figure 3.1: A single crystal of TAHS ($0.3 \times 0.3 \times 0.1$ mm^3) centred in a $\phi = 0.5$ mm X-ray beam.

For low-temperature measurements an Oxford Cryosystems 600 LN_2-flow cooler was used, which provides a temperature stability of $\sim \pm 0.2$ K. A low voltage of 30 kV was

chosen to exclude a possible $\lambda/2$-effect (energy of Mo $K\alpha_1$ = 17.480 keV). The data reduction was performed with the program X-Area [31]. From each frame reflections of a certain criterion (e.g. I > 2σ(I)) are selected and with an indexing process, the space group symmetry and lattice parameters are calculated. With this process, an orienting matrix is defined, which describes the relation between the crystallographic axes of the sample in the reciprocal space and the orthogonal axis of the diffractometer (Fig. 3.2). After the determination of the orienting matrix, all *hkl*-reflection intensities are

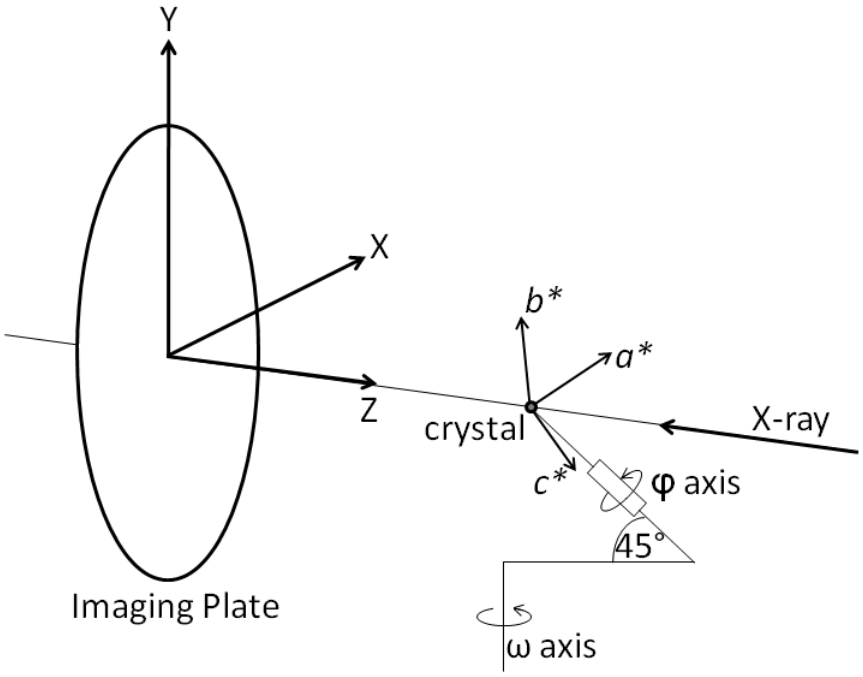

Figure 3.2: Reciprocal lattice vectors of a sample on the goniometer head and the orthogonal coordinate system of the STOE-IPDS II.

integrated and saved in a separate file. Since the X-ray beam experiences attenuation within the crystal, an absorption correction has to be applied to the measured intensities before a crystal structure can be solved and further refined. This absorption process can be expressed in the following equation:

$$I = I_0 \cdot exp(-\mu d)$$

where μ is the linear absorption coefficient and d is the path length of the beam in the sample. Whether an absorption correction is needed or not depends on the size of the linear absorption coefficient and the crystal size. Furthermore the crystal form has to be considered for an absorption correction, since the path length of the beam can vary

with the sample orientation in a case of strongly anisotropic crystal form. The structure refinement was carried out with the SHELXL-97 program [32]. The experimental details are given in Table 3.1.

Table 3.1: Experimental details of X-ray single crystal diffraction.

Diffractometer	STOE IPDS II
Wavelength (Å)	Mo $K\alpha$ = 0.71073
Tube voltage (kV)	30
Tube current (mA)	25
Collimator size (mm)	0.5
Temperature (K)	298, 150, 136, 126
Detector distance (mm)	80.0
Data collection method	ω-scans (0-180°), $\Delta\omega$= 1°, φ=0°, 90°
Exposure time (min)	2.0

3.2 X-ray powder diffraction

X-ray powder diffraction experiments were carried out with the X'pert PRO diffractometer (PANalytical). The $\Theta - \Theta$ geometry of the diffractometer allows the sample to stay flat in the horizontal plane during the data collection. The diffraction data were gathered in Bragg-Brentano geometry with Cu $K\alpha_{1,2}$ radiation. A position-sensitive detector with 128 channels covering approx. 2° registered the diffracted beam. This detector has the advantage that the data can be obtained more precisely and very fast. A specially developed furnace was used for the high-temperature measurements. The sample is directly prepared onto the furnace which consists of a platinum sample holder and a platinum heater underneath (Fig. 3.3). The temperature was measured through a NiCr-Ni thermocouple with an accuracy of ±0.1 K. For the low-temperature measurements (down to $\sim 8.0\,(1)$ K) a CTI-Cryogenics Closed Cycle Refrigerator System with He-gas was used (Fig. 3.4). At each temperature, complete X-ray powder scans ($10° \leq 2\Theta \leq 90°$) were recorded repeatedly for several times for the sake of better statistics and control of stability of the measurements. Moreover, the changes of diffraction patterns could be observed effectively. Following the measurement on heating and cooling enabled a verification of possible hysteresis effects and a reproducibility of the whole process could also be checked. Due to a strong texture effect of the sample powders no Rietveld refinements were possible and only profile matching with the FullProf

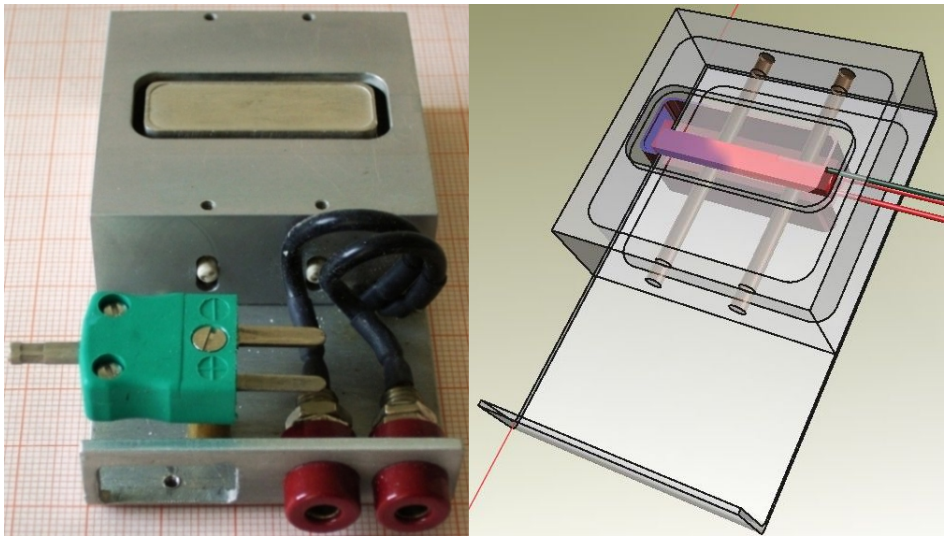

Figure 3.3: A flat sample holder made of platinum, functioning as a furnace at the same time. Illustration received with thanks from Dipl.-Ing. Franz-Dieter Scherberich.

program [33] has been performed. Further experimental parameters are given in Table 3.2.

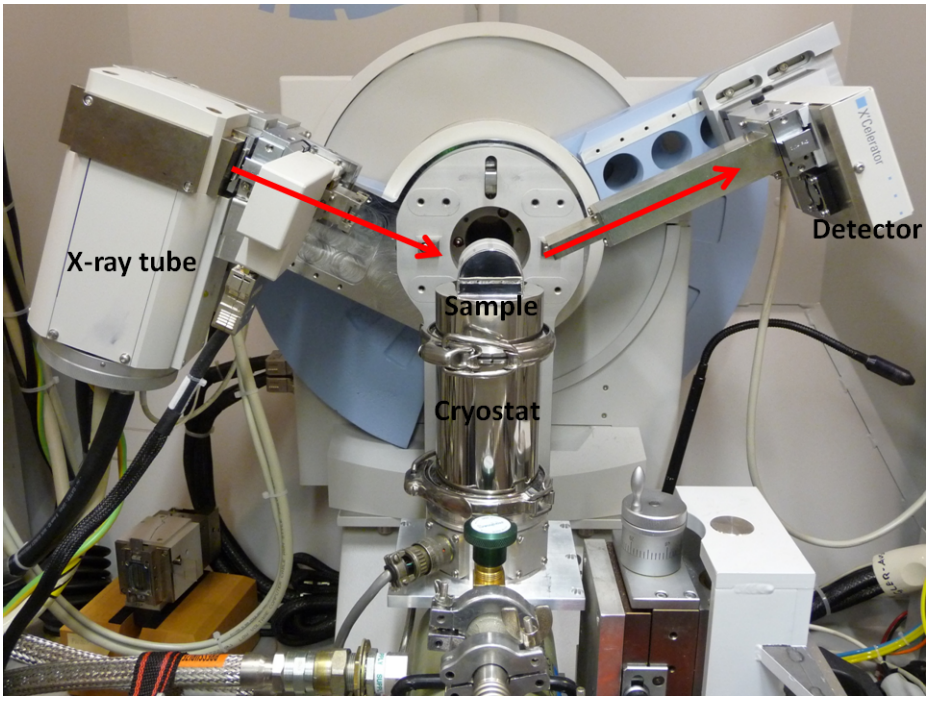

Figure 3.4: X'pert PRO diffractometer for low-temperature measurements.

Table 3.2: Experimental details of X-ray powder diffraction.

	TAHS	TKHS
Diffractometer	X'pert PRO diffractometer (PANalytical)	
Wavelength (Å)	Cu $K\alpha_1$ = 1.540598, Cu $K\alpha_2$ = 1.544426	
Tube voltage (kV)	45	
Tube current (mA)	40	
Temperature range(K)	8 – 427	298 – 479
Data collection method	Bragg-Brentano geometry	
Data scan range (2Θ)	10°-90°	10°-90°, 16°-47°
Step size (2Θ)	0.008°	
Measuring time per step (sec)	50 (128 channels)	

3.3 Neutron single-crystal diffraction

TAHS single crystals of typically $3 \times 3 \times 3$ mm^3 in size were used for the neutron diffraction experiments. A complete dataset of Bragg reflection intensities was collected up to sufficiently high $\sin\Theta/\lambda$ on the four-circle diffractometer HEiDi at the FRM II in Garching at different temperatures. The neutron single-crystal dataset at room temperature was obtained on the four-circle diffractometer SV28 at the DIDO-reactor, FZ in Jülich. For high-temperature measurements, a small cylindrical, thin walled Al-furnace was combined with a goniometer head. The sample was then heated through a NiCr-resistance filament winding around the upper and lower part of the furnace (Fig. 3.5) [34]). This furnace provides a long term temperature stability of ±2 K. Test exper-

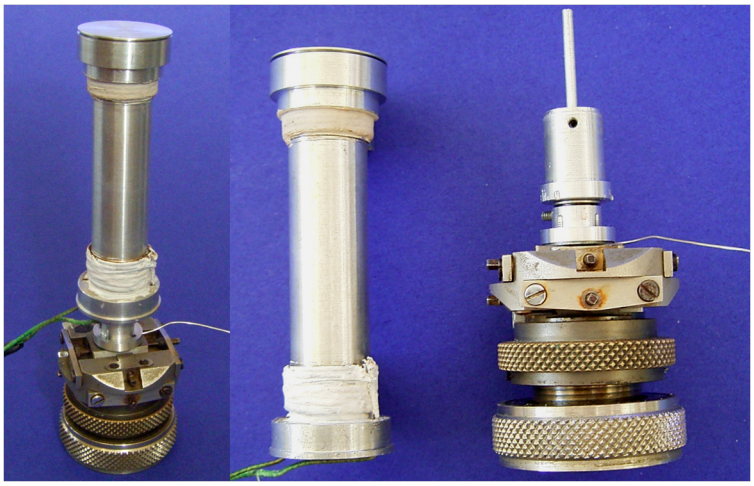

Figure 3.5: An Al-furnace for neutron single-crystal diffraction at high temperatures.

iments have revealed that the large, almost perfect TAHS crystals were damaged or even broken when passing the $C2/c - R\bar{3}m$ phase transition on heating. This strain-induced effect can be avoided by using a crystal with twin domains in the monoclinic TAHS-II phase at room temperature. Slow heating through the phase transition leads to a monodomain single crystal in the TAHS-I phase. For low-temperature measurements a SUMITOMO RDK 101 cryostat (He-gas) was used. As can be seen in Fig. 3.6, the sample was wrapped in an aluminium foil and attached on a sample holder in

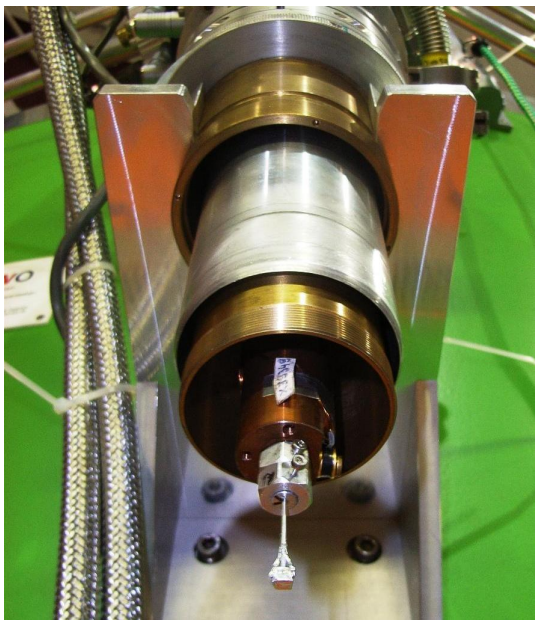

Figure 3.6: TAHS sample in the cryostat at the four-circle diffractometer HEiDi.

the cryostat. The data reduction was performed with the program PRON [35]. No absorption correction was made due to the small linear absorption coefficient ($\mu = 0.017$ mm^{-1} at $\lambda = 0.555$ Å). The structure refinement was performed with the JANA2006 program [36]. The secondary extinction correction was undertaken with JANA2006 relating to the theoretical models and formulas described by P.J. Becker and P. Coppens [37], which also corresponds to the definition by W. H. Zachariasen [38]. No significant intensity decay was found between measurements of standard reflections. The experimental details are given in Table 3.3.

3.4 Differential scanning calorimetry/Thermogravimetry

The DSC/TG measurements were carried out using a Netzsch STA 409 apparatus. The powder sample of $\sim$ 25 mg was prepared in a stenan crucible (chemical composition:

Table 3.3: Experimental details of neutron single-crystal diffraction.

Temperature (K)	413	295	250	150	136
Diffractometer	HEiDi	SV28	HEiDi	HEiDi	HEiDi
Wavelength (Å)	0.555	0.87	0.87	0.87	0.87
$(\sin\Theta/\lambda)_{max}$ ($Å^{-1}$)	0.9	0.7	0.7	0.7	0.7
Absorption coefficient (mm^{-1})	0.017	0.173	0.173	0.173	0.173
Data collection method	ω scan	ω scan	ω scan	ω scan	ω scan
No. of standard reflections	3	2	2	2	2
Time interval of standards (min)	480	600	360	360	240

59 % SiO_2, 35 % Al_2O_3, ≈ 3% TiO_2 and ≈ 1% Fe_2O_3) and a similar amount of Al_2O_3 powder was also prepared as a reference. The heating and cooling rate of 3 K/min was carefully chosen for the experiments to exclude a time-dependent thermal decomposition of the sample. In order to check the reproducibility, repeated measurements were performed under the same experimental conditions. X-ray powder diffraction studies before and after DSC/TG measurements were performed to verify the sample quality during the experiments. For example, new peaks could be found in the case of a thermal decomposition. The temperature range of measurements for TAHS and TKHS was RT – 493.0 (5) K and RT – 548.0 (5) K, respectively.

3.5 Conductivity measurements

For conductivity measurements an impedance spectrometer Solartron 1174 was used in a temperature range from RT – 441 K and with a frequency range of 1 Hz – 500 kHz. Since the anisotropy of the conductivity in TAHS-I was reported [12], TAHS single crystals were cut perpendicular to the monoclinic **a**, **b** and **c** directions with the help of X-ray laue experiments. Silver paste was applied to the sample surface, which served as contact for the electrodes. The TAHS-crystals had a dimension of approx. 3 mm× 3 mm× 0.5 mm (Fig. 3.7).

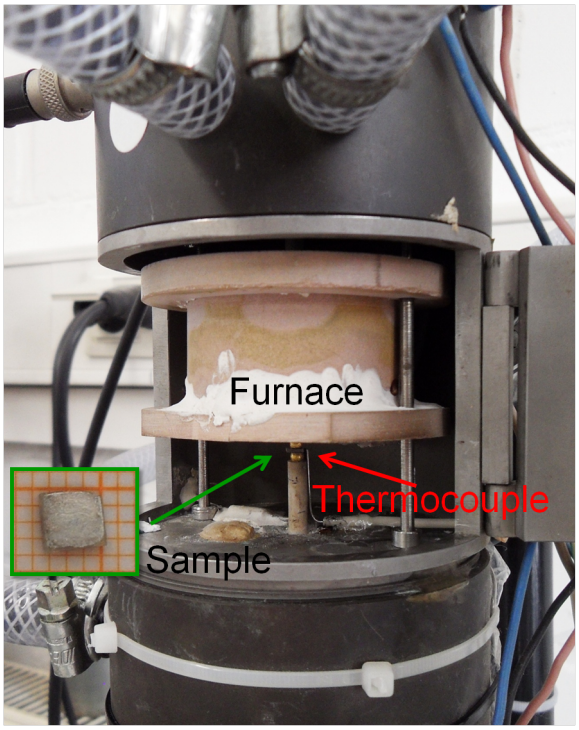

Figure 3.7: Impedance spectrometer Solartron 1174. The furnace is moved upwards to place the sample between two gold electrodes. TAHS sample with silver paste.

Chapter 4

Crystal structure of $(NH_4)_3H(SO_4)_2$

4.1 High-temperature phase I

The high-temperature phase I of TAHS above 413 K crystallizes in the rhombohedral space group $R\bar{3}m$ (No.166 [11]). The lattice parameters in hexagonal setting are $a = 5.907\,(3),\ c = 22.57\,(1)$ Å determined by previous X-ray powder diffraction [30]. These values were used for the refinements of the single crystal neutron diffraction data. The lattice parameters from the single crystal neutron diffraction measurement are $a_n = 5.89\,(4),\ c_n = 22.51\,(7)$ Å. At the beginning of the refinement, the atomic parameters of the high-temperature crystal structure were taken from the literature [9]. Thereby, all atoms except H3 were treated anisotropically. The first result showed well-localized S, N and O atoms with rather small and almost isotropic mean-square displacements whereas all H atoms except H3 showed strongly enlarged anisotropic mean-square displacements. For the next step, the highly disordered crystal structure of TAHS-I was refined and analysed using a split-atom model. In addition, a rigid-body treatment and a spherical shell model was applied, assuming NH_4 groups as freely rotating units.

The splitting of O1 and H1 positions in a SO_4–H–SO_4 hydrogen bond

The striking feature of the high-temperature phase I of TAHS is the disordering of the O1 atom in the SO_4–H–SO_4 hydrogen bond [9]. Instead of lying on a threefold axis, O1 is slightly shifted and located on three symmetrically equivalent positions. This splitting allows shorter O1–O1 bond distances. The H1 atom in the SO_4–H–SO_4 hydrogen bonds is also disordered with only one-third of the site occupancy factor on a $9e$ Wyckoff position. However, no displacement from the ideal position could be observed in the

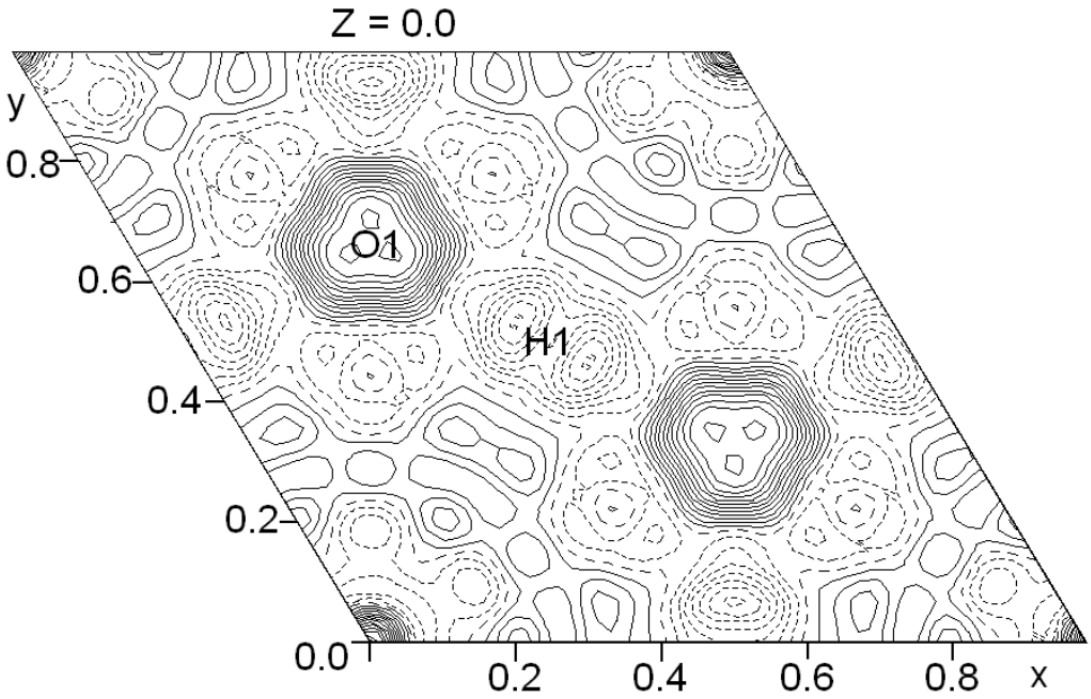

Figure 4.1: Difference Fourier map around the O1 and H1 atoms. There is a clear indication of disorder, with three split positions for O1 and at least two split positions for H1. Positive contours (solid line) and negative contours (dotted line) are drawn at a step of 0.2 fm·Å^{-3}. The negative H density is due to the negative scattering length of the proton.

X-ray diffraction studies [9]. With single-crystal neutron diffraction, the splitting of both, O1 and H1 atoms, could be detected. As shown in Fig. 4.1, a difference Fourier map suggests a splitting for the positions of the O1 and H1 atoms of the SO_4–H–SO_4 hydrogen bond. Therefore, the H1 atoms were refined using a split-atom model with an isotropic mean-square displacement parameter, which is compatible with the previous results from neutron single-crystal diffraction at room temperature. This split-atom model moves the H1-atom position from the 9*e*-Wyckoff to a 18*h*-Wyckoff position. Thereby, its site occupancy factor reduces from 1/3 to 1/6. Fig. 4.2 shows the O1–H1–O1 hydrogen bond network in the (001) plane.

$N1H_4$ group in TAHS-I

The $N1H_4$ groups lie at the centre of the six-membered ring of the SO_4–H–SO_4 hydrogen bond network. According to the high site symmetry $\bar{3}m$ of the N1 atom (0,0,0; 3*a*-Wyckoff position) of the $N1H_4$ group, an ordered NH_4 tetrahedron description is not

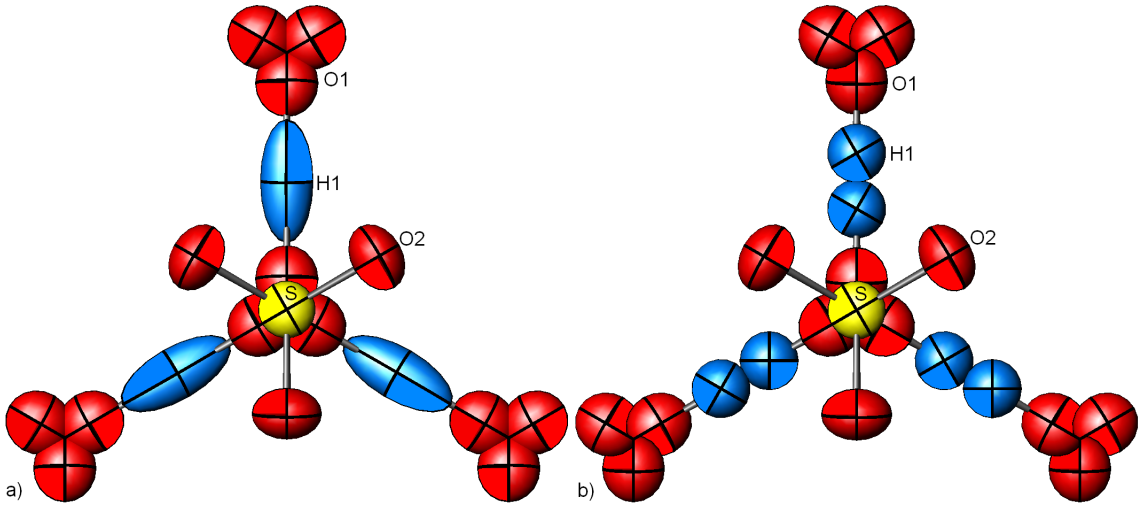

Figure 4.2: O1–H1–O1 hydrogen bond network in the (001) plane (view along [001]). a) H1 atom on a 9*e*-Wyckoff position with enlarged anisotropic mean-square displacements; b) split-atom model. Displacement ellipsoids are drawn at the 50 % probability level.

simple. Three different models have been chosen, keeping a reasonable tetrahedral geometry as well as acceptable N–H bond lengths.

i) Split-atom model: Around the well localized N1 atom, definite proton positions were searched from a difference Fourier map. With two symmetrically independent proton sites a total number of 12 split-atom positions were used in the refinement (Fig. 4.3). With this model, six different orientations for the $N1H_4$ tetrahedron exist. Three H2 atoms either on upper or lower part form the basis of a tetrahedron and each set can choose one out of three different H3 atoms on the opposite part as the top. Hence, each H3 atom defines one out of six possible $N1H_4$ orientations, whereas each smeared out H2 atom belongs to three different orientations having three varied z-parameters. As a result, the H2 atoms were refined anisotropically. The $N1H_4$ group forms N–H$\cdots$O hydrogen bonds with adjacent SO_4 tetrahedra (Fig. 4.4).

ii) Isotropic model: Since the N–H bond lengths are significantly different with two symmetrically independent H atoms in a split-atom model, a more isotropic model for the $N1H_4$ group was tested. Instead of two different H atoms, only one H2 atom on a general position was defined. Through the high site symmetry of $\bar{3}m$, 12 H2-atom positions are generated around the N1 atom with a site occupancy factor of $1/3$. The refinement of this model, however, brought two nearest neighbour atom positions too close to each other, such that their anisotropically refined mean-square displacements overlapped (see Fig. 4.5a). Therefore, the middle position of these two atom sites was

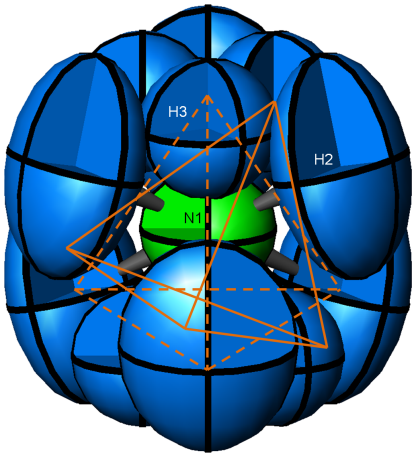

Figure 4.3: $N1H_4$ group described with the split-atom model using 12 H atoms. Dashed lines indicate the NH_4 tetrahedron orientation for a conventional model. One of six possible tilted NH_4 tetrahedra is marked with solid lines. Displacement ellipsoids are drawn at the 50 % probability level.

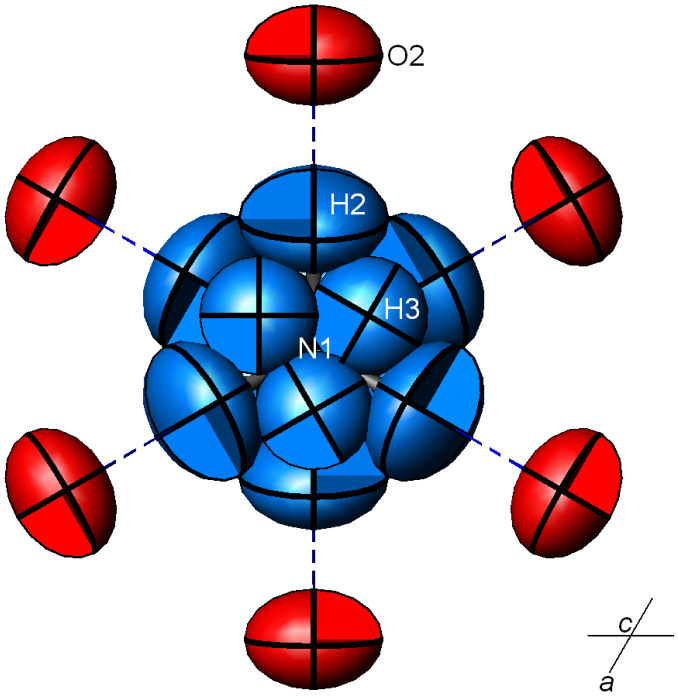

Figure 4.4: A $N1H_4$ tetrahedron (split-atom model) with nearest oxygen (view along [001]). Three O-neighbours are on the upper and the others are on the lower part of the $N1H_4$ tetrahedron. Displacement ellipsoids are drawn at the 50 % probability level.

defined and only six H2 atoms were used for the refinement (Fig. 4.5b). This model yields an equal N–H bond length of 0.95 (1) Å and a homogeneous O···H distance of 2.04 (1) Å in the N–H···O hydrogen bonds. The problem of this isotropic model is

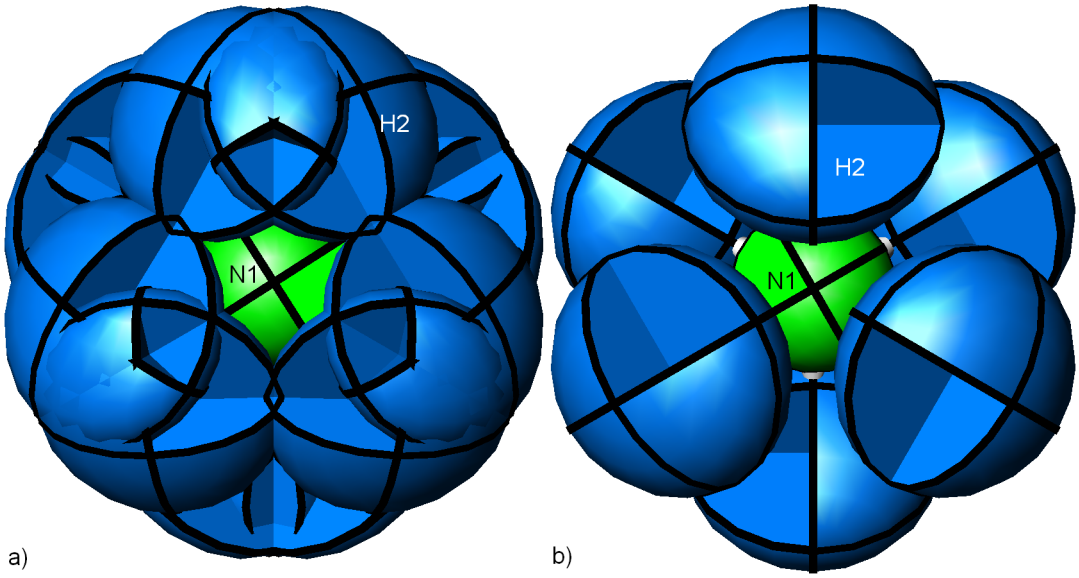

Figure 4.5: A $N1H_4$ tetrahedron with an isotropic model refinement. a) H2 atom on a general position. b) H2 atom on a special position ($x, \bar{x}, z$; 18h-Wyckoff position). Displacement ellipsoids are drawn at the 50 % probability level.

that no adequate NH_4 tetrahedral geometry can be built with six equally distributed H atoms around N1. The only relevant statement may be that there exist six equivalent H2-atom positions around N1, that are only partly occupied (site occupancy factor of $^2/_3$). This model assumes the $N1H_4$ group as a freely rotating unit.

iii) Spherical shell model: Under the assumption of the $N1H_4$ group as a freely rotating unit, a continuous proton density on a spherical shell around the N1 position was refined using the FullProf program [33]. This model yields a N–H bond length of 1.08(4) Å. For a better verification and comparison of this last model, the split-atom model was refined using the same FullProf program. In Fig. 4.6 the results of both refinement models are shown. The final weighted R factor of the split-atom model was 0.0764 with 48 parameters, whereas the spherical shell model yields the final weighted R factor of 0.127 with 41 parameters.

$N2H_4$ group in TAHS-I

Due to the strongly enlarged anisotropic displacement parameters, a split-atom model was applied for the $N2H_4$ group. As in the case of the $N1H_4$ group, six different

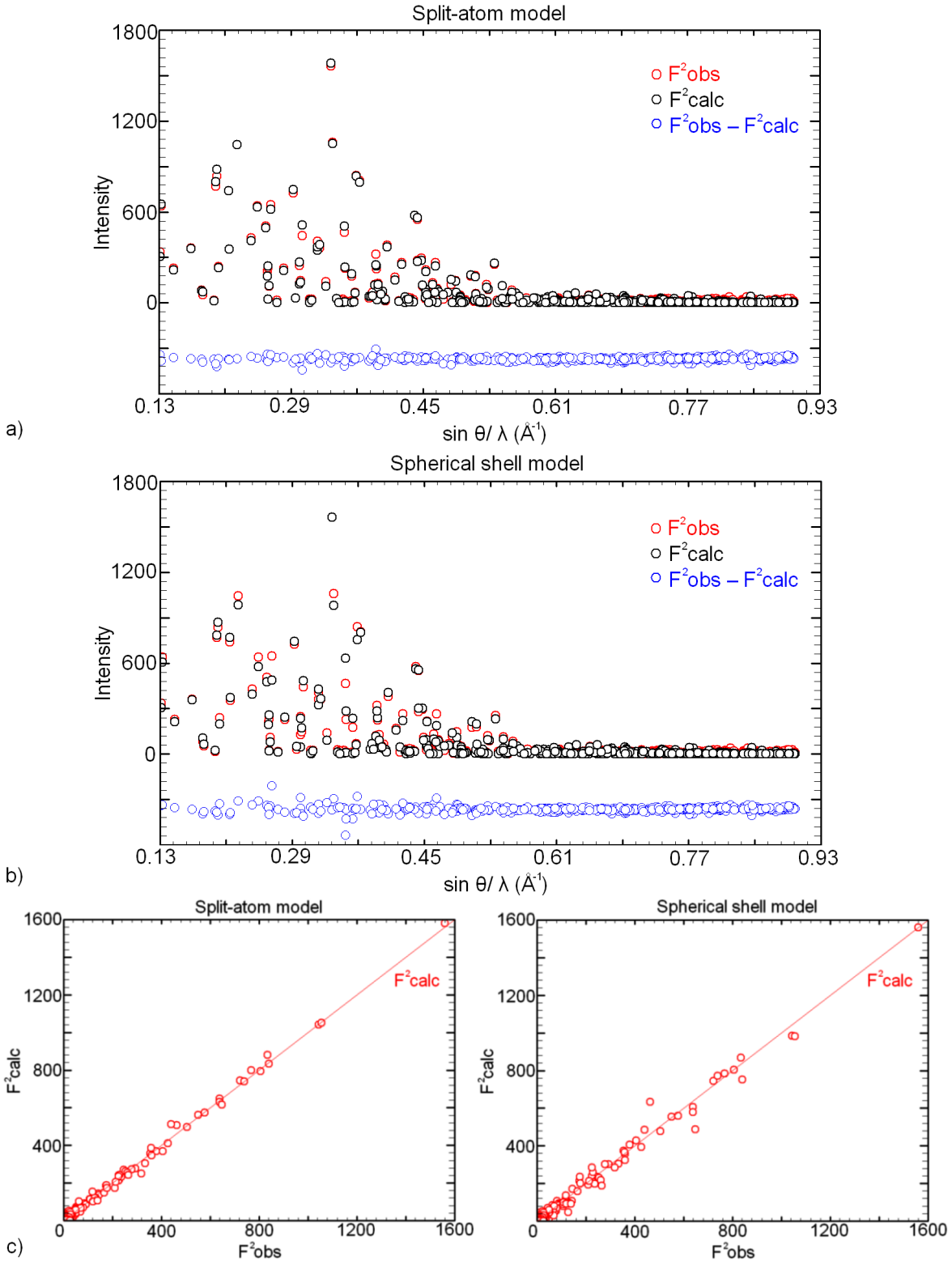

Figure 4.6: a) Intensity plot of split-atom model as a function of sinΘ/λ. b) Intensity plot of spherical shell model as a function of sinΘ/λ. c) F^2_{calc}= F^2_{obs} plot of split-atom and spherical shell model.

orientations of $N2H_4$ are possible. For that reason, each H4 atom belongs to two and each H5 to three specific $N2H_4$ orientations. Each $N2H_4$ tetrahedron orientation is tilted compared to the conventional model and, hence, anisotropic mean-square displacement parameters were chosen for the H atoms (Fig. 4.7). The splitting of H4 and H5

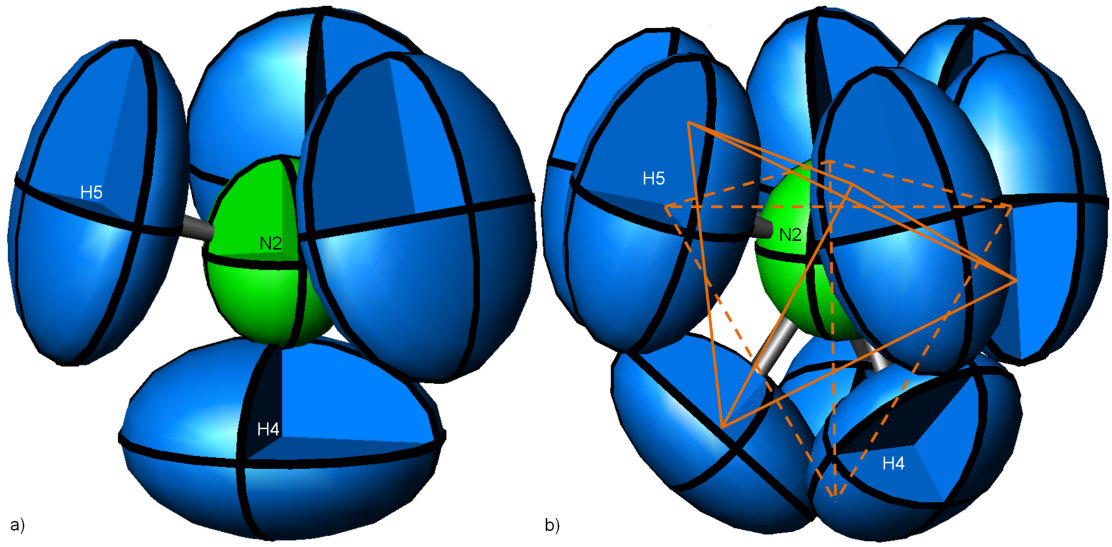

Figure 4.7: $N2H_4$ tetrahedron with a) conventional model b) split-atom model. The tetrahedron drawn by solid lines shows one of six possible orientations whereas the dashed tetrahedron results from the conventional model. Displacement ellipsoids are drawn at the 50 % probability level.

corresponds very well to its environment, because, instead of building, for example, bifurcated N–H···O hydrogen bonds, each split H atom forms only one specific hydrogen bond with adjacent SO_4 groups (Fig. 4.8). For the H4 atom, there exist altogether three nearest O neighbours in the same distance. On splitting, each H4 atom forms a single hydrogen bond with an adjacent O2. The N–H bond lengths and the distance of N–H···O hydrogen bonds are given in Table 4.1.

Table 4.1: N–H···O hydrogen bond distances (Å) and angles (°) (split-atom model).

N–H···O	N–H	H···O	N–O	angle
N1–H2···O2	1.03 (1)	2.00 (2)	2.963 (3)	154 (1)
N2–H4···O2	1.02 (1)	2.09 (1)	3.093 (5)	168 (1)
N2–H5···O2	0.98 (1)	2.12 (1)	3.092 (3)	173.7 (6)

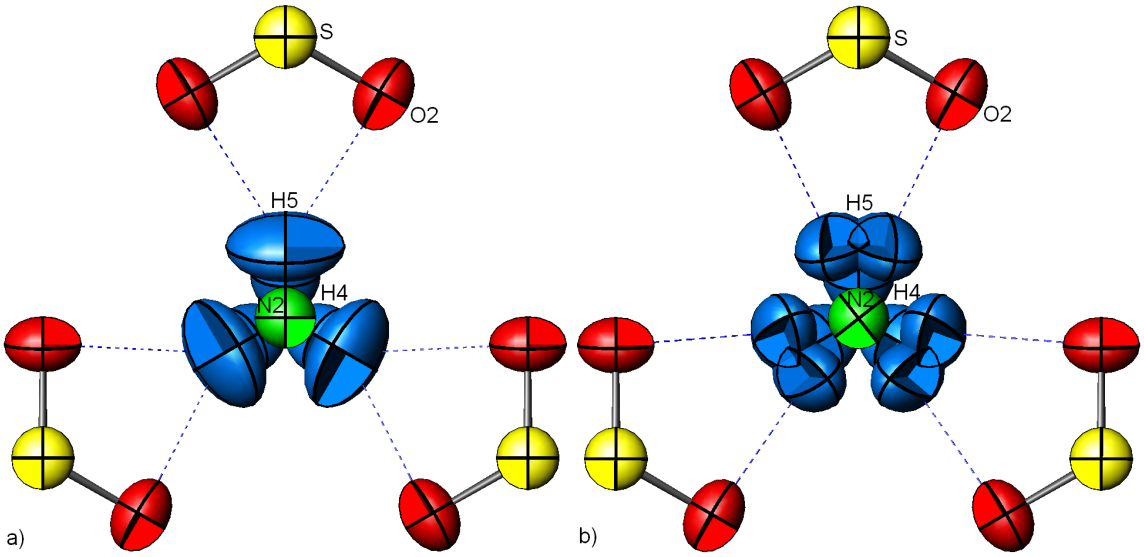

Figure 4.8: A $N2H_4$ tetrahedron with adjacent SO_4 groups (view along [001]). a) Bifurcated hydrogen bonds in the conventional model. b) Single hydrogen bonds with the split-atom model. The N2–H4···O2 hydrogen bonds are not illustrated here. Displacement ellipsoids are drawn at the 50 % probability level.

Unit cell of TAHS-I (relation between different moieties)

The rhombohedral structure with the space group $R\bar{3}m$ consists of SO_4 tetrahedra linked to each other via H1 atoms, in which each SO_4 tetrahedron points with its O1 atom alternately up and down with respect to the **c**-axis. These O1–H1–O1 hydrogen bonds build a two-dimensional pseudo-hexagonal network in the (001) plane. The O1 atom is disordered and occupies a 18*h*-Wyckoff position, with a site occupancy factor of 1/3. The H1 atom was refined using a split-atom model. As a result, the proton position moved to the 18*h*-Wyckoff position with a site occupancy factor of 1/6. The $N1H_4$ groups lie at the centre of a six-membered ring of the O1–H1–O1 hydrogen bond network (see Fig. 4.9). The nuclear density map around the $N1H_4$ indicates possible proton diffusion between $N1H_4$ and the O1–H1–O1 hydrogen bonds in the (001) plane. The atomic distance from H1 to the other nearest H1 of the neighbouring O–H–O hydrogen bond is 2.27 (2) Å, whereas the distance between H1 and H2 ($N1H_4$) is 2.26 (1) Å. This supports the idea of NH_4 group involvement in proton conduction as proposed by Merinov *et al.* [15] and Fechtelkord *et al.* [14]. The $N2H_4$ groups are building double layers with alternating hydrogen configurations. They are separated by SO_4–H–SO_4 sandwich structures perpendicular to **c** (see Fig. 4.10). The $N1H_4$ and $N2H_4$ tetrahedra are linked via N–H···O hydrogen bonds to the same O2 atoms. Adjacent $N2H_4$

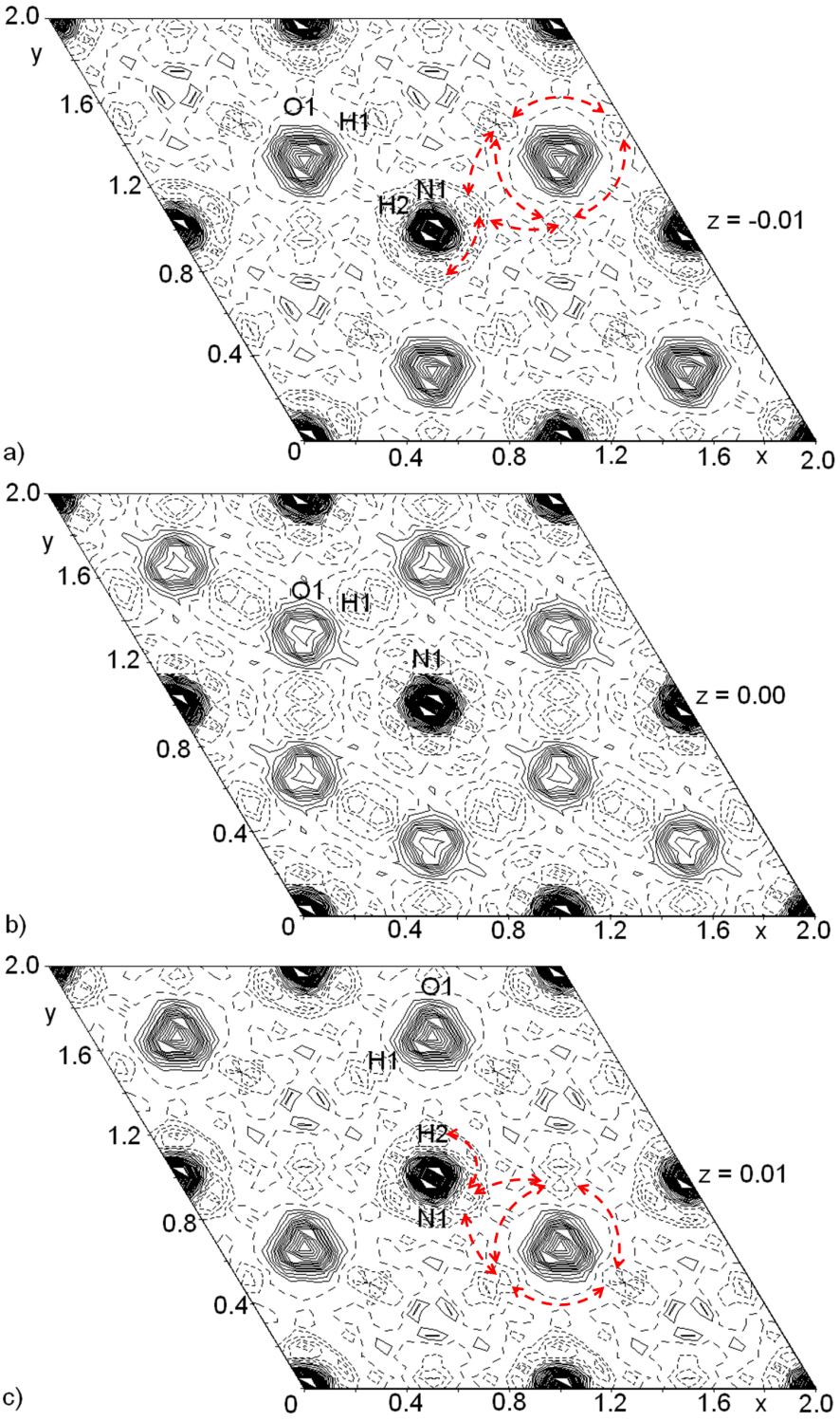

Figure 4.9: Nuclear density map F_{obs} of hydrogen bonds in the (001) plane with different z-parameters. Possible proton diffusion pathways are marked with dashed arrows. Positive (solid line) and negative (dotted line) contours are drawn in steps of 0.5 fm·Å^{-3}.

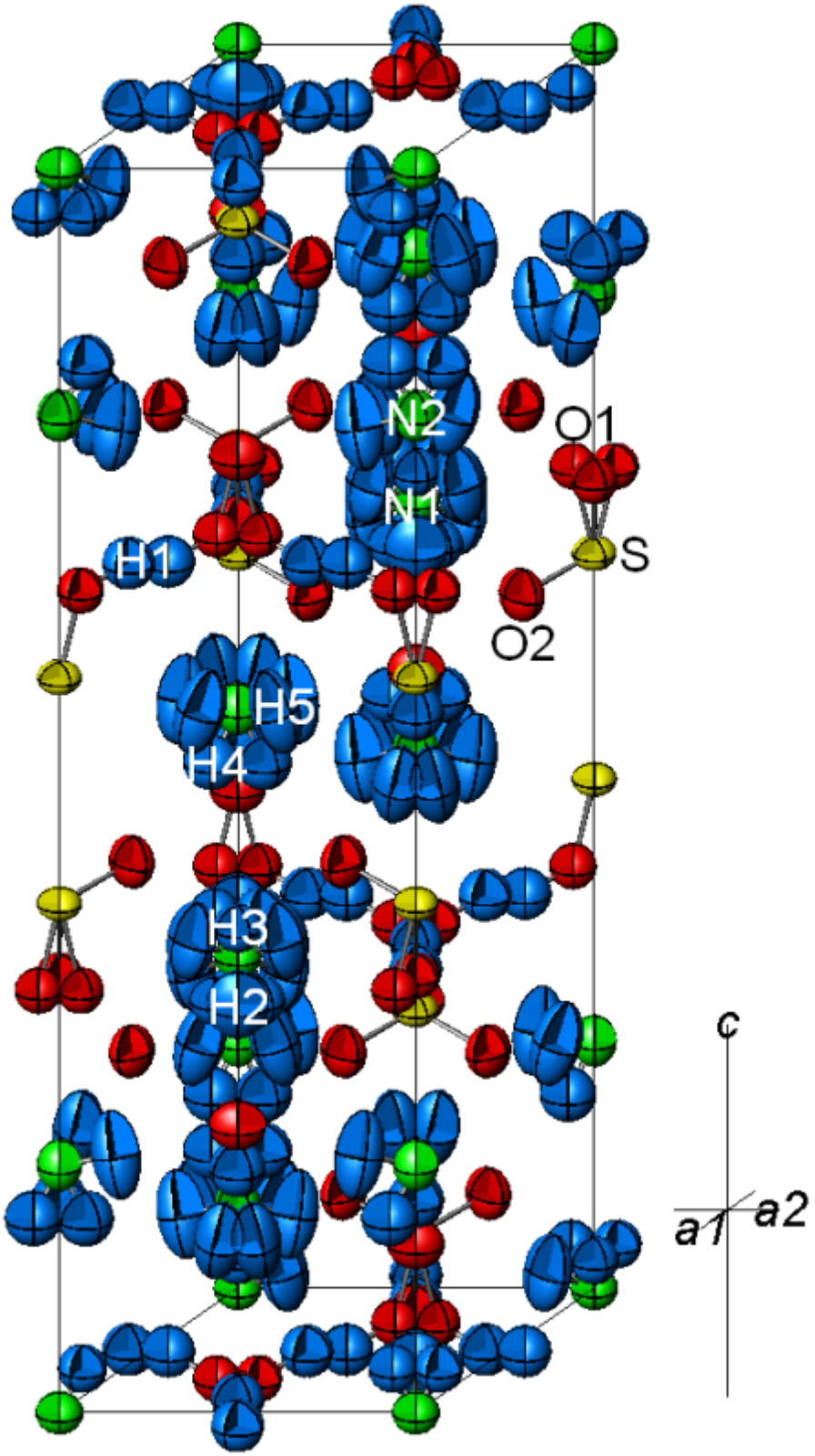

Figure 4.10: The rhombohedral unit cell of TAHS-I in hexagonal setting (space group $R\bar{3}m$). Displacement ellipsoids are drawn at the 50 % probability level.

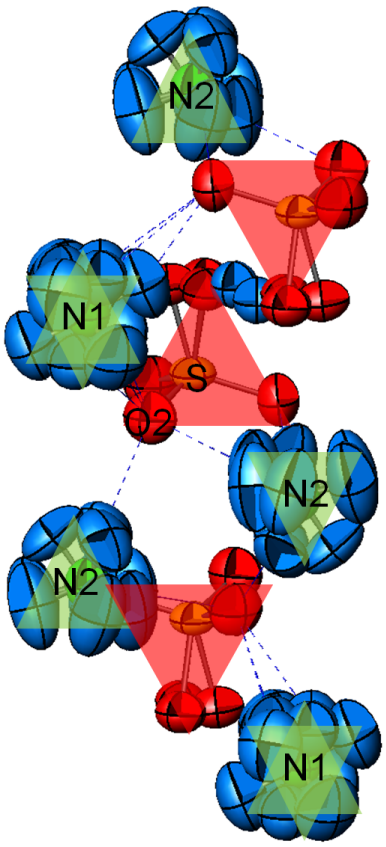

Figure 4.11: N–H···O hydrogen bonds linking different NH_4 groups along the c direction. Displacement ellipsoids are drawn at the 50 % probability level.

tetrahedra are also interlinked to each other in the same way by N–H···O hydrogen bonds sharing the same O2 atoms (Fig. 4.11). The refinement details of model i) and ii) are presented in Table 4.2 and the results are presented in Table 4.3 – 4.4.

Rigid-body analysis of the NH_4 groups

According to the strongly enlarged ADPs around the well defined N atoms, a rigid-body analysis was performed in order to describe the translational and librational motion behaviour of the NH_4 groups. Since the rigid-body analysis needs anisotropic mean-square displacement parameters for every involved H atoms, the isotropic model was chosen. The N1 and N2 atoms were defined for each group as molecule-fixed origins. The specific high site symmetries of N1 ($\bar{3}m$) and N2 ($3m$) reduced the number of **T** (translational tensor), **L** (librational tensor) and **S** (correlation tensor of translation and libration) parameters to 4 and 5 out of 21 general parameters [39]. The crystal structure of TAHS-I is then refined with each NH_4 group as a rigid-body and **T**, **L** and **S** parameters are

Table 4.2: Crystal data and refinement details of TAHS-I with neutron single-crystal diffraction.

Refinement model	i (split-atom)	ii (isotropic)
Chemical formula	$HO_8S_2{\cdot}3H_4N$	
M_r	247.25	
Crystal system	Trigonal	
Space group	$R\bar{3}m$	
Temperature (K)	413 (2) K	
a, c (Å)	5.907 (3), 22.57 (1)	
V (Å^3)	682.0 (6)	
Z	3	
D_x (Mg m^{-3})	1.825	
Data collection		
No. of measured, independent and observed $[I > 3\sigma(I)]$ reflections	1164, 452, 133	
R_{int}	0.065	
$\Theta_{max}(^\circ)$	29.92	
Refinement		
$R[F^2 > 3\sigma(F^2)]$	0.0531	0.0539
$wR(F^2)$	0.1046	0.1064
S	1.44	1.46
Extinction method	B-C type I Lorentzian isotropic [37]	
Extinction coefficient	1400 (300)	1200 (300)
No. of reflections	452	452
No. of parameters	47	44
$\Delta\rho_{max}, \Delta\rho_{min}$ (fm·Å^{-3})	4.64, -2.72	4.56, -2.19

given as further refinable parameters instead of ADPs for the NH_4 groups. The final weighted R factor of the rigid-body refinement yields 0.1347 with 28 refinement parameters. The **T** and **L** tensors are converted to the crystallographic coordinate system after the refinement and listed in Table 4.5. The translational behaviour of the $N1H_4$ group is more pronounced in **a**/**b** directions than in **c**, which can be explained from its location at the centre of the six-memebered ring of O–H–O hydrogen bonds and also,

Table 4.3: Refinement results of TAHS-I from i) split-atom model. The U-values are given in Å^2.

Atom	x	y	z	Occ.	$U_{11}/Uiso$	U_{22}	U_{33}	U_{12}	U_{13}	U_{23}
S	0	0	0.4090 (3)	1	0.061 (3)	0.061 (3)	0.034 (4)	0.030 (1)	0	0
N1	0	0	0	1	0.064 (3)	0.064 (3)	0.058 (4)	0.032 (1)	0	0
N2	0	0	0.1995 (2)	1	0.062 (1)	0.062 (1)	0.082 (2)	0.0307 (6)	0	0
O1	0.0382 (8)	-0.0382 (8)	0.3430 (2)	1/3	0.083 (5)	0.083 (5)	0.053 (3)	0.031 (4)	0 (n.s.)*	0 (n.s.)
O2	0.1355 (2)	-0.1355 (2)	0.5708 (1)	1	0.085 (2)	0.085 (2)	0.084 (2)	0.059 (2)	-0.0018 (7)	0.0018 (7)
H1	0.461 (2)	-0.461 (2)	-0.002 (1)	1/6	0.062 (5)					
H2	-0.087 (1)	0.087 (1)	-0.0227 (8)	1/2	0.119 (8)	0.119 (8)	0.15 (1)	0.082 (8)	-0.014 (5)	0.014 (5)
H3	0.043 (3)	-0.043 (3)	-0.030 (2)	1/3	0.08 (1)					
H4	0.054 (2)	-0.054 (2)	0.1617 (6)	1/3	0.104 (9)	0.104 (9)	0.091 (9)	0.048 (8)	0.023 (5)	-0.023 (5)
H5	0.140 (2)	-0.034 (2)	0.2114 (5)	1/2	0.081 (7)	0.088 (7)	0.215 (9)	0.043 (6)	0 (n.s.)	0.032 (4)

* non-significant values of the refinement parameters are set to zero and fixed.

The bond distances (Å) and angles (°) of TAHS-I from i) split-atom model.

Bond distances				Bond angles			
S–O1	1.540 (8)	N1–H2	1.03 (1)	O1–S–O2	123.0 (4)	H4–N2–H5	128.6 (8)
S–O2	1.460 (3)	N1–H3	0.81 (4)	O1–S–O2’	100.5 (3)	H4–N2–H5’	109.0 (8)
O1–H1	0.96 (2)	N2–H4	1.02 (1)	O2–S–O2’	110.7 (3)	H4–N2–H5”	74.9 (9)
H1–H1	0.79 (2)	N2–H5	0.98 (1)	H3–N1–H2	87 (2)	H5–N2–H5’	112.8 (9)
O1–O1	2.663 (9)			H3–N1–H2’	131 (1)		
				H2–N1–H2’	97.2 (9)		

Table 4.4: Refinement results of TAHS-I from ii) isotropic model. The U-values are given in Å^2.

Atom	x	y	z	Occ.	$U_{11}/Uiso$	U_{22}	U_{33}	U_{12}	U_{13}	U_{23}
S	0	0	0.4089 (3)	1	0.062 (3)	0.062 (3)	0.033 (3)	0.031 (1)	0	0
N1	0	0	0	1	0.066 (2)	0.066 (2)	0.055 (3)	0.033 (1)	0	0
N2	0	0	0.1995 (2)	1	0.062 (1)	0.062 (1)	0.081 (2)	0.0307 (6)	0	0
O1	0.0379 (9)	-0.0379 (9)	0.3429 (2)	1/3	0.083 (5)	0.083 (5)	0.053 (3)	0.031 (4)	0 (n.s.)	0 (n.s.)
O2	0.1353 (2)	-0.1353 (2)	0.5708 (1)	1	0.085 (2)	0.085 (2)	0.084 (2)	0.059 (2)	-0.0015 (7)	0.0015 (7)
H1	0.460 (2)	-0.460 (2)	-0.002 (1)	1/6	0.059 (5)					
H2	-0.075 (1)	0.075 (1)	-0.0247 (4)	2/3	0.152 (7)	0.152 (7)	0.128 (8)	0.086 (7)	-0.020 (3)	0.020 (3)
H4	0.054 (2)	-0.054 (2)	0.1617 (6)	1/3	0.099 (9)	0.099 (9)	0.095 (9)	0.042 (7)	0.025 (5)	-0.025 (5)
H5	0.140 (2)	-0.034 (2)	0.2115 (5)	1/2	0.078 (7)	0.090 (7)	0.217 (9)	0.043 (7)	0 (n.s.)	0.031 (4)

The bond distances (Å) and angles (°) of TAHS-I from ii) isotropic model.

Bond distances				Bond angles			
S–O1	1.539 (8)	N1–H2	0.949 (8)	O1–S–O2	122.9 (4)	H4–N2–H5	129.0 (8)
S–O2	1.459 (3)	N2–H4	1.02 (1)	O1–S–O2’	100.6 (3)	H4–N2–H5’	109.2 (8)
O1–H1	0.95 (2)	N2–H5	0.98 (1)	O2–S–O2’	110.6 (3)	H4–N2–H5”	74.8 (9)
H1–H1	0.83 (2)			H2–N1–H2	89.0 (6)	H5–N2–H5’	112.6 (9)
O1–O1	2.670 (9)			H2–N1–H2’	91.0 (6)		

Table 4.5: **T** (Å^2) and **L** (deg^2) tensors of the NH_4 groups of TAHS-I.

	$N1H_4$ group	$N2H_4$ group
T11	0.069 (1)	0.063 (1)
T22	0.069 (1)	0.063 (1)
T33	0.056 (1)	0.081 (1)
L11	370 (20)	390 (20)
L22	370 (20)	390 (20)
L33	370 (40)	100 (20)

through the proton exchange in the (001) plane between H1 and H2 (further discussed in chapter 6). On the other hand, the $N2H_4$ group has a larger **T** parameter along **c** than parallel to **a** and **b**. This behaviour may result from different orientations of this group, in which the z-parameter of the group can vary for each selected orientation. The libration motion of the $N1H_4$ group at the centre of a pseudo-hexagonal SO_4–H–SO_4 hydrogen bond network is isotropic with equal **L** values for the three crystallographic axes, while the $N2H_4$ group shows much stronger librational motion around the **a**/**b** directions than around **c**. An additional result of the rigid-body refinement for the NH_4 groups is the similar libration amplitude for $N1H_4$ and $N2H_4$ groups around the **a**/**b** directions. This similarity of both NH_4 groups corresponds to the observation from ^{15}N MAS NMR spectroscopy by Fechtelkord *et al.* [40]. They found only one nitrogen signal in TAHS-I indicating that the two N sites experience the same time-averaged chemical environment in the high-temperature phase of TAHS.

4.2 Room-temperature phase II

The crystal structure of TAHS-II has been described in a previous diploma thesis using neutron single-crystal diffraction [10]. Therefore, only a brief summary of the previous results, together with further new studies will be presented in this dissertation. The room-temperature phase II of TAHS is monoclinic, $C2/c$ with lattice parameters $a = 15.431\,(8)$ Å, $b = 5.861\,(3)$ Å, $c = 10.169\,(5)$ Å and $\beta = 101.83\,(5)^\circ$ [30]. There has been a certain ambiguity about the 'correct' space group symmetry of TAHS-II. An observation of a few reflections that violated the reflection condition for a centrosymmetric space group, was reported earlier using single-crystal neutron diffraction [41]. Hence, the corresponding neutron diffraction studies have been performed to clarify the correct reflection conditions. Since neutron diffraction studies need bigger crystals (up

to several mm), a so-called Renniger-effect can appear additionally to the extinction effect. Such reflections observed through the Renninger-effect may result in wrong interpretation of the possible space group symmetry. However, a Ψ-scan perpendicular to the concerned lattice planes reveals whether the reflection is due to single or double diffraction. Using single-crystal neutron diffraction on a TAHS sample ($6 \times 7 \times 8$ mm^3), no violation of the centrosymmetric space group could be found and therefore the existence of an inversion centre in the middle of the $(SO_4)H(SO_4)$ dimer was confirmed [10]. The crystal structure of TAHS-II is characterized by an isolated $(SO_4)H(SO_4)$ dimer and two symmetrically independent NH_4 groups. The H atom site in the middle of the $(SO_4)H(SO_4)$ dimer is located on an inversion centre. By refining this H atom anisotropically, its displacement ellipsoid was strongly elongated towards the symmetric O–H–O bonding. Hence a split-atom model was chosen to describe the hydrogen distribution within the dimer. The two symmetrically independent NH_4 groups consist of rather well localized N atoms with its small and almost isotropic displacement ellipsoids and disordered H atoms with strongly enlarged mean-square displacement parameters. The unit cell of TAHS-II is depicted in Fig. 4.12 and the refinement details and results are listed in Table 4.6 and 4.7.

Disorder of NH_4 groups

The NH_4 groups are surrounded by SO_4 groups and form N–H$\cdots$O hydrogen bonds. Most of the N–H$\cdots$O hydrogen bonds are bifurcated, such that there are two adjacent O atoms with nearly equal distances from the H-atom position. As a result, the H atoms of NH_4 groups show peculiarly enlarged anisotropic ellipsoids. Around the N1 atom which is situated on a special position (twofold axis), there are two symmetrically independent H atoms (H2 and H3), each on a general position. While the H2 atom has only one adjacent O atom (O3) for a N–H$\cdots$O hydrogen bond, the H3 atom has two neighbouring O atoms (O2 and O4). The mean-square displacements of the H3 atoms in the $N1H_4$ group remain more or less unchanged with decreasing temperature. To investigate the disorder character of the $N1H_4$ group with decreasing temperature, an alternative refinement model was also tried, parallel to the model already described above with both, anisotropic H2 and H3 atoms. In this model, the H3-atom position with strongly elongated mean-square displacement parameters was divided in two atom positions, H3a and H3b with isotropic and at the same time equal mean-square displacement parameters (see Fig. 4.13). In consequence of dividing the H3-atom position into two, the bifurcated N–H$\cdots$O hydrogen bond changed to a single one. Moreover, when the

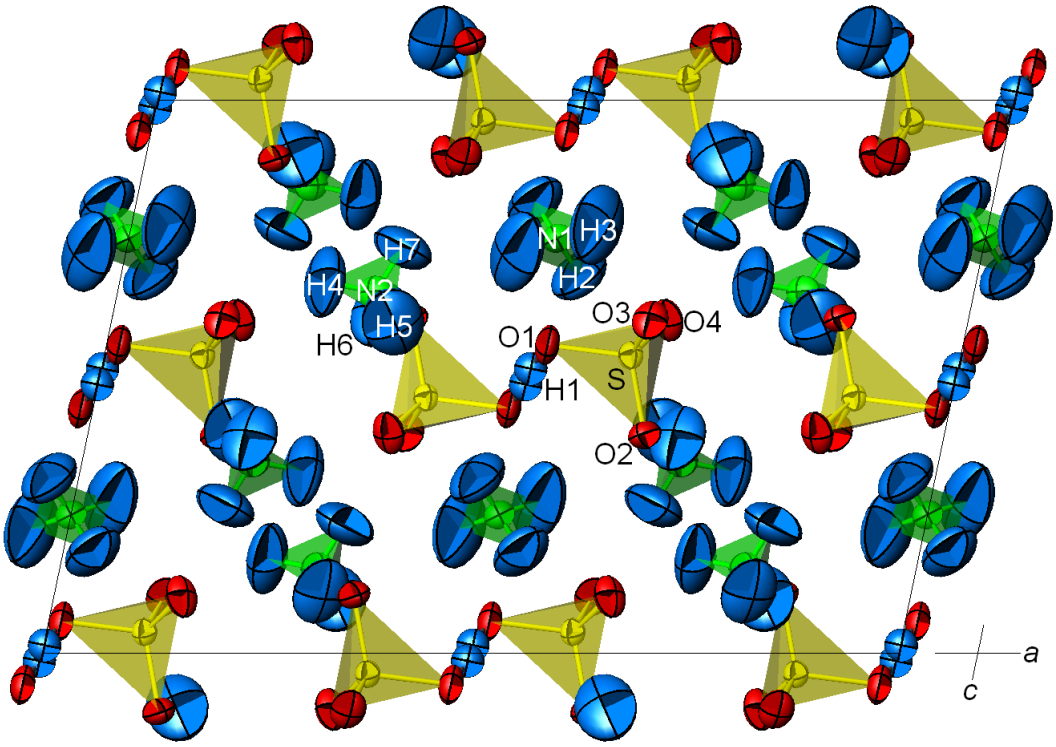

Figure 4.12: Unit cell of monoclinic TAHS-II (view along [010]). Displacement ellipsoids are drawn at the 50 % probability level.

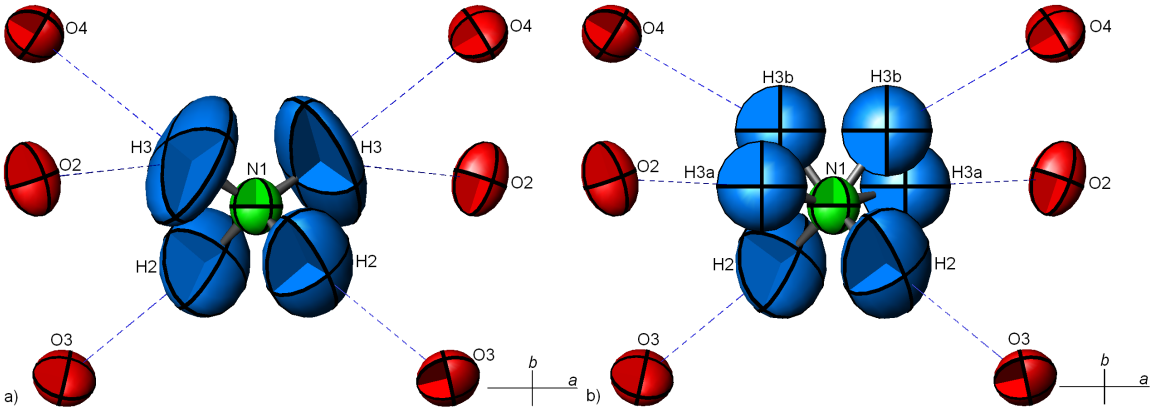

Figure 4.13: $N1H_4$ group in TAHS-II. a) Bifurcated N–H···O hydrogen bonds with the H3 atoms. The mean-square displacement parameters of H3 atoms are strongly enlarged. b) The splitting of the H3-atom position with equal isotropic mean-square displacement parameters gives rise to single N–H···O hydrogen bonds around the $N1H_4$ group. Displacement ellipsoids are drawn at the 50 % probability level.

Table 4.6: Crystal data and refinement details of TAHS-II of the neutron single-crystal diffraction study.

Chemical formula	$HO_8S_2{\cdot}3H_4N$
M_r	247.25
Crystal system	Monoclinic
Space group	$C2/c$
Temperature (K)	295
a, b, c (Å)	15.431 (8), 5.861 (3), 10.169 (5)
$\beta(^\circ)$	101.83 (5)
V (Å^3)	899.9 (8)
Z	4
D_x (Mg m^{-3})	1.825
Data collection	
No. of measured, independent and observed $[I > 3\sigma(I)]$ reflections	1169, 1143, 674
R_{int}	0.0391
$\Theta_{max}(^\circ)$	37.47
Refinement	
$R[F^2 > 3\sigma(F^2)]$	0.0742
$wR(F^2)$	0.1335
S	2.61
Extinction method	B-C type I Lorentzian isotropic [37]
Extinction coefficient	550 (60)
No. of reflections	1143
No. of parameters	108
$\Delta\rho_{max}, \Delta\rho_{min}$ (fm·Å^{-3})	0.95, -1.13

site occupancy of the H3a and H3b are additionally freely refined, restraining that the sum of both occupancies should be one, the site occupancy proportion of H3a : H3b results in 0.55 (2) : 0.45 (2). The slight higher occupation probability refers to the shorter (somewhat stronger) N–H$\cdots$O hydrogen bond. This description gives a final weighted R factor of 0.1322 using 118 parameters. The bond distances and angles from both models are listed and compared in Table 4.8.

Table 4.7: Refinement results of TAHS-II. The U-values are given in Å^2.

Atom	x	y	z	Occ.	$U_{11}/Uiso$	U_{22}	U_{33}	U_{12}	U_{13}	U_{23}
S	0.1146 (3)	0.2186 (9)	0.4619 (5)	1	0.022 (2)	0.028 (2)	0.027 (3)	0 (n.s.)	0.006 (2)	0 (n.s.)
N1	0.5	0.2299 (5)	0.25	1	0.031 (1)	0.036 (1)	0.028 (1)	0	0.002 (1)	0
N2	0.1991 (1)	0.2765 (3)	0.1530 (2)	1	0.041 (1)	0.034 (1)	0.036 (1)	-0.007 (1)	0.007 (1)	0 (n.s.)
O1	0.0148 (2)	0.1851 (5)	0.4428 (3)	1	0.020 (1)	0.054 (2)	0.055 (2)	0 (n.s.)	0.004 (1)	0 (n.s.)
O2	0.1503 (2)	0.2230 (5)	0.6053 (3)	1	0.036 (1)	0.060 (2)	0.026 (1)	-0.008 (1)	0 (n.s.)	0 (n.s.)
O3	0.1288 (2)	0.4336 (5)	0.3983 (3)	1	0.044 (2)	0.036 (1)	0.053 (2)	0.003 (1)	0.005 (1)	0.017 (1)
O4	0.1490 (2)	0.0273 (5)	0.3981 (3)	1	0.040 (1)	0.036 (2)	0.062 (2)	0 (n.s.)	0.020 (1)	-0.018 (1)
H1	0.0009 (7)	0.043 (1)	0.486 (1)	1/2	0.038 (2)					
H2	0.4654 (6)	0.133 (2)	0.184 (1)	1	0.091 (5)	0.132 (8)	0.091 (6)	0 (n.s.)	-0.018 (4)	-0.044 (6)
H3	0.4568 (7)	0.308 (3)	0.274 (2)	1	0.095 (6)	0.19 (1)	0.22 (1)	0.057 (7)	0.010 (8)	-0.10 (1)
H4	0.2603 (5)	0.309 (2)	0.171 (1)	1	0.057 (4)	0.130 (8)	0.18 (1)	-0.023 (5)	0.016 (5)	-0.074 (7)
H5	0.1711 (8)	0.391 (2)	0.099 (1)	1	0.137 (8)	0.126 (9)	0.16 (1)	0.052 (7)	0.037 (7)	0.078 (8)
H6	0.1898 (6)	0.131 (2)	0.112 (1)	1	0.103 (6)	0.075 (5)	0.144 (9)	-0.020 (4)	0 (n.s.)	-0.057 (5)
H7	0.1780 (7)	0.280 (2)	0.233 (1)	1	0.132 (7)	0.19 (1)	0.066 (5)	-0.028 (7)	0.049 (6)	0 (n.s.)

The bond distances (Å) and angles (°) of TAHS-II.

Bond distances				Bond angles			
S–O1	1.525 (5)	N1–H2	0.96 (1)	O1–S–O2	107.2 (4)	H2–N1–H3'	117 (1)
S–O2	1.450 (6)	N1–H3	0.88 (1)	O1–S–O3	107.2 (3)	H3–N1–H3"	118 (1)
S–O3	1.453 (6)	N2–H4	0.945 (8)	O1–S–O4	107.2 (3)	H4–N2–H5	107 (1)
S–O4	1.450 (6)	N2–H5	0.92 (1)	O2–S–O3	111.8 (4)	H4–N2–H6	108.7 (9)
O1–H1	0.98 (1)	N2–H6	0.949 (9)	O2–S–O4	111.5 (3)	H4–N2–H7	110 (1)
H1–H1	0.59 (1)	N2–H7	0.94 (1)	O3–S–O4	111.7 (4)	H5–N2–H6	113 (1)
O1–O1	2.548 (5)			H2–N1–H2'	106.8 (9)	H5–N2–H7	108 (1)
				H2–N1–H3	99 (1)	H6–N2–H7	111 (1)

Table 4.8: N–H···O hydrogen bond distances (Å) and angles (°) of $N1H_4$ group.

N–H···O	N–H	H···O	N–O	angle
N1–H2···O3	0.96 (1)	1.92 (1)	2.831 (4)	158.9 (9)
N1–H3···O2	0.88 (1)	2.26 (1)	3.003 (4)	142 (1)
N1–H3···O4	0.88 (1)	2.50 (1)	3.028 (4)	120 (1)
N1–H2···O3	0.97 (1)	1.90 (1)	2.833 (3)	159.1 (9)
N1–H3a···O2	0.99 (2)	2.02 (2)	3.004 (3)	171 (2)
N1–H3b···O4	0.93 (2)	2.24 (2)	3.024 (3)	141 (2)

In the case of the $N2H_4$ group which is located on a general position, there are eight O-atom neighbours in the surrounding for possible N–H···O hydrogen bonds. Each H atom forms bifurcated N–H···O hydrogen bonds which are regarded as being in competition at room temperature. The N–H bond lengths as well as the N–H···O bond distances and angles are given in Table 4.9 for this $N2H_4$ group.

Table 4.9: N–H···O hydrogen bond distances (Å) and angles (°) of $N2H_4$ group.

N–H···O	N–H	H···O	N–O	angle
N2–H4···O2	0.945 (8)	2.41 (1)	3.017 (5)	121.6 (9)
N2–H4···O4	0.945 (8)	2.12 (1)	2.903 (4)	139.4 (9)
N2–H5···O2	0.92 (1)	2.29 (1)	3.042 (5)	140 (1)
N2–H5···O3	0.92 (1)	2.26 (1)	3.101 (5)	153 (1)
N2–H6···O2	0.949 (9)	2.16 (1)	3.037 (5)	153.6 (9)
N2–H6···O4	0.949 (9)	2.33 (1)	3.109 (5)	139.0 (8)
N2–H7···O3	0.94 (1)	2.18 (1)	3.059 (5)	157 (1)
N2–H7···O4	0.94 (1)	2.35 (1)	3.119 (5)	140 (1)

Rigid-body analysis of the NH_4 groups

A rigid-body refinement was performed for a better comprehension of the motional behaviour of the ammonium groups. A refinement model with anisotropic mean-square displacements for H atoms was chosen for both NH_4 groups. The N1 and N2 atoms were defined as molecule-fixed origins. Instead of refining harmonic ADPs of N and H atoms **T**, **L** and **S** parameters of the rigid-body NH_4 groups were used and refined. The N1 atom is positioned on a twofold axis and hence the total number of **T**, **L** and **S** tensor parameters was reduced to 13. The final weighted R factor of the rigid-body refinement yields 0.142 with 105 parameters. The **T** and **L** tensors are converted to the crystallographic coordinate system and given in Table 4.10. While the translational

motion of the ammonium groups is considerably reduced for TAHS-II with respect to the high-temperature phase, the amplitudes of the librational motion strongly increased at room temperature. In the high-temperature phase I, the NH_4 groups are positioned on a special position with site symmetry $\bar{3}m$ and $3m$ for N1 and N2 atoms, respectively, which influences the large number of split H atoms around N. The reorientation of these groups takes place between different H atoms, however the freedom of libration is limited to some extent due to the high site symmetry. On the other hand, the ammonium groups at room temperature have lower site symmetry and therefore allow a greater degree of librational motion. Furthermore, the competing N–H$\cdots$O hydrogen bonds with surrounding SO_4 groups strengthen the large amplitudes of libration. As can be seen in Table 4.10, the translational and especially the librational motion at room temperature is clearly anisotropic. The $N1H_4$ group, though on a special position, shows remarkably higher libration amplitudes in the crystallographic **a** direction, because two nearby O neighbours form competing N–H$\cdots$O hydrogen bonds. The almost isotropically distributed O atoms around $N2H_4$ explain the rather small motional variances of these ammonium groups.

Table 4.10: **T** (Å^2) and **L** (deg^2) tensors of the NH_4 groups of TAHS-II.

	$N1H_4$ group	$N2H_4$ group
T11	0.030 (1)	0.039 (1)
T22	0.035 (1)	0.033 (1)
T33	0.028 (1)	0.034 (1)
L11	1210 (90)	650 (30)
L22	380 (70)	430 (30)
L33	600 (60)	370 (30)

Verification of a possible modulation in TAHS-II at room temperature

In the structure analyses of TAHS by X-ray single-crystal diffraction [8], a possible modulation of the crystal structure was reported. The authors observed additional weak interlayered reflections for the room and low temperature phases of TAHS. In order to verify this observation, similar X-ray single-crystal diffraction experiments were performed at room temperature, using an image-plate diffractometer (STOE-IPDS II, with MoKα radiation). The observed weak reflections disappeared when lowering the voltage to 30 kV (the energy of MoKα is 17.444 keV), which is clearly an indication of a $\lambda/2$ contamination effect (Fig. 4.14).

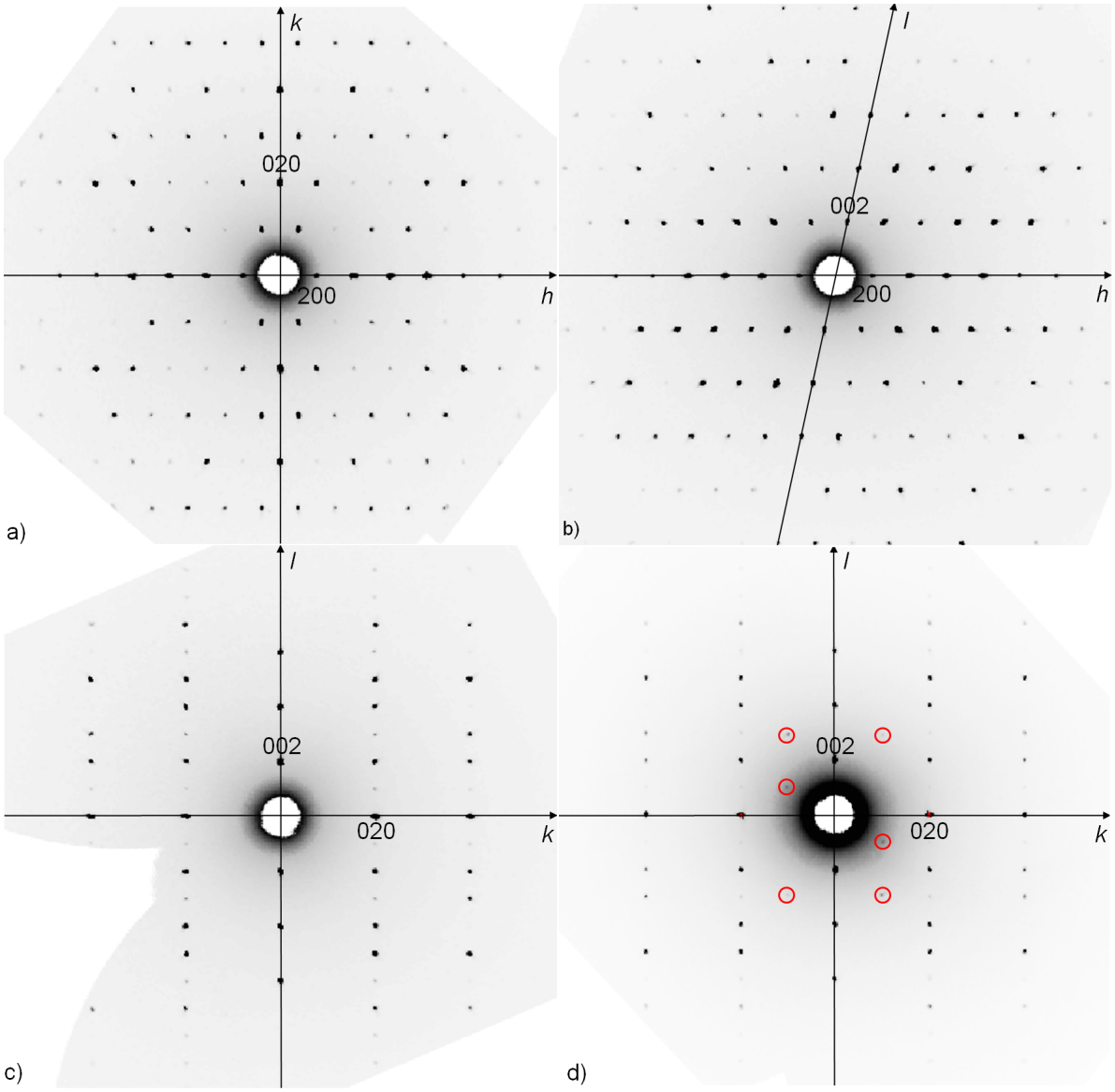

Figure 4.14: Reflections of TAHS-II at room temperature using the image-plate diffractometer (STOE-IPDS II, 30 kV). a) $hk0 : h + k = 2n$ b) $h0l : h, l = 2n$ c) $0kl : k = 2n$ d) $0kl$ at 50 kV with $k = 2n + 1$ as a $\lambda/2$ contamination effect.

4.3 Low-temperature phase III

The crystal structure of TAHS-III is monoclinic, space group symmetry $P2/n$ (No.13) with lattice parameters $a = 15.473\,(8), b = 5.849\,(3), c = 10.131\,(5)$ Å and $\beta = 101.75\,(5)^\circ$ at 250 K. For a structural investigation of TAHS-III with respect to proton ordering in this phase, single-crystal neutron diffraction measurements were carried out at two different temperatures, 250 K and 150 K, near the II/III- and the III/IV-phase transitions, respectively. The II/III-phase transition at 265 K shows the following direct group-subgroup relation between the space groups of the TAHS-II and III:

$$C2/c \text{ (Phase II)} \leftarrow k[2] \rightarrow P2/n \text{ (Phase III)}$$

The space group $P2/n$ is a 'klassengleiche' subgroup of $C2/c$ of index 2. The direct group-subgroup relation is a necessary precondition for a second-order phase transition. For the crystal structure refinement at 250 K, the atom positions of TAHS-II were transformed according to the group-subgroup relation into the new atomic coordinates for TAHS-III. Due to the symmetry reduction from the C-centred lattice to a primitive one, the inversion centre in the middle of the $(SO_4)H(SO_4)$ dimer at room temperature disappears in TAHS-III. Therefore, an asymmetric O–H$\cdots$O bond is formed in phase III. There are two symmetrically independent SO_4 groups and four NH_4 groups. Two NH_4 groups are located on special positions with twofold site symmetry, the other two on general positions. It is known from earlier work that the II/III-phase transition has a second-order character [2]. This character is confirmed by a continuous increase of Bragg reflection intensities for $T < T_c$, which will be discussed in more detail in the next chapter. A continuous change of H-ordering can also be found in the crystal structure analysis of the TAHS-III phase.

A continuous H-ordering in TAHS-III

Corresponding to the assumption of an order-disorder II/III-phase transition, the site occupancy of the split proton positions of the $(SO_4)H(SO_4)$ dimer was refined in the neutron structure analysis of TAHS-III. For this, the split H-atom positions were taken from those obtained for TAHS II at room temperature. They were kept fixed in the refinement with equal isotropic mean-square displacement parameters. A further constraint was that the sum of the refined site occupancies for both split H-positions had to be one. The result indicated an increase of the H-ordering in the $(SO_4)H(SO_4)$ dimer with decreasing temperature (Fig. 4.15). The degree of order was zero for TAHS-II

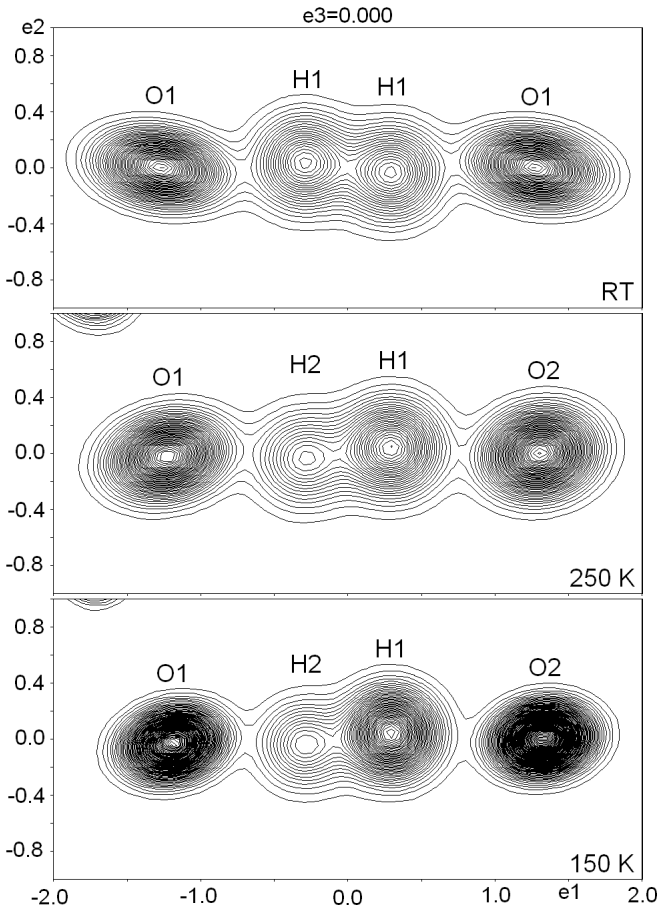

Figure 4.15: An increase of the H-ordering with decreasing temperature. 50 % : 50 % site occupancy of split H atom positions at room temperature. 35 % : 65 % at 250 K. 25 % : 75 % at 150 K. The contours (absolute values of the neutron scattering lengths) are drawn at a step of 0.2 fm·Å^{-3}.

at room temperature (fully disordered state with 50 % : 50 % site occupancy factor for both split H positions). As temperature decreases within the TAHS-III phase, the degree of order increases with the continuous growth of the H1-atom site occupancy factor. The 65 %-site occupancy at 250 K meets the degree of order of 30 % and those of 75 % at 150 K corresponds to 50 %. Fig. 4.16 shows the degree of order as a function of temperature in TAHS-III (cf. chapter 5.3). The O–O bond distance of the $(SO_4)H(SO_4)$ dimer becomes shorter with decreasing temperature. With the vanishing of the inversion centre, the O1–H2 and O2–H1 bond lengths became different.

Concerning the NH_4 groups in this phase, the changes appear more significant for those groups on general positions than for those on special positions. The ADPs of

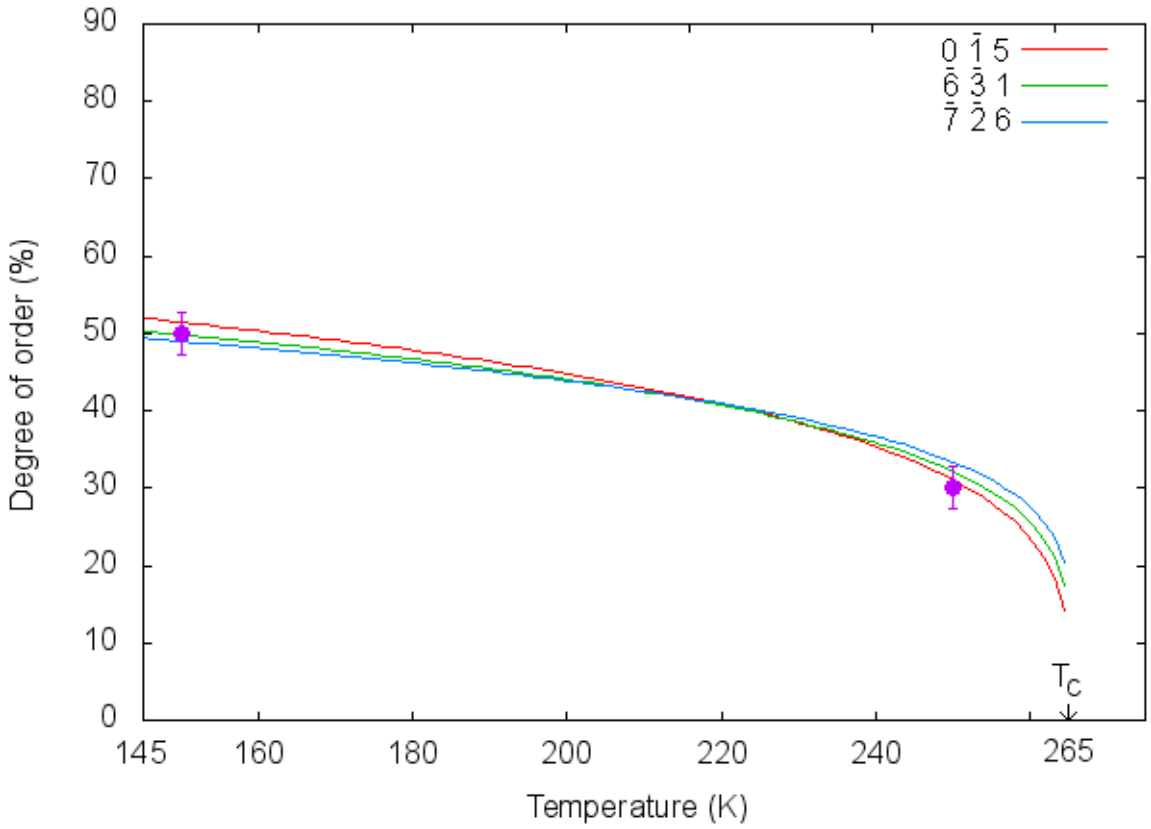

Figure 4.16: Degree of order calculated from the development of the Bragg reflection intensities of the superstructure reflections $(0\bar{1}5, \bar{6}\bar{3}1, \bar{7}\bar{2}6)$ in TAHS-III as a function of temperature. The values from the refinement of the site occupancies of split H-positions at 250 K and 150 K are marked with a closed circle.

$N3H_4$ and $N4H_4$ get distinctly smaller as the temperature decreases, whereas the NH_4 groups on a special position (site symmetry: 2) show little change in their ADPs. The equivalent U-values of each NH_4 group at 250 K and 150 K are presented in Fig. 4.17. All the equivalent U-values of nitrogen are similar and the largest equivalent U-values belong to H5 and H6 bonded to N atoms on a special position. Like at room temperature (TAHS-II), there exist two competing N–H$\cdots$O bonds and hence these H atoms have strongly enlarged U-values. The analysis of those H atoms by splitting their positions will be discussed later in detail. From the diagram in Fig. 4.17, it is easy to notice that the equivalent U-values of H atoms around N3 and N4 reveal a clear drop at 150 K. This suggests a freezing of a reorientational motion of these ammonium groups. A limitation of mobility may be caused by the shortening of the bond distances between H atoms of the ammonium groups and surrounding O atoms of the SO_4 tetrahedra. Compared to the environmental situation of these ammonium groups on a general

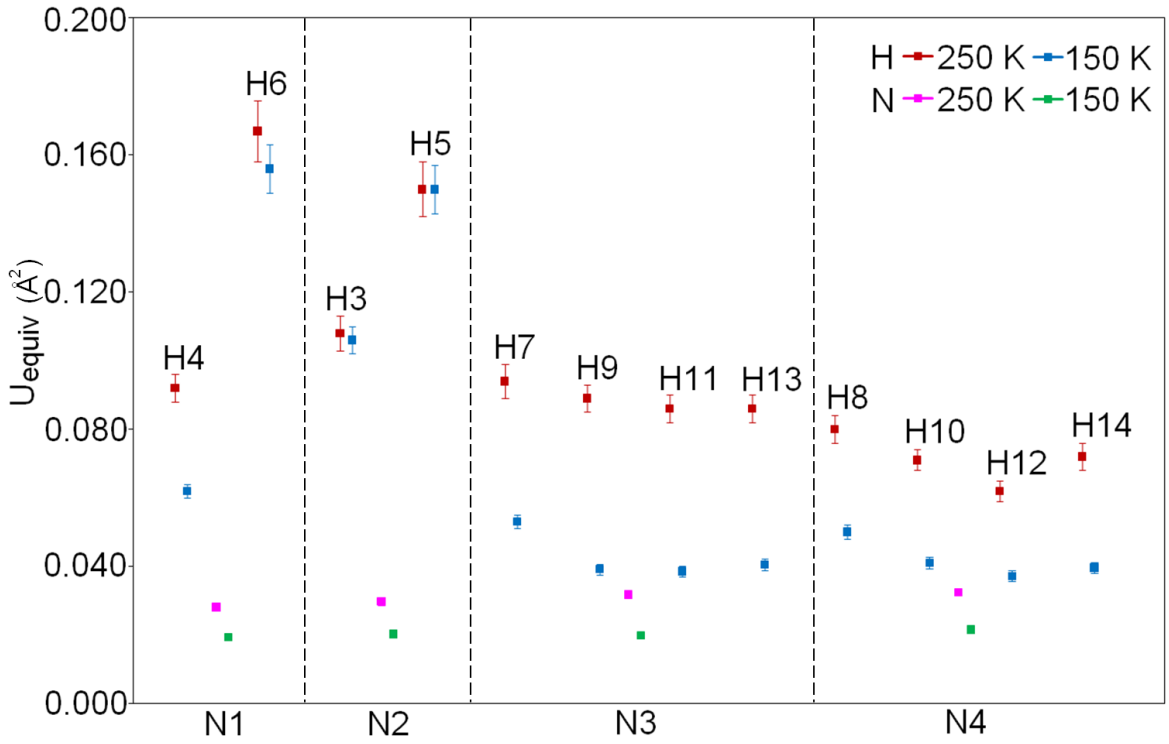

Figure 4.17: The equivalent U-values for N and H atoms of different NH_4 groups at 250 and 150 K in TAHS-III are plotted.

position at room temperature, where more or less competing N–H···O hydrogen bonds with a bifurcation are observed, shorter, and hence stronger, single bonds are mainly formed in TAHS-III. This results in a preferred orientation of these NH_4 groups. The N–H bond lengths, N–H···O bond distances and angles are listed in Table 4.11. As can be seen, all the H···O bonds get stronger with decreasing temperature and thus the relevant N–H bond lengths become longer. Interestingly, the ammonium groups on a special position still tend to have rather competing N–H···O hydrogen bonds and therefore large ADPs in TAHS-III, whereas those on a general position exhibit a stronger bonding and seem to freeze with a preferred orientation, because their ADPs get smaller. However, between the competing N–H···O hydrogen bonds for N1 and N2, the weaker bonding gets weaker and hence longer and the stronger one becomes even stronger, and thus shorter with decreasing temperature. From that, it can be assumed that like for other ammonium groups, those on a special position may also form stronger single hydrogen bonds with neighbouring O atoms at lower temperatures and freeze in a certain preferred orientation. Fig. 4.18 and 4.19 show the ammonium groups at 150 K, on special and general positions, respectively, with adjacent O atoms. There is still

Table 4.11: N–H···O hydrogen bond distances (Å) and angles (°) of NH_4 groups in TAHS-III. The first line for each bond gives the values at 250 K whereas the second line represents the equivalent values at 150 K.

N–H···O	N–H	H···O	N–O	angle
N1–H4···O5	0.99 (1)	1.89 (1)	2.831 (5)	159 (1)
	1.002 (7)	1.850 (8)	2.817 (4)	161.5 (7)
N1–H6···O4	0.92 (2)	2.20 (2)	2.972 (5)	141 (2)
	0.95 (2)	2.17 (2)	2.953 (4)	139 (1)
N1–H6···O7	0.92 (2)	2.44 (2)	3.000 (5)	119 (2)
	0.95 (2)	2.44 (1)	2.993 (4)	117 (1)
N2–H3···O6	0.95 (1)	1.93 (1)	2.839 (5)	159 (1)
	0.97 (1)	1.93 (1)	2.838 (4)	155 (1)
N2–H5···O3	0.91 (2)	2.23 (2)	3.033 (5)	147 (2)
	0.94 (1)	2.18 (2)	3.024 (4)	149 (1)
N2–H5···O8	0.91 (2)	2.54 (2)	3.062 (5)	117 (2)
	0.94 (1)	2.55 (2)	3.075 (4)	116 (1)
N3–H7···O3	0.93 (1)	2.32 (1)	2.995 (5)	129 (1)
	0.974 (6)	2.248 (7)	2.990 (4)	132.1 (6)
N3–H7···O8	0.93 (1)	2.23 (1)	2.895 (5)	128 (1)
	0.974 (6)	2.261 (8)	2.900 (4)	122.1 (5)
N3–H9···O4	1.02 (1)	1.90 (1)	2.912 (5)	170.5 (9)
	1.033 (6)	1.836 (6)	2.864 (4)	173.8 (5)
N3–H11···O8	1.01 (1)	1.96 (1)	2.957 (5)	170 (1)
	1.037 (5)	1.869 (6)	2.905 (4)	178.3 (5)
N3–H13···O7	0.98 (1)	1.97 (1)	2.942 (5)	170 (1)
	1.020 (6)	1.864 (6)	2.876 (4)	170.7 (5)
N4–H8···O4	0.99 (1)	2.52 (1)	3.054 (5)	113.4 (9)
	0.997 (7)	2.519 (7)	3.059 (4)	113.6 (5)
N4–H8···O7	0.99 (1)	2.03 (1)	2.915 (5)	147 (1)
	0.997 (7)	2.020 (8)	2.906 (4)	146.8 (6)
N4–H10···O5	0.98 (1)	1.94 (1)	2.910 (5)	172 (1)
	1.026 (5)	1.841 (6)	2.862 (4)	172.7 (6)
N4–H12···O3	1.027 (8)	1.884 (9)	2.894 (5)	167.1 (9)
	1.038 (5)	1.820 (6)	2.846 (4)	168.7 (5)
N4–H14···O6	1.02 (1)	1.91 (1)	2.922 (5)	175.4 (8)
	1.029 (6)	1.859 (6)	2.886 (4)	175.5 (5)

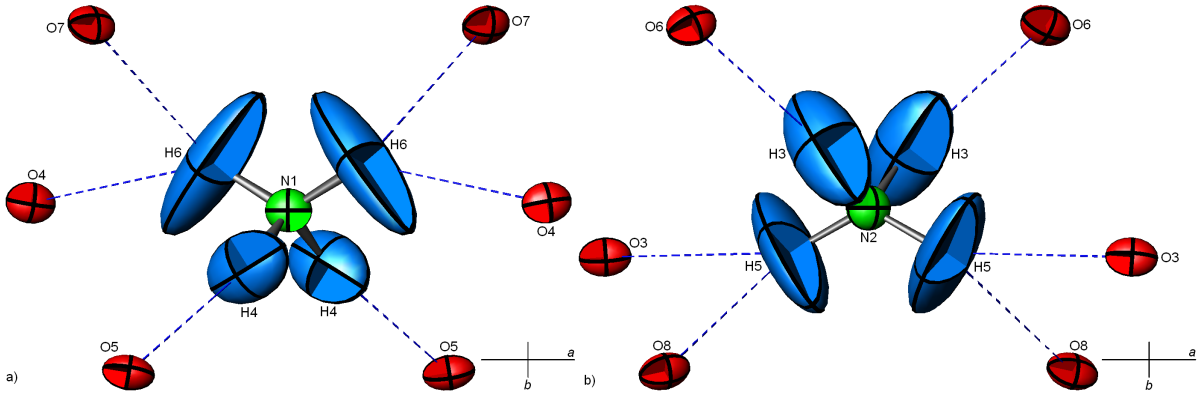

Figure 4.18: NH_4 groups on a special position with adjacent O atoms at 150 K. a) $N1H_4$ b) $N2H_4$. Displacement ellipsoids are drawn at the 50 % probability level.

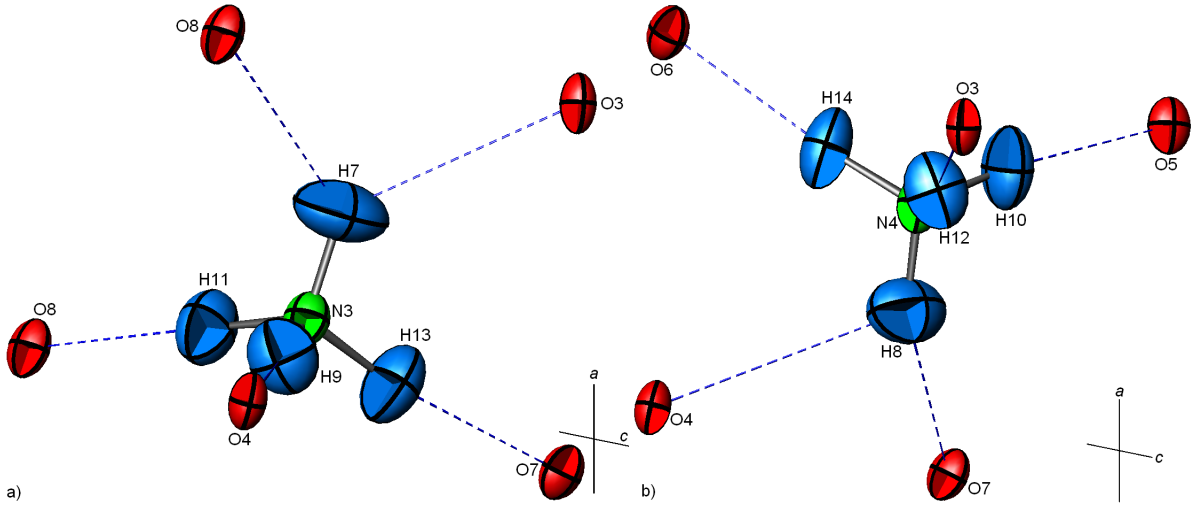

Figure 4.19: NH_4 groups on a general position with adjacent O atoms at 150 K. a) $N3H_4$ b) $N4H_4$. Displacement ellipsoids are drawn at the 50 % probability level.

one bifurcated H bond for H7 and H8 in the NH_4 groups on a general position. These bifurcated hydrogen bonds are weaker than the other single bonds and hence the bond lengths of N3–H7 and N4–H8 are the shortest. As can be read from Table 4.11, in the case of N3 the bifurcated hydrogen bonds are more or less competing and hence it is difficult to predict which of them is going to be stronger whereas those of N4 are both getting shorter with decreasing temperature and probably the shorter one will remain at lower temperatures. The refinement details and results for TAHS-III are given in Table 4.12– 4.15 and the unit cell of TAHS-III is shown in Fig. 4.20.

NH_4 groups on a special position

The splitting of H5- and H6-atom positions are tested due to their strongly enlarged mean-square displacement parameters as well as having two nearest O atoms in the surroundings. For this, the isotropic and at the same time equally set ADPs are distributed to both split H atoms. In addition, the site occupancy factors of H5a/H5b and H6a/H6b are refined with the restriction of adding up to 100 % for each pair of split atoms. As a result, H5a and H5b have an isotropic U-value of 0.079 (4) at 250 K and 0.060 (2) at 150 K whereas U for H6a and H6b are 0.073 (4) at 250 K and 0.052 (2) at 150 K. Although both groups lie on a special position and there is little difference with respect to the anisotropic H atom refinement, the site occupancy of H5 and H6 differ distinctly. For both NH_4 groups on a special position, the site occupancy ratio for split H-positions remains almost constant with decreasing temperature; H6a:H6b equals 45 (2) %: 55 (2) % at 250 K and 43 (1) %: 57 (1) % at 150 K, whereas H5a:H5b yields 62 (2) %: 38 (2) % at 250 K and 62 (1) %: 38 (1)% at 150 K. The H atoms with higher site occupancy factor form the shorter H$\cdots$O bonds with the O neighbours. Regarding the previous refinement, where both, H5 and H6 were described with anisotropic ADPs, the total number of refinement parameters was reduced, but nevertheless the final results yield smaller weighted R factors. At 250 K the final weighted R factor was 0.1374 with 228 parameters (those with non-significant values are not excluded here) and at 150 K it was 0.1237 with the same number of parameters. The bond distances and angles of N–H$\cdots$O are listed in Table 4.16. With the splitting of H5- and H6-atom positions these ammonium groups form stronger N–H$\cdots$O bonds with surrounding O atoms, and thus, the relevant N–H bond lengths increase, even more so with decreasing temperature. The N1–H6a$\cdots$O7 hydrogen bond weakens as temperature falls, whereas the N1–H6b$\cdots$O4 hydrogen bond becomes stronger. For the $N2H_4$ group, both hydrogen bonds involving H5a and H5b get stronger with decreasing temperature, however,

Table 4.12: Crystal data and refinement details of TAHS-III with neutron single-crystal diffraction.

Temperature (K)	250	150
Chemical formula	$HO_8S_2{\cdot}3H_4N$	
M_r	247.25	
Crystal system	Monoclinic	
Space group	$P2/n$	
a, b, c (Å)	15.473 (8), 5.849 (3)	15.534 (8), 5.825 (3)
	10.131 (5)	10.089 (5)
β (°)	101.75 (5)	101.52 (5)
V (Å^3)	897.7 (8)	894.5 (8)
Z	4	4
D_x (Mg m^{-3})	1.829 (2)	1.835 (2)
Data collection		
No. of measured, independent and observed $[I > 3\sigma(I)]$ reflections	1770, 1503, 1092	2379, 1689, 1470
R_{int}	0.0434	0.0239
Θ_{max}(°)	37.5	37.68
Refinement		
$R[F^2 > 3\sigma(F^2)]$	0.0660	0.0581
$wR(F^2)$	0.1402	0.1385
S	3.26	4.11
Extinction method	B-C type I Lorentzian isotropic [37]	
Extinction coefficient	8700 (400)	7300 (300)
No. of reflections	1503	1689
No. of parameters	208	208
$\Delta\rho_{max}, \Delta\rho_{min}$ (fm·Å^{-3})	0.97, -1.59	1.37, -1.99

Table 4.13: Refinement results of TAHS-III at 250 K. The U-values are given in Å^2.

Atom	x	y	z	Occ.	$U_{11}/Uiso$	U_{22}	U_{33}	U_{12}	U_{13}	U_{23}
S1	0.3614 (5)	0.467 (1)	0.4624 (6)	1	0.037 (4)	0.027 (3)	0.016 (3)	0.007 (2)	0.012 (3)	0 (n.s.)
S2	0.1343 (4)	0.031 (1)	0.5395 (7)	1	0.020 (3)	0.020 (3)	0.023 (3)	0.004 (2)	0 (n.s.)	0 (n.s.)
N1	0.75	0.0214 (6)	0.75	1	0.029 (2)	0.030 (2)	0.024 (2)	0	0.003 (1)	0
N2	0.75	0.4803 (6)	0.25	1	0.037 (2)	0.030 (2)	0.023 (2)	0	0.006 (1)	0
N3	0.4492 (2)	0.5239 (4)	0.1557 (3)	1	0.042 (2)	0.030 (1)	0.025 (1)	-0.007 (1)	0.009 (1)	0 (n.s.)
N4	0.0505 (2)	0.9689 (4)	0.8504 (3)	1	0.038 (2)	0.025 (1)	0.034 (2)	-0.006 (1)	0.007 (1)	-0.0026(9)
O1	0.2641 (2)	0.4315 (7)	0.4463 (4)	1	0.026 (2)	0.047 (2)	0.043 (2)	0 (n.s.)	0.009 (2)	0 (n.s.)
O2	0.2339 (2)	0.0620 (7)	0.5610 (4)	1	0.030 (2)	0.044 (2)	0.041 (2)	0 (n.s.)	0.008 (2)	0 (n.s.)
O3	0.4011 (2)	0.4449 (7)	0.6054 (3)	1	0.038 (2)	0.035 (2)	0.022 (2)	0 (n.s.)	0.003 (1)	0.003 (1)
O4	0.1012 (2)	0.0006 (6)	0.3945 (4)	1	0.042 (2)	0.038 (2)	0.019 (2)	-0.007 (2)	0.007 (2)	-0.003 (1)
O5	0.3769 (2)	0.6950 (6)	0.4132 (4)	1	0.044 (2)	0.025 (2)	0.032 (2)	0.003 (2)	0.004 (1)	0.006 (1)
O6	0.1200 (2)	0.8291 (6)	0.6154 (4)	1	0.041 (2)	0.029 (2)	0.032 (2)	0.006 (2)	0.010 (1)	0.011 (1)
O7	0.3956 (2)	0.2909 (6)	0.3836 (4)	1	0.041 (2)	0.030 (2)	0.036 (2)	0 (n.s.)	0.018 (1)	-0.011 (1)
O8	0.0982 (2)	0.2365 (6)	0.5884 (4)	1	0.038 (2)	0.027 (2)	0.042 (2)	0.004 (1)	0.016 (1)	-0.006 (1)
H1	0.2489	0.2061	0.5143	0.65 (1)	0.040 (2)					
H2	0.2511	0.2939	0.4857	0.35 (1)	0.040 (2)					
H3	0.7138 (7)	0.382 (3)	0.187 (1)	1	0.068 (6)	0.14 (1)	0.097 (8)	0 (n.s.)	-0.024 (5)	-0.041 (9)
H4	0.7849 (8)	0.114 (2)	0.823 (1)	1	0.103(8)	0.090 (7)	0.060 (5)	0.011 (6)	-0.036 (5)	-0.025 (6)
H5	0.705 (1)	0.556 (3)	0.274 (2)	1	0.073 (8)	0.15 (1)	0.22 (2)	0.046 (8)	0 (n.s.)	-0.08 (1)
H6	0.795 (1)	0.946 (4)	0.722 (2)	1	0.077 (8)	0.23 (2)	0.19 (2)	0.059 (9)	0 (n.s.)	-0.12 (2)
H7	0.5100 (8)	0.538 (2)	0.180 (2)	1	0.053 (6)	0.093 (8)	0.13 (1)	0 (n.s.)	0 (n.s.)	-0.036 (7)
H8	0.9872 (7)	0.930 (2)	0.840 (1)	1	0.053 (5)	0.094 (7)	0.095 (7)	-0.022 (5)	0.021 (5)	-0.040 (6)
H9	0.4259 (8)	0.685 (2)	0.130 (1)	1	0.110 (9)	0.062 (6)	0.085 (7)	0 (n.s.)	0 (n.s.)	0.010 (5)
H10	0.0804 (7)	0.880 (2)	0.9281 (9)	1	0.097 (7)	0.061 (5)	0.057 (5)	0.008 (5)	0.022 (5)	0 (n.s.)
H11	0.4377 (7)	0.413 (2)	0.078 (1)	1	0.092 (7)	0.083 (7)	0.089 (7)	-0.035 (6)	0.035 (6)	-0.042 (6)
H12	0.0590 (6)	0.140 (1)	0.8702 (8)	1	0.087 (6)	0.033 (4)	0.060 (5)	0 (n.s.)	0 (n.s.)	-0.006 (3)
H13	0.4277 (8)	0.464 (2)	0.233 (1)	1	0.104 (8)	0.116 (8)	0.052 (5)	0 (n.s.)	0.045 (6)	0.017 (5)
H14	0.0721 (7)	0.925 (2)	0.765 (1)	1	0.104 (7)	0.062 (5)	0.058 (5)	-0.017 (5)	0.033 (5)	0 (n.s.)

Table 4.14: Refinement results of TAHS-III at 150 K. The U-values are given in Å^2.

Atom	x	y	z	Occ.	$U_{11}/Uiso$	U_{22}	U_{33}	U_{12}	U_{13}	U_{23}
S1	0.3602 (3)	0.4656 (8)	0.4630 (4)	1	0.021 (2)	0.014 (2)	0.009 (2)	0 (n.s.)	0.007 (2)	0 (n.s.)
S2	0.1338 (3)	0.0286 (8)	0.5391 (4)	1	0.016 (2)	0.015 (2)	0.011 (2)	0 (n.s.)	0.004 (2)	0 (n.s.)
N1	0.75	0.0227(4)	0.75	1	0.023 (1)	0.020 (1)	0.015 (1)	0	0.0026 (9)	0
N2	0.75	0.4804(4)	0.25	1	0.023 (1)	0.021 (1)	0.018 (1)	0	0.0063 (9)	0
N3	0.4497 (1)	0.5217 (3)	0.1573 (2)	1	0.0243 (9)	0.0180 (8)	0.0177 (8)	-0.0031 (6)	0.0057 (6)	0 (n.s.)
N4	0.0486 (1)	0.9678 (3)	0.8517 (2)	1	0.030 (1)	0.0181 (8)	0.0171 (9)	-0.0022 (6)	0.0051 (6)	0 (n.s.)
O1	0.2630 (2)	0.4288 (5)	0.4480 (3)	1	0.018 (1)	0.033 (2)	0.029 (1)	0 (n.s.)	0.006 (1)	0 (n.s.)
O2	0.2334 (2)	0.0602 (5)	0.5628 (3)	1	0.018 (1)	0.030 (1)	0.026 (1)	0 (n.s.)	0.005 (1)	-0.0018 (9)
O3	0.4005 (2)	0.4357 (4)	0.6066 (2)	1	0.029 (1)	0.016 (1)	0.011 (1)	0 (n.s.)	0.0031 (9)	0.0016 (7)
O4	0.1021 (2)	-0.0096 (4)	0.3938 (2)	1	0.027 (1)	0.018 (1)	0.012 (1)	0 (n.s.)	0.0056 (9)	0 (n.s.)
O5	0.3751 (2)	0.6991 (4)	0.4172 (2)	1	0.028 (1)	0.013 (1)	0.017 (1)	0.0023 (9)	0.0034 (8)	0 (n.s.)
O6	0.1194 (2)	0.8307 (4)	0.6202 (2)	1	0.028 (1)	0.018 (1)	0.016 (1)	0.0034 (9)	0.0072 (9)	0.0039 (8)
O7	0.3941 (2)	0.2949 (4)	0.3790 (2)	1	0.026 (1)	0.016 (1)	0.017 (1)	0.0015 (9)	0.0085 (8)	-0.0031 (8)
O8	0.0976 (2)	0.2408 (4)	0.5843 (2)	1	0.029 (1)	0.015 (1)	0.016 (1)	0.0036 (9)	0.0085 (8)	-0.0017 (8)
H1	0.2489	0.2061	0.5143	0.75 (1)	0.033 (1)					
H2	0.2511	0.2939	0.4857	0.25 (1)	0.033 (1)					
H3	0.7151 (7)	0.379 (2)	0.185 (1)	1	0.066 (5)	0.140 (9)	0.096 (7)	0.029 (6)	-0.023 (5)	-0.067 (7)
H4	0.7857 (5)	0.120 (1)	0.8227 (7)	1	0.059 (4)	0.059 (4)	0.055 (4)	0.009 (3)	-0.019 (3)	-0.019 (3)
H5	0.7029 (7)	0.557 (3)	0.275 (2)	1	0.055 (6)	0.16 (1)	0.22 (2)	0.045 (6)	0 (n.s.)	-0.12 (1)
H6	0.7942 (8)	0.942 (3)	0.717 (1)	1	0.097 (8)	0.22 (2)	0.13 (1)	0.103 (9)	-0.042 (7)	-0.11 (1)
H7	0.5133 (4)	0.530 (1)	0.1871 (7)	1	0.028 (3)	0.054 (4)	0.072 (4)	0 (n.s.)	0 (n.s.)	-0.009 (3)
H8	0.9850 (4)	0.930 (1)	0.8403 (7)	1	0.039 (3)	0.054 (3)	0.057 (4)	-0.005 (3)	0.010 (2)	-0.019 (3)
H9	0.4266 (4)	0.6866 (9)	0.1366 (5)	1	0.044 (3)	0.030 (3)	0.041 (3)	0.005 (2)	0.003 (2)	0 (n.s.)
H10	0.0809 (4)	0.8769 (9)	0.9338 (5)	1	0.062 (3)	0.034 (3)	0.025 (2)	0.004 (2)	0.006 (2)	0.007 (2)
H11	0.4339 (4)	0.4225 (9)	0.0704 (5)	1	0.048 (3)	0.038 (3)	0.032 (2)	-0.007 (2)	0.012 (2)	-0.008 (2)
H12	0.0590 (4)	0.1426 (8)	0.8676 (5)	1	0.050 (3)	0.022 (2)	0.036 (3)	0 (n.s.)	0 (n.s.)	0 (n.s.)
H13	0.4236 (4)	0.4479 (9)	0.2321 (5)	1	0.053 (3)	0.039 (3)	0.035 (3)	-0.006 (2)	0.022 (2)	0 (n.s.)
H14	0.0706 (4)	0.9184 (9)	0.7663(5)	1	0.062 (3)	0.035 (2)	0.025 (2)	-0.003 (2)	0.016 (2)	0 (n.s.)

Table 4.15: The bond distances (Å) and angles (°) of TAHS-III.

	250 K	150 K		250 K	150 K		250 K	150K
S1–O1	1.495 (8)	1.503 (6)	N3–H13	0.98 (1)	1.020 (6)	H4–N1–H6'	112 (2)	111 (1)
S1–O3	1.460 (7)	1.469 (5)	N4–H8	0.99 (1)	0.997 (7)	H6–N1–H6'	123 (2)	121 (1)
S1–O5	1.462 (8)	1.470 (5)	N4–H10	0.98 (1)	1.026 (5)	H3–N2–H3'	105 (1)	105 (1)
S1–O7	1.465 (8)	1.470 (5)	N4–H12	1.027 (8)	1.038 (5)	H3–N2–H5	95 (1)	97 (1)
S2–O2	1.523 (7)	1.530 (6)	N4–H14	1.02 (1)	1.029 (6)	H3–N2–H5'	120 (2)	118 (1)
S2–O4	1.465 (7)	1.467 (5)	O1–S1–O3	107.9 (5)	107.7 (3)	H5–N2–H5'	121 (2)	123 (1)
S2–O6	1.452 (7)	1.456 (5)	O1–S1–O5	108.7 (5)	108.6 (3)	H7–N3–H9	106 (1)	107.8 (5)
S2–O8	1.452 (7)	1.468 (5)	O1–S1–O7	108.2 (4)	108.3 (3)	H7–N3–H11	106 (1)	110.0 (6)
O1–H2	0.938 (4)	0.908 (3)	03–S1–O5	110.7 (4)	110.9 (3)	H7–N3–H13	108 (1)	108.7 (6)
O2–H1	1.016 (4)	1.033 (3)	O3–S1–O7	110.7 (5)	110.9 (3)	H9–N3–H11	113.6 (9)	109.5 (4)
H1–H2	0.5940 (5)	0.5915 (5)	O5–S1–O7	110.6 (5)	110.3 (3)	H9–N3–H13	112 (1)	111.6 (5)
O1–O2	2.541 (6)	2.524 (5)	O2–S2–O4	107.1 (5)	107.5 (4)	H11–N3–H13	111 (1)	109.2 (5)
N1–H4	0.99 (1)	1.002 (7)	O2–S2–O6	106.1 (4)	105.7 (3)	H8–N4–H10	105 (1)	106.9 (5)
N1–H6	0.92 (2)	0.95 (2)	O2–S2–O8	107.6 (4)	106.8 (3)	H8–N4–H12	109.2 (9)	110.9 (5)
N2–H3	0.95 (1)	0.97 (1)	O4–S2–O6	111.8 (4)	112.5 (3)	H8–N4–H14	109.9 (9)	109.3 (5)
N2–H5	0.91 (2)	0.94 (1)	O4–S2–O8	111.3 (4)	111.4 (3)	H10–N4–H12	110.0 (8)	110.2 (4)
N3–H7	0.93 (1)	0.974 (6)	O6–S2–O8	112.5 (5)	112.4 (4)	H10–N4–H14	111.3 (9)	109.9 (5)
N3–H9	1.02 (1)	1.033 (6)	H4–N1–H4'	113 (1)	111.1 (6)	H12–N4–H14	111.3 (8)	109.6 (5)
N3–H11	1.01 (1)	1.037 (5)	H4–N1–H6	99 (1)	101.8 (9)			

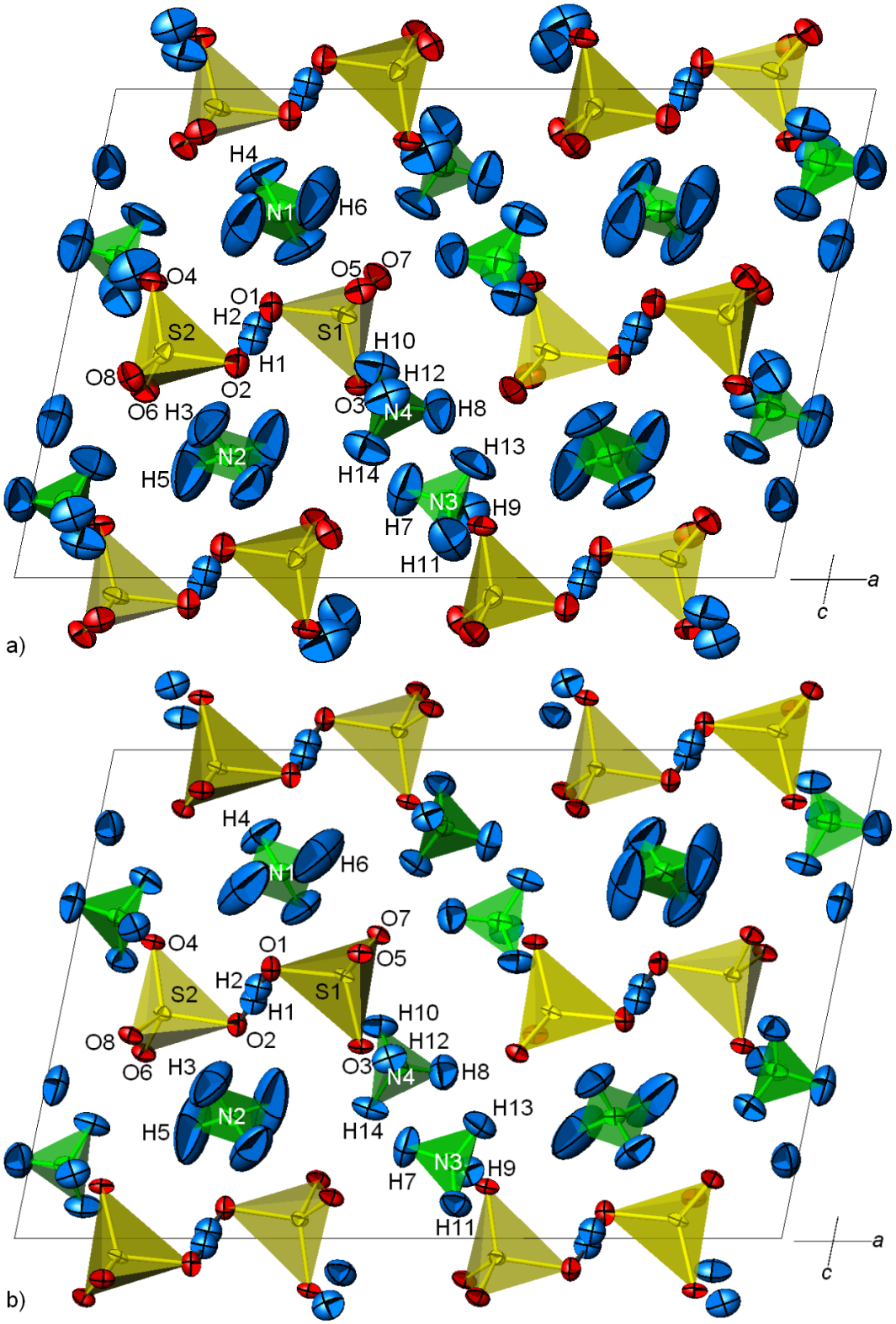

Figure 4.20: Unit cell of monoclinic TAHS-III ($P2/n$) at a) 250 K b) 150 K (view along [010]). Displacement ellipsoids are drawn at the 50 % probability level.

Table 4.16: N–H···O bond distances (Å) and angles(°) of NH_4 on a special position after splitting in TAHS-III. The second line gives the equivalent values at 150 K.

N–H··· O	N–H	H···O	N–O	angle
N1–H4···O5	0.99 (1)	1.89 (1)	2.831 (5)	159 (1)
	1.001 (6)	1.851 (7)	2.817 (3)	161.2 (6)
N1–H6a···O7	0.99 (2)	2.18 (2)	3.000 (5)	139 (2)
	0.98 (2)	2.26 (1)	2.993 (3)	130 (1)
N1–H6b···O4	1.02 (2)	1.96 (2)	2.974 (5)	171 (2)
	1.06 (1)	1.92 (1)	2.954 (3)	166.3 (9)
N2–H3···O6	0.96 (1)	1.93 (1)	2.838 (5)	159 (1)
	0.97 (1)	1.93 (1)	2.839 (3)	154.9 (9)
N2–H5a···O3	0.99 (2)	2.06 (2)	3.033 (5)	169 (2)
	1.01 (1)	2.02 (1)	3.024 (3)	171.5 (9)
N2–H5b···O8	0.96 (3)	2.22 (3)	3.063 (5)	146 (3)
	1.03 (2)	2.17 (2)	3.077 (4)	146 (1)

the H5a site has a larger occupancy factor. The illustration in Fig. 4.21 shows the split H5- and H6-atom positions of NH_4 groups on a special position with their oxygen neighbours at 150 K.

Rigid-body analysis of the NH_4 groups

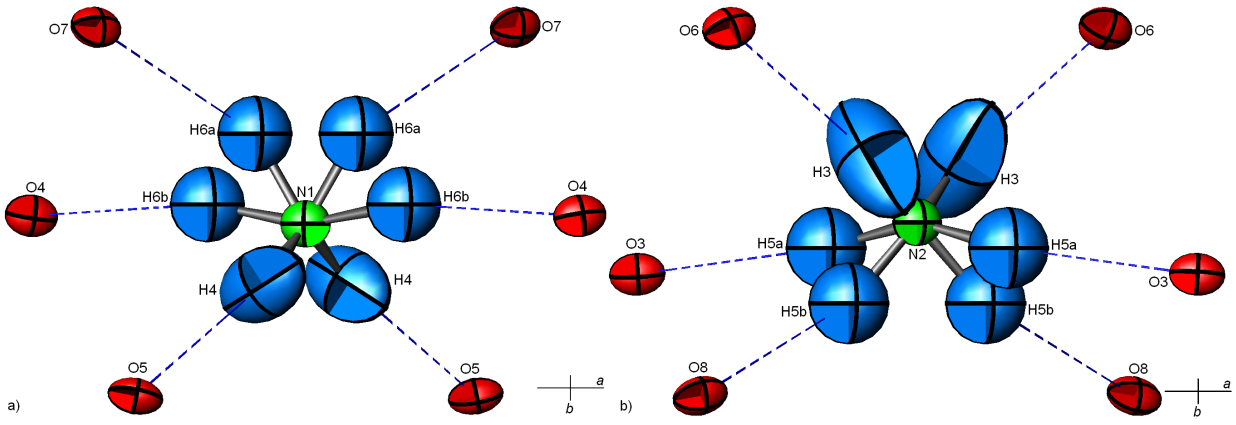

Figure 4.21: NH_4 groups on a special position with the splitting of H-atom positions at 150 K. a) $N1H_4$ b) $N2H_4$. The split H-atom positions are shown with their isotropic mean-square displacement parameters and the site occupancy factors are not considered in the illustration. Displacement ellipsoids are drawn at the 50 % probability level.

The mobility changes of the NH_4 groups in TAHS-III with decreasing temperature were also visible through the rigid-body analysis. For each NH_4 group, N was defined as a molecule fixed origin, and instead of mean-square displacement parameters for each N and H atoms, the **TLS** tensors of each molecule were refined. For the rest of the crystal structure of TAHS-III, the related refinement parameters remained unchanged, and only the ammonium groups were described as rigid-bodies. After the refinement, the **T** and **L** tensors were converted to the crystallographic coordinate system and are given in Table 4.17. On the whole, the translational motion decreases from 250 K to 150 K.

Table 4.17: **T** ($Å^2$) and **L** (deg^2) tensors of the NH_4 groups of TAHS-III.

		250 K	150 K			250 K	150 K
$N1H_4$	**T**11	0.028 (2)	0.022 (1)	$N3H_4$	**T**11	0.040 (2)	0.022 (1)
	T22	0.029 (2)	0.019 (1)		**T**22	0.028 (1)	0.018 (1)
	T33	0.022 (2)	0.014 (1)		**T**33	0.025 (1)	0.018 (1)
	L11	1100 (100)	950 (80)		**L**11	300 (20)	83 (7)
	L22	330 (60)	200 (30)		**L**22	290 (30)	140 (10)
	L33	580 (80)	570 (60)		**L**33	240 (30)	90 (10)
$N2H_4$	**T**11	0.034 (2)	0.021 (1)	$N4H_4$	**T**11	0.037 (2)	0.028 (1)
	T22	0.029 (2)	0.021 (1)		**T**22	0.025 (1)	0.017 (1)
	T33	0.020 (2)	0.016 (1)		**T**33	0.031 (2)	0.016 (1)
	L11	1500 (100)	1500 (100)		**L**11	130 (10)	74 (7)
	L22	300 (90)	340 (60)		**L**22	210 (20)	124 (9)
	L33	300 (60)	300 (50)		**L**33	200 (20)	90 (10)

At 150 K, both ammonium groups ($N1H_4$ and $N2H_4$) on a special position have slightly bigger translational movement in crystallographic **a** and **b** than **c** direction, whereas the other groups ($N3H_4$ and $N4H_4$) on a general position show stronger translations in **a** than in **b** and **c**. In the analysis of librational motion, the amplitudes do not always decrease with decreasing temperature. Within error bars, the $N1H_4$ and $N2H_4$ groups show no significant variation of the librations. In contrast to these two groups, the ammonium groups on a general position show a drastic reduction of librational amplitudes. This can be interpreted as a freezing of these groups in TAHS-III. Though the four ammonium groups are all symmetrically independent in TAHS-III, a tendency of similar motional behaviour is given for those on a special as well as general position. The final weighted R factor of the rigid-body refinement yields 0.1528 at 250 K and 0.1502 at 150 K with 202 parameters.

As in TAHS-II, single-crystal X-ray experiments on a STOE-IPDS II (MoKα) were performed to check for a possible modulation in TAHS-III. A potential $\lambda/2$ effect was suppressed by reducing the X-ray tube voltage to 30 kV. The result showed no additional interlayered reflections in the phase III (Fig. 4.22).

4.4 Low-temperature phase IV

The crystal structure of TAHS-IV was earlier reported as isostructural to that of TAHS-III with the space group symmetry $P2/n$ [8]. It was actually in this phase IV at 136 K, where the authors clearly observed some additional interlayered reflections using single-crystal X-ray diffraction. However, no adequate crystal structure refinement could be carried out with the additional reflections and hence a possible modulation of the crystal structure was suggested. As mentioned and shown above, we have not been able to confirm the existence of additional interlayered reflections from room temperature down to 150 K. By keeping the measurement conditions identical, the same experiments were performed at 136 K. The result showed some additional reflections which appeared only along the **k** direction in reciprocal space, at exactly half of the already indexed reflection positions (Fig. 4.23). Since the applied voltage of the Mo X-ray tube was sufficiently low at 30 kV to avoid the $\lambda/2$-contamination, the observed reflections were considered to be real. Therefore, we assumed a doubling of the unit cell in **b** direction. The observed reflection intensities of the superstructure were $\sim$ 300 times weaker than those of the strongest ones. With this previous information, a single-crystal neutron diffraction measurement was carried out on the four-circle diffractometer HEiDi at the FRM II in Garching. The existence range of the phase IV is very narrow ($\sim$ 8 K) and in addition, the next low-temperature phase transition IV/V shows a hysteresis of $\sim$ 5 K. Moreover, a twinning of the crystal structure occurs in phase V. In order to be sure that the neutron diffraction data collection takes place in the right phase, the doubling of the unit cell as well as the twinning of the next low-temperature phase V were considered and checked. For this, the sample was firstly cooled down until a splitting of reflections (twinning effect) was observed and then heated again to the vanishing point of the twinning. Thereafter, some of the superstructure reflections were checked for the verification of the presence of phase IV. The complete dataset was then collected up to $(\sin\Theta/\lambda)_{max} = 0.7$ Å at 138.5 K. In the case of single-crystal neutron diffraction, the measured intensities of additional superstructure reflections were $\sim$ 100 times smaller than those of the strongest ones, and these additional reflections dis-

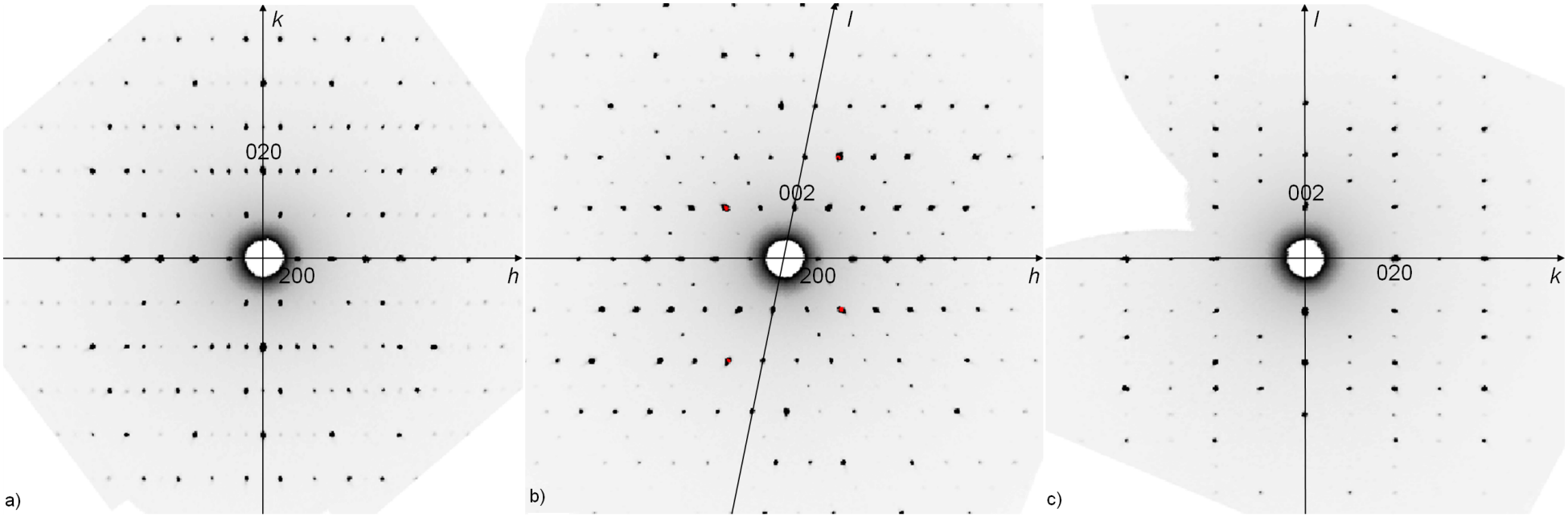

Figure 4.22: Reflections of TAHS-III at 150 K using an image-plate diffractometer (STOE-IPDS II). a) $hk0$ b) $h0l : h + l = 2n$ c) $0kl$.

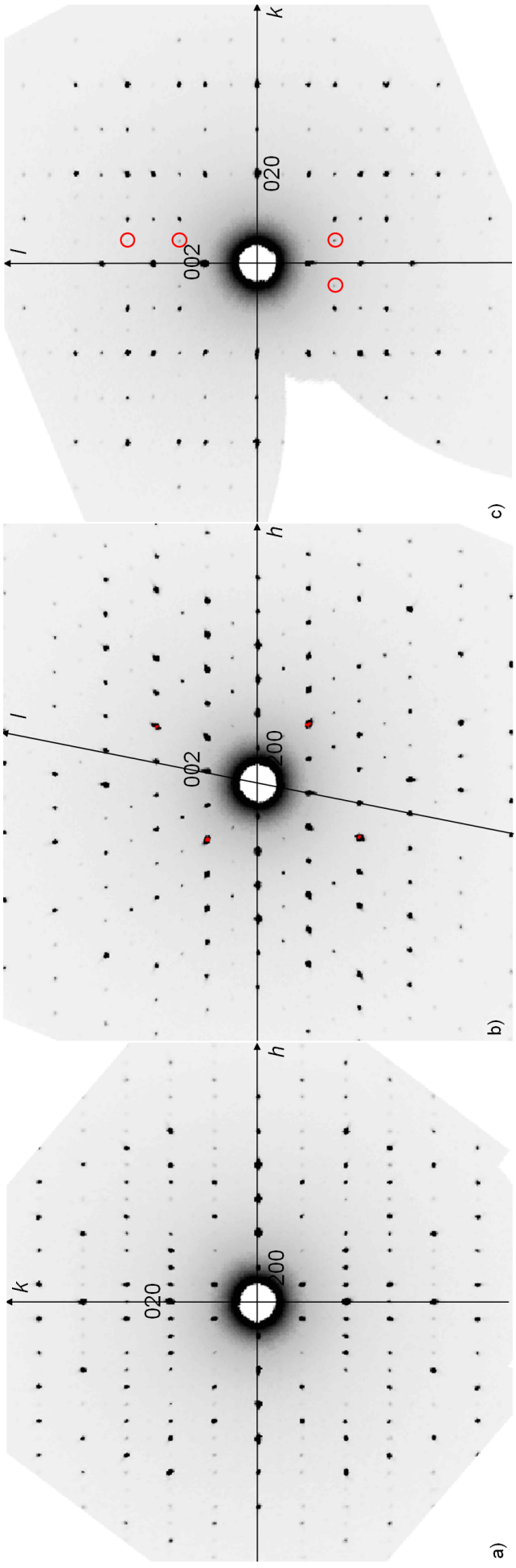

Figure 4.23: Reflections of TAHS-IV at 136 K using an image-plate diffractometer (STOE-IPDS II). Some of the additional interlayered reflections are marked with a circle. a) $hk0$ b) $h0l : h + l = 2n$ c) $0kl$.

appeared at the III/IV-phase transition, when the sample was heated again. While single-crystal X-ray diffraction with an image plate detector delivered clear evidence for the differences between the crystal structures of TAHS-III and IV, temperature-dependent X-ray powder diffraction showed only little changes at the III/IV-phase transition of TAHS, showing hardly any change regarding peak positions and profiles. However, the profile matching of the powder pattern at 138 K using the FullProf program [33] with a doubling of the unit cell in **b** direction, lowered the final weighted R factor by more than 10 % with respect to the refinement with a smaller unit cell. The crystal structure of TAHS-IV (neutron diffraction data) was therefore refined with a doubled monoclinic unit cell of space group symmetry $P2/n$ and lattice parameters: $a = 15.538\,(8), b = 11.641\,(6), c = 10.085\,(5)$ Å and $\beta = 101.46\,(5)^\circ$. The main focus of the crystal structure analysis in TAHS-IV was, to find out, why the unit cell is doubled in **b** direction. The crystal structure refinement was started with the atomic parameters taken from TAHS-III at 150 K. The superstructure reflections were weak and, thus, the collected data had certain limitations. In addition to this, the doubling of the unit cell increases the total number of atoms ($Z = 8$ instead of 4), leading to too many refinement parameters for the measured dataset. Hence, some restraints were needed in the refinement. At first, the unit cell was doubled and all the atomic positions and mean-square displacement parameters were refined as in TAHS-III. With this first refinement, no remarkable changes of the crystal structure of TAHS-IV could be detected in comparison to that of the phase III, apart from that the ADPs are now smaller. In the following, the doubling of the unit cell in **b** direction is carefully considered. As illustrated in Fig. 4.24, all symmetry elements at $\frac{1}{4}b'$ and $\frac{3}{4}b'$ disappear on doubling **b**. This leads to a symmetry inequality of the red and blue atom/molecule-pairs in the doubled unit cell: for simplification, only one inversion centre is drawn here at the $(1/2, 1/2, 1/2)$-position. Therefore, only the atomic positions were refined independently. This shifted the atoms into new positions. However, the ADPs of each atom could not be refined separately, due to the large number of parameters, and hence, they were restrained to be equal. On refining the ADPs, the atomic positions were fixed again to avoid possible large correlation effects. After that, the refined ADPs were kept constant and the atom positions were refined again. This whole procedure was repeated several times until the refinement converged. The unit cell of monoclinic TAHS-IV is shown in Fig. 4.25. The slightly reorientated SO_4 as well as NH_4 groups can best be recognized in an **a**,**c**-projection.

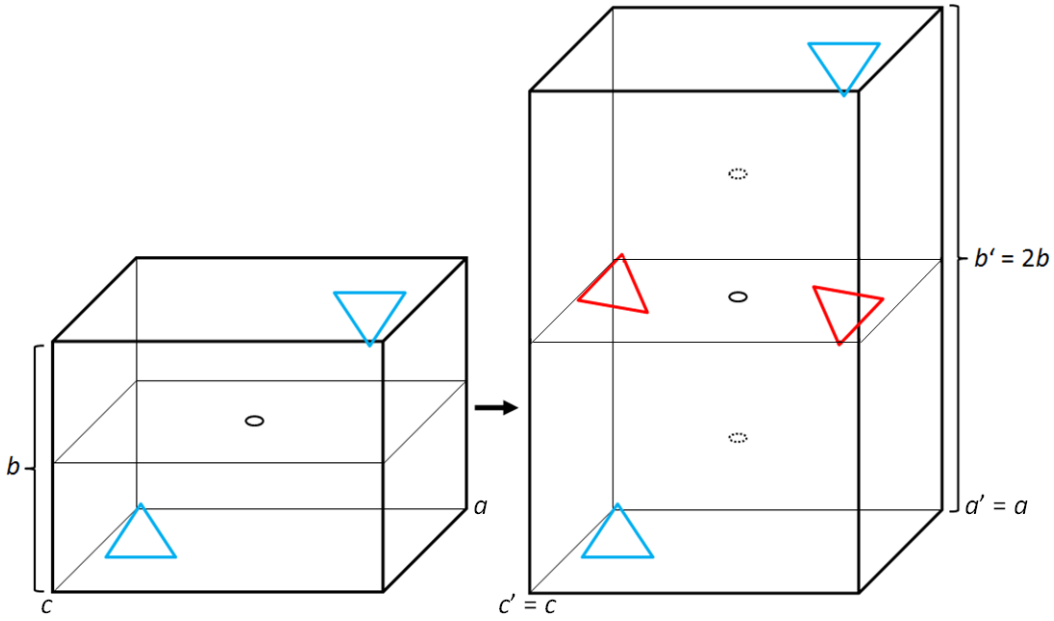

Figure 4.24: Doubling of the monoclinic unit cell in **b** direction and disappearance of inversion centres (dotted). Hence the red and blue atoms/molecules are not symmetry equivalent any more.

H-ordering in a $(SO_4)H(SO_4)$ dimer

Refinement of the atomic positions in TAHS-IV yields two different asymmetric O–H···O bonds of the $(SO_4)H(SO_4)$ dimers in the unit cell, with two unequal O–O distances. Due to this effect, the refinement of the site occupancy for the split H-atom positions in each $(SO_4)H(SO_4)$ dimer was treated individually. During the refinement, each split H-atom position was kept the same as in TAHS-II and III. The mean-square displacement parameters of those split positions were described isotropically and equally. Finally, the site occupancy was refined with its sum to be one as a constraint. The results are shown in Table 4.18 with corresponding bond lengths. Although the III/IV-phase transition of TAHS has a second-order character like the II/III-phase transition

Table 4.18: O–H···O bond distances (Å) and site occupancy of split H-atom positions in the $(SO_4)H(SO_4)$ dimers in TAHS-IV.

O1–H2	0.90 (2)	O9–H16	0.94 (2)
H2–H1	0.5911 (5)	H16–H15	0.5911 (5)
H1–O2	1.01 (2)	H15–O10	1.04 (2)
O1–O2	2.50 (2)	O9–O10	2.56 (2)
H1 : H2	0.71 (7) : 0.29 (7)	H15 : H16	0.73 (7) : 0.27 (7)

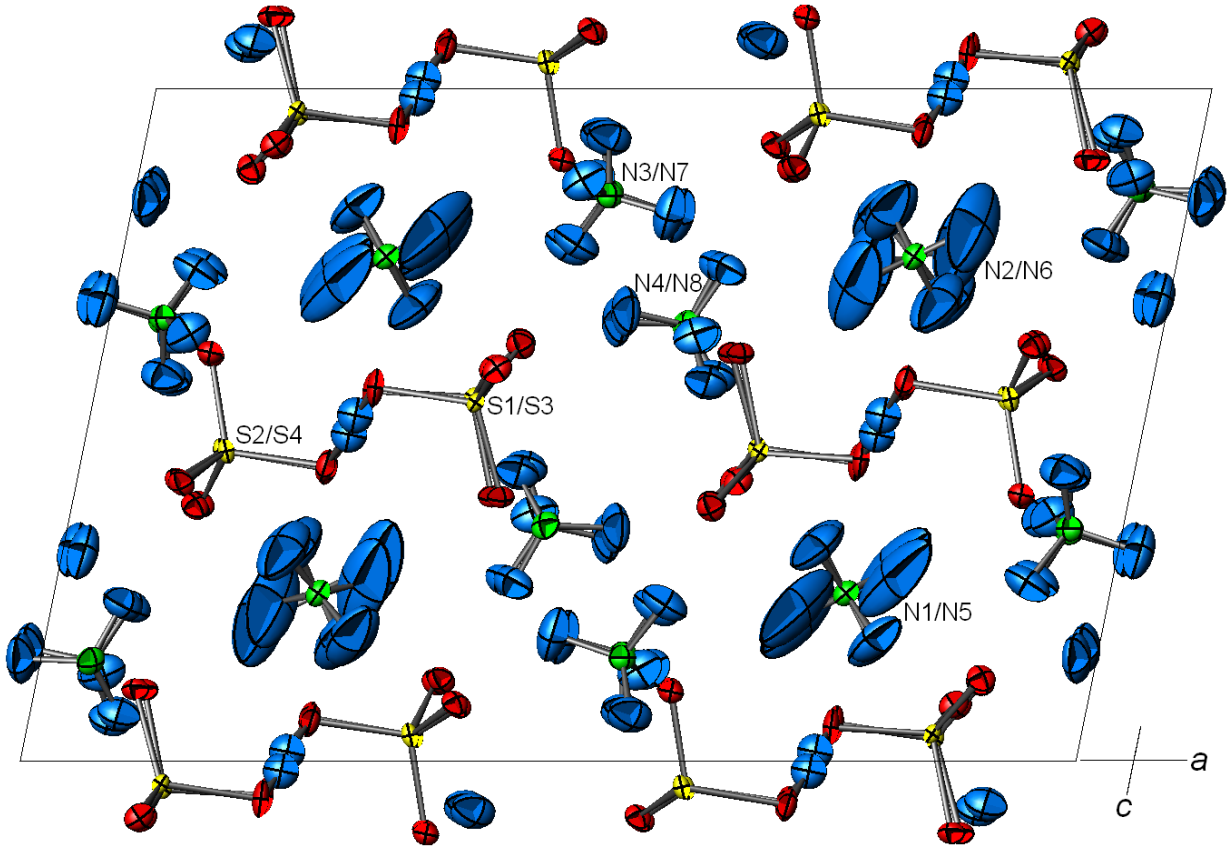

Figure 4.25: Unit cell of monoclinic TAHS-IV ($P2/n$) at 138.5 K. Slight shifts of atomic positions are visible from the overlap of the molecular groups projected along [010]. Displacement ellipsoids are drawn at the 50 % probability level.

[2], the doubling of the unit cell in TAHS-IV interrupts a further development of H-ordering in some way. Therefore, the refined site occupancy of split H-atom positions in a $(SO_4)H(SO_4)$ dimer shows no distinct progress compared to that in TAHS-III, where a clear increase in the degree of order could be evidenced as temperature decreases. The estimated standard deviation of the site occupancy factor in TAHS-IV is fairly large, because the crystal structure refinement itself needed certain restraints. According to the weak intensities of the superstructure reflections, the modification in the crystal structure causing these additional reflections, should be rather small. However, each SO_4 and NH_4 group is linked to each other in the unit cell via either O–H$\cdots$O or N–H$\cdots$O bondings. Thus, a small difference in atom positions or orientations of some groups involves further rearrangements in the unit cell. In this context, the slightly different O–H$\cdots$O bonding between $(SO_4)H(SO_4)$ dimers distorts each SO_4 tetrahedron in the unit cell, leading to unequal N–H$\cdots$O bonds between NH_4 and SO_4 groups and, hence, slightly different orientations of each NH_4 group. The refinement details and results for TAHS-IV are given in Table 4.19–4.20. The two different numbers of refinement parameters given in Table 4.19 refer to the separate refinement processes, once only with the atom positions (150) and once only with ADPs (130), respectively. The bond distances and angles are listed in Table 4.21. Among the different S–O bond lengths in a SO_4 tetrahedron, the one with an asymmetric O–H$\cdots$O bond is the longest and hence the weakest. The same phenomena occur for the N–H bond lengths in a NH_4 tetrahedron and its N–H$\cdots$O bonding, thus, stronger hydrogen bondings with neighbouring SO_4 groups result in longer N–H bonds.

H-splitting in NH_4 groups on a special position

As can be seen in Fig. 4.25, the different NH_4 groups are slightly rotated against each other along the **b** direction in the **a**,**c**-projection. This results from the various N–H$\cdots$O bonding environments due to the reorientations of the SO_4 groups. In this phase IV of TAHS, the NH_4 groups on a special position still show strongly enlarged anisotropic mean-square displacements, whereas those on a general position present relatively small anisotropic mean-square displacements. Therefore, the splitting of some H-atom positions with enlarged anisotropic ADPs took place in a separate refinement process. By performing this kind of refinement, the splitting of H-atom positions were treated with an isotropic mean-square displacement parameter. After the refinement gave a reasonable splitting of those H-atom positions, their site occupancy was refined to evaluate their orientational tendency. As in other splitting cases, the total sum

Table 4.19: Crystal data and refinement details of TAHS-IV with neutron single-crystal diffraction.

Chemical formula	$HO_8S_2{\cdot}3H_4N$
M_r	247.25
Crystal system	Monoclinic
Space group	$P2/n$
Temperature (K)	138.5
a, b, c (Å)	15.538 (8), 11.641 (6), 10.085 (5)
β (°)	101.46 (5)
V (Å^3)	1787.8 (2)
Z	8
D_x (Mg m^{-3})	1.837(2)
Data collection	
No. of measured, independent and observed $[I > 3\sigma(I)]$ reflections	4208, 2689, 1789
R_{int}	0.03
Θ_{max}(°)	37.63
Refinement	
$R[F^2 > 3\sigma(F^2)], wR(F^2)$	0.0832, 0.1657
S	4.02
Extinction method	B-C type I Lorentzian isotropic [37]
Extinction coefficient	1520 (70)
No. of reflections	2689
No. of parameters	150 + 130
$\Delta\rho_{max}, \Delta\rho_{min}$ (fm·Å^{-3})	2.68, -3.60

of the site occupancies was constrained to be one. The final weighted R factor of this refinement yields 0.1506, using 150 atomic coordinates and 147 parameters for the ADPs. An example for such a splitting is shown in Fig. 4.26 with a standard non-splitting description of an ammonium group for comparison. The N–H$\cdots$O bond distances and angles of all NH_4 groups in TAHS-IV are given in Table 4.22 and those using the splitting model are listed in Table 4.23.

Table 4.20: Refinement results of TAHS-IV at 138.5 K. The U-values are given in Å^2.

Atom	x	y	z	Occ.	$U_{11}/Uiso$	U_{22}	U_{33}	U_{12}	U_{13}	U_{23}
S1	0.359 (1)	0.230 (1)	0.459 (2)	1	0.007 (2)	0.010 (1)	0.010 (2)	0 (n.s.)	0 (n.s.)	0 (n.s.)
S2	0.131 (1)	0.011 (2)	0.538 (2)	1	0.008 (2)	0.011 (2)	0.014 (2)	0 (n.s.)	0.004 (1)	0 (n.s.)
S3	0.363 (1)	0.737 (1)	0.467 (2)	1	0.007 (2)	0.010 (1)	0.010 (2)	0 (n.s.)	0 (n.s.)	0 (n.s.)
S4	0.136 (1)	0.518 (2)	0.539 (2)	1	0.008 (2)	0.011 (2)	0.014 (2)	0 (n.s.)	0.004 (1)	0 (n.s.)
N1	0.75	0.0085 (9)	0.75	1	0.0146 (9)	0.0164 (8)	0.0151 (8)	0	0 (n.s.)	0
N2	0.75	0.2441 (7)	0.25	1	0.0130 (9)	0.0171 (8)	0.0167 (8)	0	0 (n.s.)	0
N3	0.4496 (7)	0.261 (1)	0.1539 (8)	1	0.0179 (7)	0.0163 (6)	0.0148 (6)	-0.0021 (4)	0.0029 (5)	0 (n.s.)
N4	0.0497 (6)	0.4876 (6)	0.8522 (9)	1	0.0178 (8)	0.0154 (6)	0.0183 (6)	-0.0046 (5)	0.0015 (5)	-0.0019 (4)
N5	0.75	0.5141 (9)	0.75	1	0.0145 (9)	0.0164 (8)	0.0151 (8)	0	0 (n.s.)	0
N6	0.75	0.7368 (7)	0.25	1	0.0130 (9)	0.0171 (8)	0.0167 (8)	0	0 (n.s.)	0
N7	0.4498 (7)	0.761 (1)	0.1539 (8)	1	0.0179 (7)	0.0163 (6)	0.0148 (6)	-0.0021 (4)	0.0029 (5)	0 (n.s.)
N8	0.0475 (6)	0.9809 (6)	0.8522 (9)	1	0.0178 (8)	0.0154 (6)	0.0183 (6)	-0.0046 (5)	0.0015 (5)	-0.0019 (4)
O1	0.2614 (8)	0.215 (1)	0.449 (1)	1	0.007 (1)	0.031 (1)	0.032 (1)	0 (n.s.)	0.0033 (8)	0 (n.s.)
O2	0.235 (1)	0.033 (1)	0.565 (2)	1	0.009 (1)	0.026 (1)	0.024 (1)	0 (n.s.)	0 (n.s.)	-0.0023 (7)
O3	0.3958 (5)	0.2198 (9)	0.6063 (9)	1	0.018 (1)	0.0165 (8)	0.0111 (8)	0 (n.s.)	0.0024 (7)	0.0019 (6)
O4	0.102 (1)	-0.003 (1)	0.392 (2)	1	0.016 (1)	0.0186 (8)	0.0117 (8)	0 (n.s.)	0.0031 (7)	0 (n.s.)
O5	0.3733 (9)	0.349 (1)	0.415 (2)	1	0.019 (1)	0.0118 (8)	0.0172 (8)	0 (n.s.)	0 (n.s.)	0.0011 (6)
O6	0.1165 (7)	-0.0872 (9)	0.621 (1)	1	0.018 (1)	0.0159 (8)	0.0160 (8)	0.0031 (7)	0.0058 (7)	0.0044 (6)
O7	0.3943 (8)	0.1440 (8)	0.376 (1)	1	0.019 (1)	0.0126 (8)	0.0166 (8)	0 (n.s.)	0.0047 (7)	-0.0048 (6)
O8	0.0957 (7)	0.1164 (7)	0.583 (1)	1	0.017 (1)	0.0127 (8)	0.0146 (8)	0 (n.s.)	0.0049 (7)	-0.0040 (6)
O9	0.2649 (8)	0.715 (1)	0.444 (2)	1	0.007 (1)	0.031 (1)	0.032 (1)	0 (n.s.)	0.0033 (8)	0 (n.s.)
O10	0.234 (1)	0.528 (1)	0.562 (2)	1	0.009 (1)	0.026 (1)	0.024 (1)	0 (n.s.)	0 (n.s.)	-0.0023 (7)

Table 4.20 – continued

Atom	x	y	z	Occ.	$U_{11}/Uiso$	U_{22}	U_{33}	U_{12}	U_{13}	U_{23}
O11	0.4045 (5)	0.7173 (9)	0.6069 (9)	1	0.018 (1)	0.0165 (8)	0.0111 (8)	0 (n.s.)	0.0024 (7)	0.0019 (6)
O12	0.103 (1)	0.494 (1)	0.397 (2)	1	0.016 (1)	0.0186 (8)	0.0117 (8)	0 (n.s.)	0.0031 (7)	0 (n.s.)
O13	0.3769 (8)	0.851 (1)	0.418 (2)	1	0.019 (1)	0.0118 (8)	0.0172 (8)	0 (n.s.)	0 (n.s.)	0.0011 (6)
O14	0.1218 (7)	0.4171 (9)	0.618 (1)	1	0.018 (1)	0.0159 (8)	0.0160 (8)	0.0031 (7)	0.0058 (7)	0.0044 (6)
O15	0.3944 (8)	0.6506 (8)	0.383 (1)	1	0.019 (1)	0.0126 (8)	0.0166 (8)	0 (n.s.)	0.0047 (7)	-0.0048 (6)
O16	0.0997 (7)	0.6235 (7)	0.587 (1)	1	0.0127 (8)	0.0146 (8)	0 (n.s.)	0.0049 (7)	-0.0040 (6)	
H1	0.2489	0.10305	0.5143	0.71 (7)	0.030 (1)					
H2	0.2511	0.14695	0.4857	0.29 (7)	0.030 (1)					
H3	0.709 (1)	0.191 (3)	0.187 (3)	1	0.055 (4)	0.114 (7)	0.083 (5)	0.019 (4)	-0.017 (4)	-0.061 (5)
H4	0.785 (2)	0.056 (2)	0.825 (3)	1	0.049 (3)	0.048 (3)	0.048 (3)	0.008 (2)	-0.019 (2)	-0.018 (2)
H5	0.708 (2)	0.293 (2)	0.265 (4)	1	0.061 (5)	0.122 (9)	0.18 (1)	0.042 (5)	0 (n.s.)	-0.094 (9)
H6	0.794 (2)	-0.040 (4)	0.727 (4)	1	0.092 (6)	0.20 (1)	0.140 (9)	0.114 (8)	-0.062 (7)	-0.12 (1)
H7	0.520 (1)	0.263 (2)	0.189 (2)	1	0.021 (3)	0.049 (3)	0.068 (3)	0 (n.s.)	0 (n.s.)	-0.009 (2)
H8	-0.012 (1)	0.469 (2)	0.831 (2)	1	0.022 (2)	0.055 (3)	0.058 (3)	-0.013 (2)	0.012 (2)	-0.017 (2)
H9	0.431 (1)	0.342 (2)	0.136 (2)	1	0.043 (3)	0.024 (2)	0.038 (2)	0.003 (2)	0 (n.s.)	0 (n.s.)
H10	0.077 (1)	0.437 (2)	0.938 (2)	1	0.044 (3)	0.033 (2)	0.026 (2)	0 (n.s.)	0.010 (2)	0.007 (1)
H11	0.431 (1)	0.211 (2)	0.069 (2)	1	0.046 (3)	0.035 (2)	0.030 (2)	-0.011 (2)	0.008 (2)	-0.008 (2)
H12	0.062 (2)	0.567 (2)	0.868 (3)	1	0.043 (3)	0.018 (2)	0.032 (2)	-0.004 (2)	0 (n.s.)	-0.003 (1)
H13	0.420 (1)	0.227 (2)	0.236 (2)	1	0.053 (3)	0.036 (2)	0.031 (2)	-0.003 (2)	0.023 (2)	0 (n.s.)
H14	0.075 (1)	0.463 (2)	0.769 (2)	1	0.040 (3)	0.034 (2)	0.025 (2)	-0.008 (2)	0.013 (2)	-0.002 (2)
H15	0.2489	0.60305	0.5143	0.73 (7)	0.030 (1)					
H16	0.2511	0.64695	0.4857	0.27 (7)	0.030 (1)					
H17	0.719 (2)	0.687 (3)	0.181 (3)	1	0.055 (4)	0.114 (7)	0.083 (5)	0.019 (4)	-0.017 (4)	-0.061 (5)

Table 4.20 – continued

Atom	x	y	z	Occ.	$U_{11}/Uiso$	U_{22}	U_{33}	U_{12}	U_{13}	U_{23}
H18	0.788 (2)	0.565 (2)	0.818 (3)	1	0.049 (3)	0.048 (3)	0.048 (3)	0.008 (2)	-0.019 (2)	-0.018 (2)
H19	0.700 (2)	0.764 (2)	0.293 (3)	1	0.061 (5)	0.122 (9)	0.18 (1)	0.042 (5)	0 (n.s.)	-0.094 (9)
H20	0.791 (2)	0.476 (4)	0.711 (4)	1	0.092 (6)	0.20 (1)	0.140 (9)	0.114 (8)	-0.062 (7)	-0.12 (1)
H21	0.510 (1)	0.769 (2)	0.185 (2)	1	0.021 (3)	0.049 (3)	0.068 (3)	0 (n.s.)	0 (n.s.)	-0.009 (2)
H22	-0.019 (1)	0.962 (2)	0.847 (2)	1	0.022 (2)	0.055 (3)	0.058 (3)	-0.013 (2)	0.012 (2)	-0.017 (2)
H23	0.423 (1)	0.844 (2)	0.137 (3)	1	0.043 (3)	0.024 (2)	0.038 (2)	0.003 (2)	0 (n.s.)	0 (n.s.)
H24	0.084 (1)	0.940 (2)	0.929 (2)	1	0.044 (3)	0.033 (2)	0.026 (2)	0 (n.s.)	0.010 (2)	0.007 (1)
H25	0.438 (1)	0.710 (2)	0.074 (2)	1	0.046 (3)	0.035 (2)	0.030 (2)	-0.011 (2)	0.008 (2)	-0.008 (2)
H26	0.058 (2)	1.074 (2)	0.867 (3)	1	0.043 (3)	0.018 (2)	0.032 (2)	-0.004 (2)	0 (n.s.)	-0.003 (1)
H27	0.428 (1)	0.721 (2)	0.228 (2)	1	0.053 (3)	0.036 (2)	0.031 (2)	-0.003 (2)	0.023 (2)	0 (n.s.)
H28	0.067 (1)	0.959 (2)	0.765 (2)	1	0.040 (3)	0.034 (2)	0.025 (2)	-0.008 (2)	0.013 (2)	-0.002 (2)

Table 4.21: Bond distances (Å) and angles (°) of TAHS-IV.

S1–O1	1.50 (2)	N7–H27	0.95 (2)	H3–N2–H5'	132 (3)
S1–O3	1.49 (2)	N8–H22	1.05 (2)	H5–N2–H5'	101 (3)
S1–O5	1.48 (2)	N8–H24	1.00 (2)	H7–N3–H9	106 (2)
S1–O7	1.47 (2)	N8–H26	1.11 (2)	H7–N3–H11	113 (2)
S2–O2	1.60 (3)	N8–H28	1.00 (2)	H7–N3–H13	108 (2)
S2–O4	1.46 (3)	O1–S1–O3	104 (1)	H9–N3–H11	111 (2)
S2–O6	1.47 (2)	O1–S1–O5	107 (1)	H9–N3–H13	109 (2)
S2–O8	1.45 (2)	O1–S1–O7	112 (1)	H11–N3–H13	110 (2)
S3–O9	1.51 (2)	O3–S1–O5	108 (1)	H8–N4–H10	106 (2)
S3–O11	1.45 (2)	O3–S1–O7	114 (1)	H8–N4–H12	114 (2)
S3–O13	1.44 (2)	O5–S1–O7	112 (1)	H8–N4–H14	107 (2)
S3–O15	1.46 (2)	O2–S2–O4	107 (2)	H10–N4–H12	112 (2)
S4–O10	1.48 (3)	O2–S2–O6	107 (1)	H10–N4–H14	110 (2)
S4–O12	1.45 (3)	O2–S2–O8	105 (1)	H12–N4–H14	108 (2)
S4–O14	1.45 (2)	O4–S2–O6	116 (1)	H18–N5–H18'	107 (2)
S4–O16	1.47 (2)	O4–S2–O8	110 (1)	H18–N5–H20	103 (3)
N1–H4	1.00 (2)	O6–S2–O8	112 (2)	H18–N5–H20'	111 (3)
N1–H6	0.95 (4)	O9–S3–O11	111 (1)	H20–N5–H20'	122 (4)
N2–H3	1.01 (3)	O9–S3–O13	109 (1)	H17–N6–H17'	105 (3)
N2–H5	0.89 (3)	O9–S3–O15	104 (1)	H17–N6–H19	101 (2)
N3–H7	1.08 (2)	O11–S3–O13	114 (1)	H17–N6–H19'	101 (2)
N3–H9	1.00 (3)	O11–S3–O15	109 (1)	H19–N6–H19'	144 (2)
N3–H11	1.03 (3)	O13–S3–O15	110 (1)	H21–N7–H23	108 (2)
N3–H13	1.10 (2)	O10–S4–O12	108 (2)	H21–N7–H25	107 (2)
N4–H8	0.97 (2)	O10–S4–O14	104 (1)	H21–N7–H27	110 (2)
N4–H10	1.06 (2)	O10–S4–O16	109 (1)	H23–N7–H25	110 (2)
N4–H12	0.95 (2)	O12–S4–O14	109 (1)	H23–N7–H27	114 (2)
N4–H14	1.03 (2)	O12–S4–O16	114 (2)	H25–N7–H27	108 (2)
N5–H18	1.01 (2)	O14–S4–O16	113 (2)	H22–N8–H24	109 (2)
N5–H20	0.93 (4)	H4–N1–H4'	114 (2)	H22–N8–H26	110 (2)
N6–H17	0.96 (3)	H4–N1–H6	101 (3)	H22–N8–H28	112 (2)
N6–H19	1.01 (3)	H4–N1–H6'	117 (3)	H24–N8–H26	108 (2)
N7–H21	0.92 (2)	H6–N1–H6'	107 (4)	H24–N8–H28	109 (2)
N7–H23	1.06 (3)	H3–N2–H3'	105 (3)	H26–N8–H28	109 (2)
N7–H25	1.03 (3)	H3–N2–H5	96 (2)		

Table 4.22: N–H···O bond distances (Å) and angles(°) of NH_4 groups in TAHS-IV.

N–H··· O	N–H	H···O	N–O	angle
N1–H4···O13	1.00 (2)	1.89 (3)	2.849 (15)	159 (3)
N1–H6···O7	0.95 (4)	2.28 (4)	2.944 (12)	126 (3)
N1–H6···O4	0.95 (4)	2.26 (5)	2.949 (19)	129 (3)
N2–H3···O6	1.01 (3)	1.90 (3)	2.873 (12)	161 (3)
N2–H5···O11	0.89 (3)	2.38 (3)	3.070 (9)	134 (3)
N2–H5···O16	0.89 (3)	2.41 (3)	3.002 (11)	124 (3)
N3–H7···O11	1.08 (2)	2.17 (2)	2.975 (12)	130 (2)
N3–H7···O16	1.08 (2)	2.21 (2)	2.888 (16)	119 (2)
N3–H9···O12	1.00 (3)	1.86 (3)	2.853 (19)	180 (2)
N3–H11···O8	1.03 (3)	1.86 (3)	2.888 (14)	177 (2)
N3–H13···O7	1.10 (2)	1.82 (2)	2.897 (15)	165 (2)
N4–H8···O15	0.97 (2)	2.15 (2)	2.967 (14)	141 (2)
N4–H10···O5	1.06 (2)	1.84 (2)	2.904 (17)	179 (2)
N4–H12···O11	0.95 (2)	1.83 (2)	2.777 (12)	174 (3)
N4–H14···O14	1.03 (2)	1.90 (2)	2.928 (15)	179 (2)
N5–H18···O5	1.01 (2)	1.79 (3)	2.783 (15)	166 (3)
N5–H20···O15	0.93 (4)	2.57 (4)	3.050 (12)	112 (3)
N5–H20···O12	0.93 (4)	2.17 (4)	2.955 (19)	142 (4)
N6–H17···O14	0.96 (3)	1.94 (3)	2.812 (12)	149 (3)
N6–H19···O3	1.01 (3)	1.97 (3)	2.964 (9)	167 (2)
N6–H19···O8	1.01 (3)	2.78 (3)	3.148 (11)	102 (2)
N7–H21···O3	0.92 (2)	2.32 (2)	3.023 (12)	133 (2)
N7–H21···O8	0.92 (2)	2.28 (2)	2.914 (16)	126 (2)
N7–H23···O4	1.06 (3)	1.84 (3)	2.889 (19)	169 (2)
N7–H25···O16	1.03 (3)	1.90 (3)	2.922 (13)	172 (2)
N7–H27···O15	0.95 (2)	1.92 (2)	2.866 (15)	173 (2)
N8–H22···O7	1.05 (2)	1.89 (2)	2.844 (15)	149 (2)
N8–H24···O13	1.00 (2)	1.86 (2)	2.834 (17)	164 (2)
N8–H26···O3	1.11 (2)	1.84 (2)	2.924 (12)	166 (2)
N8–H28···O6	1.00 (2)	1.85 (2)	2.849 (15)	173 (2)

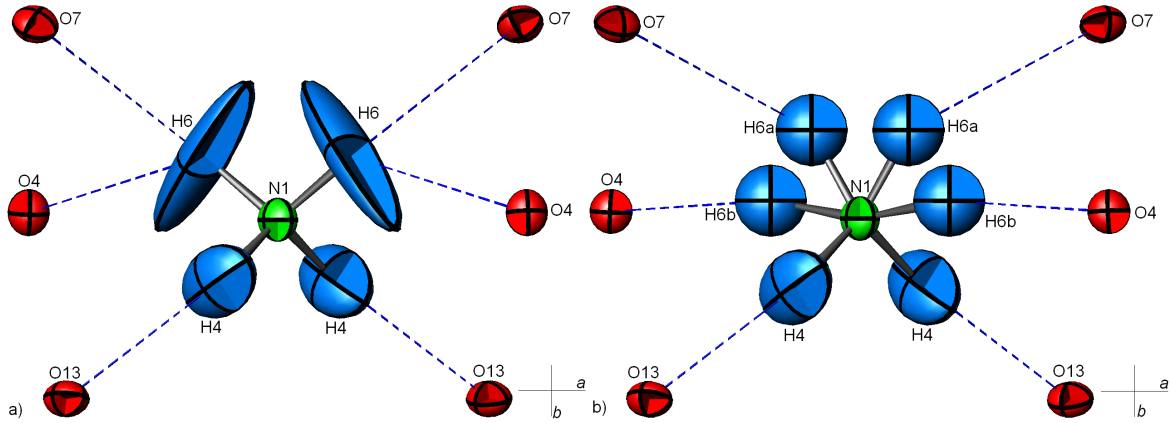

Figure 4.26: NH_4 group on a special position with its neighbouring O atoms. a) Non-splitting b) splitting model with isotropic mean-square displacement parameters. The difference in the site occupancy is not displayed here. Displacement ellipsoids are drawn at the 50 % probability level.

Table 4.23: N–H···O bond distances (Å) and angles(°) of NH_4 groups on a special position after splitting in TAHS-IV.

N–H··· O	N–H	H···O	N–O	angle
N1–H4···O13	1.06 (3)	1.79 (3)	2.818 (10)	162 (3)
N1–H6a···O7	0.94 (1)	2.27 (1)	2.961 (12)	129.8 (8)
N1–H6b···O4	1.08 (1)	1.90 (2)	2.963 (18)	168 (1)
N2–H3···O6	1.03 (3)	1.87 (3)	2.851 (11)	157 (2)
N2–H5a···O11	1.03 (1)	2.03 (2)	3.056 (12)	175.4 (9)
N2–H5b···O16	0.95 (2)	2.26 (2)	3.041 (11)	139 (1)
N5–H18···O5	0.95 (3)	1.89 (3)	2.816 (10)	164 (3)
N5–H20a···O15	1.00 (1)	2.29 (1)	3.033 (12)	130.7 (8)
N5–H20b···O12	1.09 (1)	1.88 (2)	2.945 (19)	164 (1)
N6–H17···O14	0.93 (3)	1.97 (3)	2.833 (11)	153 (3)
N6–H19a···O3	1.04 (1)	1.95 (2)	2.982 (12)	172.1 (9)
N6–H19b···O8	1.02 (2)	2.27 (2)	3.112 (11)	140 (1)

There are basically no distinct changes in the N–H···O bond distances between the phases III and IV of TAHS. However, one of the NH_4 groups on a general position loses its bifurcated connection to its surrounding neighbours and reorientates in favour of a shorter hydrogen bond. Even though there are still two O atoms around H8 and H22, their displacement ellipsoids are directed perpendicular to the shorter hydrogen bond in TAHS-IV, whereas they were positioned more or less in the middle of two possible hydrogen bonds in phase III. It is also interesting to note that, with the splitting of H-atom positions which show strongly enlarged displacement ellipsoids, distinctly shorter hydrogen bonds are formed. As can be seen in Table 4.23, the shorter bonds have an angle of nearly 180° whereas the longer ones have smaller angles. The site occupancy ratios for H6a:H6b and H5a:H5b yield 47 (1) %: 53 (1) % and 60 (1) %: 40 (1) %, respectively. In each case, the shorter hydrogen bond shows a higher occupancy. Although the H atoms around the NH_4 groups on a special position still show large ADPs compared to those on a general position, the tendency of forming a shorter hydrogen bond and, hence, a reorientation of these groups can be observed. Owing to the large number of NH_4 groups and predetermined restraints, no rigid-body analysis was performed for phase IV of TAHS.

4.5 Low-temperature phase V

The crystal structure of TAHS-V is triclinic with space group symmetry $P\bar{1}$ and the lattice parameters obtained from X-ray powder diffraction are $a = 8.282\,(4)$, $b = 10.095\,(5)$, $c = 11.613\,(6)$ Å, $\alpha = 90.44\,(5)$, $\beta = 110.07\,(6)$ and $\gamma = 100.64\,(5)°$. The IV/V-phase transition of TAHS has first-order character, showing a clear hysteresis in X-ray powder- as well as single-crystal neutron diffraction (see chapter 5). As mentioned above, a twinning of the sample crystal was observed during single-crystal neutron diffraction experiments below the IV/V-phase transition (Fig. 4.27). For verification, a Q-scan technique was applied and the $0kl$ plane of reciprocal space was mapped. Fig. 4.28 shows a 4×-splitting of the 040-reflection in the $0kl$ plane, which is typical for the twinning resulting from a monoclinic to triclinic phase transition. The twinning effect at the IV/V-phase transition was reproducible. Since a separate measurement of these split reflections was not possible in phase V, no further single-crystal neutron diffraction was performed below the IV/V-phase transition of TAHS. However, no distinct evidence of a twinning was detected during single-crystal X-ray diffraction measurements on a STOE-IPDS II. However, some limitations of peak resolution existed on the STOE-

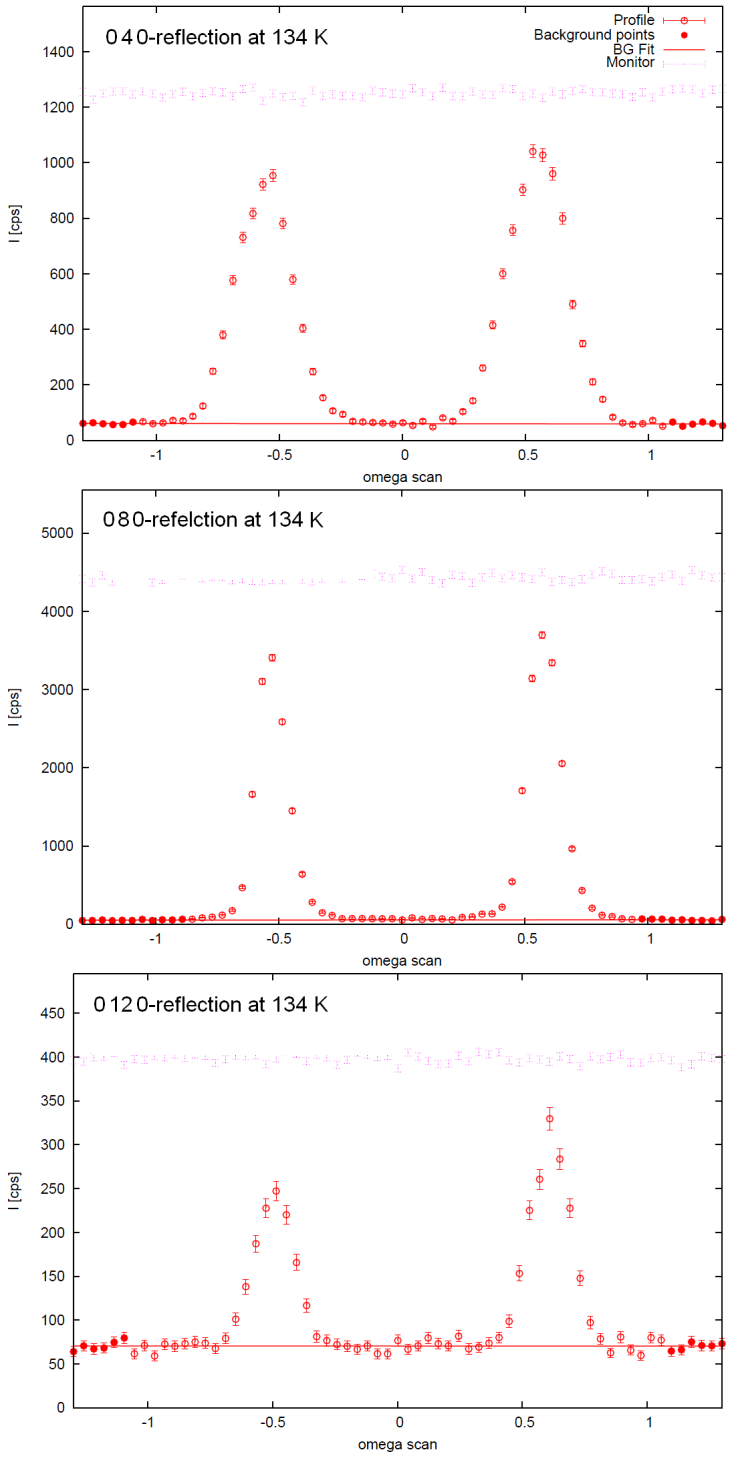

Figure 4.27: Splitting of $0k0$-reflections recorded by ω scans at 134 K. The angular distance between two split reflection positions remains constant with increasing k-values.

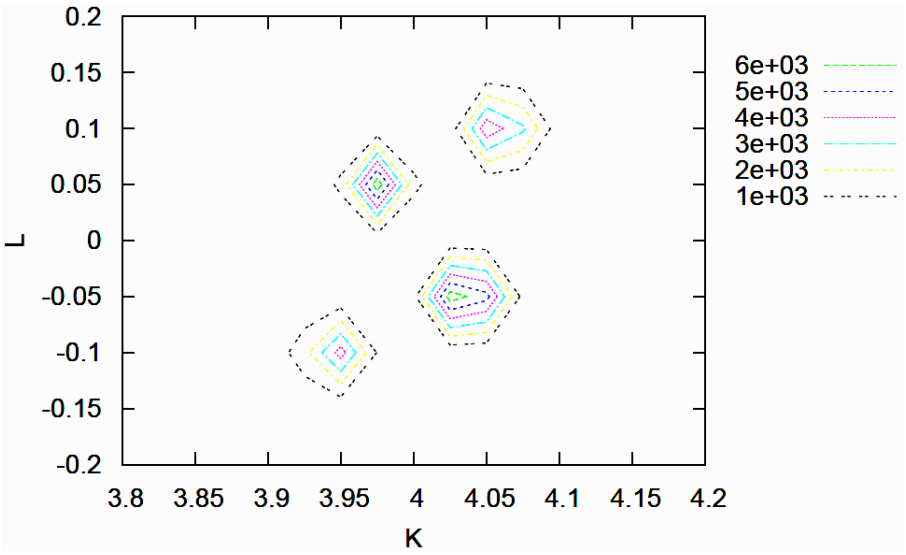

Figure 4.28: Q-scan measurements for the reciprocal $0kl$ plane.

IPDS II diffractometer. The data collection for phase V of TAHS was performed at 126 K with the same crystal that was used for the successive temperature-dependent measurements (from phase II to IV). Although this sample passed through several phase transitions, the room-temperature measurements at the end of the experiments showed no significant changes of the sample quality. It is known that TAHS is ferroelastic at room temperature [42], and, hence, the relatively small size of the sample crystal ($\sim 0.3 \times 0.3 \times 0.1$ mm^3) in contrast to the one used for neutron diffraction ($\sim 3 \times 3 \times 3\times$ mm^3) seemed to have survived the first-order IV/V-phase transition. The crystal structure of TAHS-V from the X-ray single crystal dataset is best described with a triclinic unit cell (coverage after integration: 99.6 %) with lattice parameters $a = 8.2785\,(7), b = 10.0895\,(8), c = 11.5914\,(10)$ Å, $\alpha = 90.444\,(7), \beta = 110.056\,(6)$ and $\gamma = 100.646\,(7)°$, which is in good agreement with the values obtained by X-ray powder diffraction studies, as well as with those from literature [8]. The reflections of TAHS-V in reciprocal space are shown in Fig. 4.29. After an absorption correction was applied to the measured X-ray data, the crystal structure of TAHS-V was solved and refined using SIR2002 [43] and SHELXL97 [32]. Using a difference Fourier synthesis, all H atoms were found in TAHS-V. All atoms (except hydrogen) in the unit cell were refined anisotropically. Fig. 4.30 shows the triclinic unit cell of TAHS-V. The angle γ in TAHS-V corresponds to the monoclinic angle β in phase IV and the unit cell has been halved in the **a** direction (see Fig. 4.31). The twofold axis which existed in phases II, III and IV disappears in phase V, and the N1 and N2 atoms are now located on general

Figure 4.29: Reflections of TAHS-V at 126 K using an image-plate diffractometer (STOE-IPDS II). a) $hk0$ b) $h0l$ c) $0kl$.

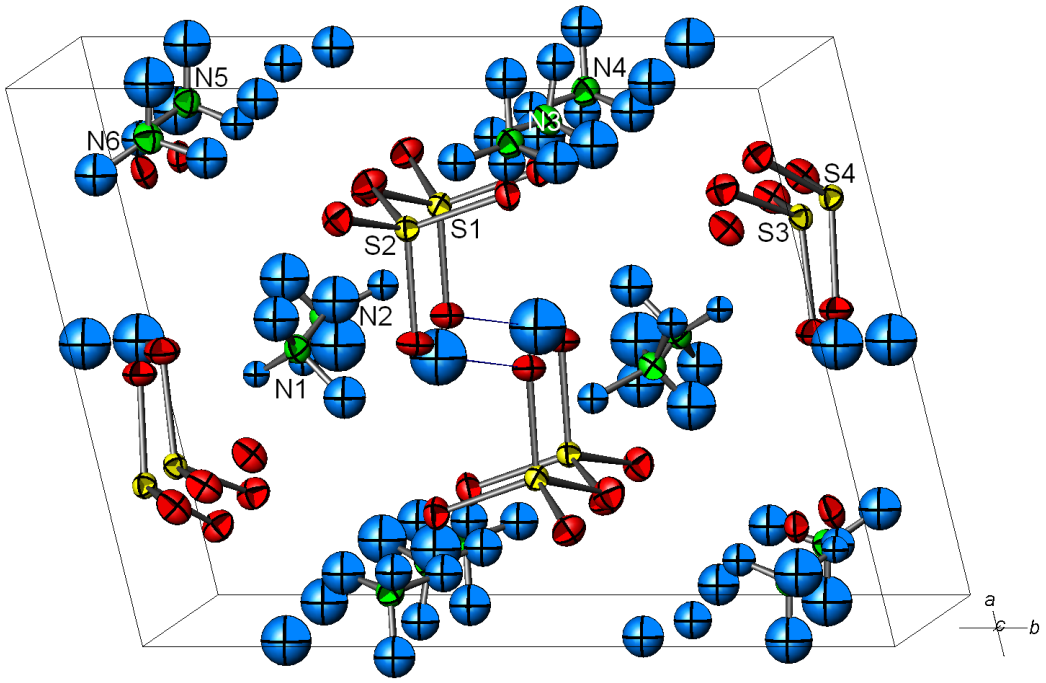

Figure 4.30: Triclinic unit cell ($P\bar{1}$) of TAHS-V. Displacement ellipsoids are drawn at the 50 % probability level.

positions. While the H atoms of $N1H_4$ and $N2H_4$ showed larger mean-square displacement parameters in the other phases, these are now considerably smaller. Hence, these ammonium groups seem to be ordered in phase V. The hydrogen in the asymmetric O–H···O bond was found using a difference Fourier synthesis, and refined isotropically. There was no indication for H-disorder, however, the precision of the H distribution is limited in the case of X-ray diffraction. The asymmetric O–H···O bond distances are given in Table 4.24. No significant changes took place in the O–O bond distances of

Table 4.24: O–H···O bond distances (Å) and angles (°) in the $(SO_4)H(SO_4)$ dimers in TAHS-V.

O–H···O	D–H	H···A	D···A	<DHA
O2–H1···O1	0.86 (6)	1.72 (6)	2.538 (4)	157 (4)
O10–H2···O9	0.96 (5)	1.57 (5)	2.515 (3)	170 (4)

the $(SO_4)H(SO_4)$ dimer from room-temperature phase II to low-temperature phase V. The only remarkable difference is the asymmetric O–H···O bond in low-temperature phases, in contrast to the room-temperature phase II, in which an inversion centre is present in the middle of the $(SO_4)H(SO_4)$ dimer. Hence, a symmetric hydrogen bond is formed in that phase. By refining site occupancy factors for the split-atom positions

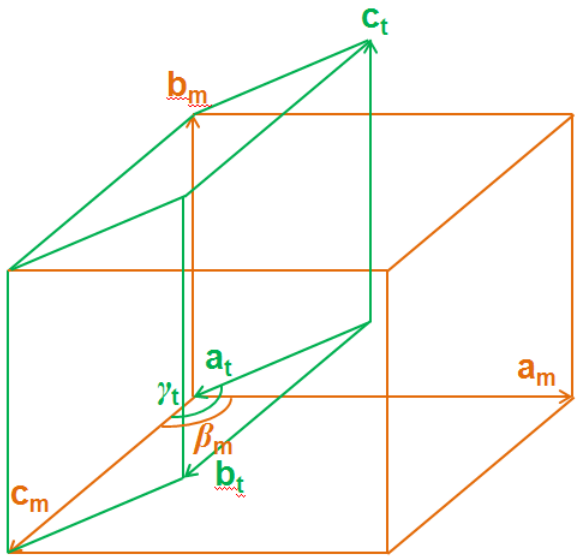

Figure 4.31: Geometrical relation between the monoclinic (TAHS-IV) and the triclinic unit cells (TAHS-V).

in other low-temperature phases (III and IV), the H-ordering in the O–H···O bonds increases with decreasing temperature. It seems that there also is a slight difference between two symmetrically independent O–H···O bonds in TAHS-V (see Table 4.24). However, the precision of the results for phase V is limited, since the data were collected by X-ray diffraction.

Fig. 4.32 shows the mean-square displacements of H atoms along the principal axes in the $(SO_4)H(SO_4)$ hydrogen bond as a function of temperature in the phases I-III. The first principal axis of the thermal ellipsoid of H atoms is directed parallel to the O–H–O hydrogen bonds and thus, its mean-square displacement is the largest. The other two mean-square displacements along their principal axes are similar and were therefore plotted as averaged (U2/U3). The development of the curve, especially of U1, suggests a dynamical H-disorder, which increases with rising temperature. The program JANA2006 [36] provides a potential curve map between two selected maxima from a section of j.p.d.f. (joined probability density function) map. Fig 4.33 illustrates the development of potential curves between O–H–O hydrogen bonds at various temperatures. From the high-temperature phase I to the low-temperature phase IV the H-disorder was described using a split-atom model (neutron diffraction data) and phase V refers to the X-ray diffraction data with a single isotropic H atom in the asymmetric O–H···O hydrogen bond. In high-temperature phase I, the potential barriers between the two split H-atom positions are comparably low. Though the potential barriers be-

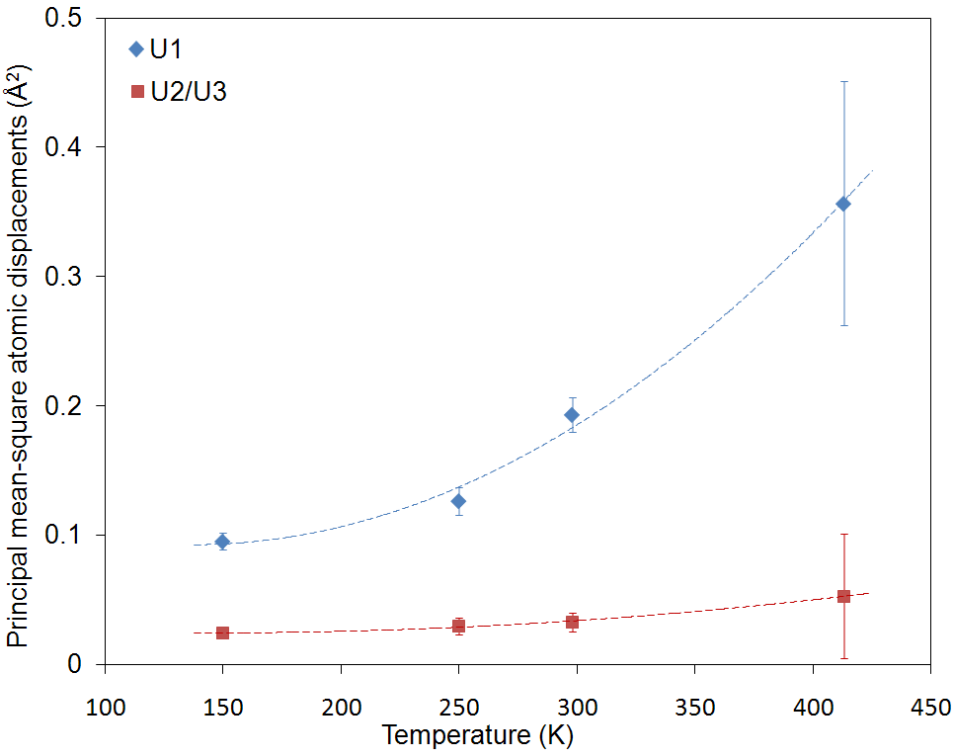

Figure 4.32: Mean-square displacements of H atoms along the principal axes in the $(SO_4)H(SO_4)$ hydrogen bond as a function of temperature. U2/U3 shows the averaged mean-square displacements along the second and third principal axes.

tween these two split H-atom positions are similarly low in room-temperature phase II, the barrier between O and H in the O–H–O hydrogen bonds has become higher. From phase III to phase IV the degree of the H-ordering increases, and in phase V an ordered O–H···O distribution is formed. The refinement details and results for TAHS-V are given in Tables 4.25–4.26. The bond distances and angles are listed in Table 4.27. There is a general tendency that the N–H bond lengths in the case of X-ray diffraction are shorter than in the case of neutron diffraction, since the single electrons of the H atoms are shifted from the proton position to the bonding partner, nitrogen. Moreover, the precise localization of hydrogen (single electron) is difficult with X-ray diffraction. The N–H···O bond distances and angles are given in Table 4.28. In the triclinic space group, all ammonium groups are now on general positions. It is noticeable that there is no longer a bifurcated hydrogen bonding in $N1H_4$ and $N2H_4$ groups which were located on special positions (2) in the monoclinic phases. Thus, it seems that these ammonium groups also become ordered in the triclinic phase V. No further rigid-body analysis was carried out for this phase, because all H atoms were described isotropically.

Table 4.25: Crystal data and refinement details of TAHS-V with X-ray single-crystal diffraction.

Chemical formula	$HO_8S_2{\cdot}3H_4N$
M_r	247.25
Crystal system	Triclinic
Space group	$P\bar{1}$
Temperature (K)	126
a, b, c (Å)	8.282 (4), 10.095 (5), 11.613 (6)
α, β, γ (°)	90.44 (5), 110.07 (6), 100.64 (5)
V (Å^3)	893.6 (8)
Z	4
D_x (Mg m^{-3})	1.838(2)
Data collection	
μ (mm^{-1})	0.623
Absorption correction	numerical
T_{min}, T_{max}	0.797, 0.942
No. of measured, independent and observed $[I > 2\sigma(I)]$ reflections	21478, 6139, 3270
R_{int}	0.0567
Θ_{max}(°)	32.05
Refinement	
$R[F^2 > 2\sigma(F^2)], wR(F^2), S$	0.0390, 0.1172, 0.942
No. of reflections	6139
No. of parameters	326
$\Delta\rho_{max}, \Delta\rho_{min}$ (e Å^{-3})	0.500, -0.654

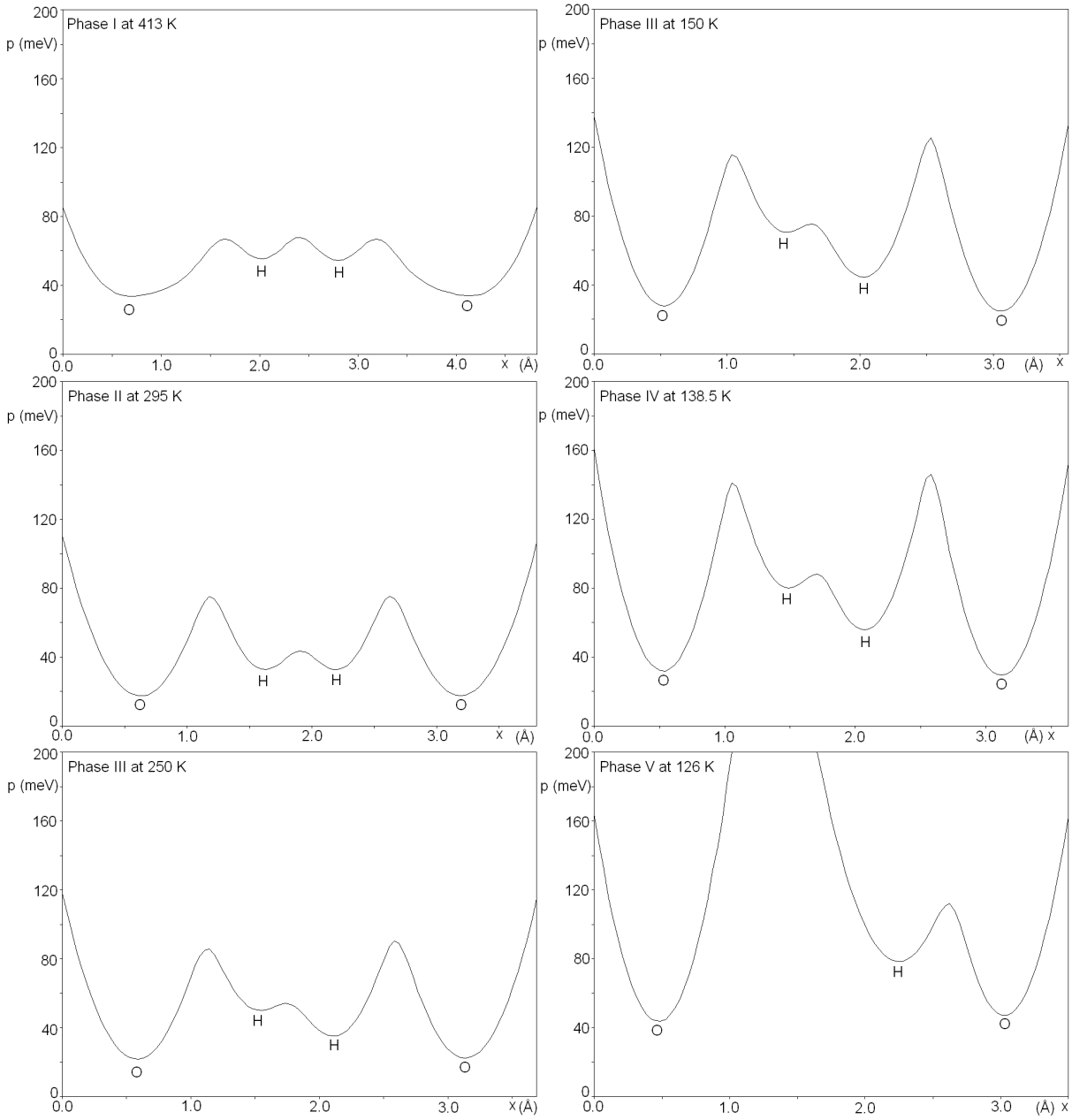

Figure 4.33: Potential curves of the O–H–O hydrogen bonds at various temperatures.

Table 4.26: Refinement results of TAHS-V at 126 K. The U-values are given in Å^2.

Atom	x	y	z	Occ.	$U_{11}/Uiso$	U_{22}	U_{33}	U_{12}	U_{13}	U_{23}
S1	0.2743 (1)	-0.4566 (1)	0.3012 (1)	1	0.0132 (3)	0.0123 (3)	0.0135 (3)	0.0036 (2)	0.0041 (2)	0.0011 (2)
S2	0.7302 (1)	-0.5351 (1)	0.1960 (1)	1	0.0135 (3)	0.0117 (3)	0.0132 (3)	0.0025 (2)	0.0041 (2)	0.0011 (2)
S3	0.2804 (1)	0.0451 (1)	0.0878 (1)	1	0.0137 (3)	0.0119 (3)	0.0149 (3)	0.0030 (2)	0.0064 (2)	0.0020 (2)
S4	0.7306 (1)	-0.0343 (1)	0.4198 (1)	1	0.0138 (3)	0.0114 (3)	0.0140 (3)	0.0017 (2)	0.0064 (2)	0 (n.s.)
N1	0.5028 (3)	-0.2577 (3)	0.6124 (2)	1	0.017 (1)	0.014 (1)	0.020 (1)	0.002 (1)	0.008 (1)	0.003 (1)
N2	0.5078 (3)	-0.7555 (3)	-0.1168 (2)	1	0.015 (1)	0.015 (1)	0.018 (1)	0.002 (1)	0.004 (1)	0 (n.s.)
N3	0.1012 (3)	-0.6529 (3)	0.5127 (2)	1	0.018 (1)	0.016 (1)	0.016 (1)	0 (n.s.)	0.005 (1)	0 (n.s.)
N4	0.0963 (3)	0.3453 (3)	0.0141 (2)	1	0.018 (1)	0.016 (1)	0.016 (1)	0.004 (1)	0.004 (1)	0.002 (1)
N5	0.0918 (4)	-0.1523 (3)	0.2823 (3)	1	0.018 (1)	0.015 (1)	0.019 (1)	0.004 (1)	0.008 (1)	0 (n.s.)
N6	0.1081 (4)	-0.1497 (3)	-0.2045 (2)	1	0.019 (1)	0.017 (1)	0.020 (1)	0.002 (1)	0.010 (1)	0.003 (1)
O1	0.4686 (3)	-0.4342 (2)	0.3295 (2)	1	0.013 (1)	0.022 (1)	0.024 (1)	0.003 (1)	0.004 (1)	0 (n.s.)
O2	0.5280 (3)	-0.5579 (2)	0.1617 (2)	1	0.012 (1)	0.027 (1)	0.023 (1)	0.002 (1)	0.005 (1)	0.002 (1)
O3	0.2100 (3)	-0.6019 (2)	0.3077 (2)	1	0.021 (1)	0.013 (1)	0.021 (1)	0.004 (1)	0.009 (1)	0.003 (1)
O4	0.7926 (3)	-0.3904 (2)	0.1958 (2)	1	0.022 (1)	0.012 (1)	0.023 (1)	0.002 (1)	0.009 (1)	0 (n.s.)
O5	0.2384 (3)	-0.3761 (2)	0.3921 (2)	1	0.021 (1)	0.022 (1)	0.017 (1)	0.006 (1)	0.006 (1)	-0.003 (1)
O6	0.7568 (3)	-0.6131 (2)	0.1010 (2)	1	0.023 (1)	0.020 (1)	0.017 (1)	0.005 (1)	0.008 (1)	-0.003 (1)
O7	0.1918 (3)	-0.4163 (2)	0.1765 (2)	1	0.020 (1)	0.023 (1)	0.015 (1)	0.007 (1)	0.004 (1)	0.005 (1)
O8	0.8000 (3)	-0.5844 (2)	0.3179 (2)	1	0.019 (1)	0.025 (1)	0.015 (1)	0.007 (1)	0.005 (1)	0.005 (1)
O9	0.4743 (3)	0.0669 (2)	0.1585 (2)	1	0.013 (1)	0.022 (1)	0.027 (1)	0.003 (1)	0.005 (1)	0.004 (1)
O10	0.5304 (3)	-0.0470 (2)	0.3564 (2)	1	0.014 (1)	0.026 (1)	0.024 (1)	0.003 (1)	0.007 (1)	0 (n.s.)
O11	0.2076 (3)	-0.1010 (2)	0.0800 (2)	1	0.020 (1)	0.012 (1)	0.021 (1)	0.003 (1)	0.008 (1)	0.002 (1)
O12	0.8113 (3)	0.1075 (2)	0.4236 (2)	1	0.023 (1)	0.012 (1)	0.019 (1)	0 (n.s.)	0.006 (1)	0.002 (1)
O13	0.2532 (3)	0.0915 (2)	-0.0359 (2)	1	0.024 (1)	0.021 (1)	0.015 (1)	0 (n.s.)	0.009 (1)	0.004 (1)

Table 4.26 – continued

Atom	x	y	z	Occ.	$U_{11}/Uiso$	U_{22}	U_{33}	U_{12}	U_{13}	U_{23}
O14	0.7866 (3)	-0.1204 (2)	0.3456 (2)	1	0.020 (1)	0.023 (1)	0.017 (1)	0.007 (1)	0.007 (1)	-0.002 (1)
O15	0.2013 (3)	0.1215 (2)	0.1543 (2)	1	0.021 (1)	0.022 (1)	0.017 (1)	0.007 (1)	0.009 (1)	0 (n.s.)
O16	0.7558 (3)	-0.0803 (2)	0.5418 (2)	1	0.022 (1)	0.024 (1)	0.015 (1)	0 (n.s.)	0.009 (1)	0.002 (1)
H1	0.499 (7)	-0.538 (5)	0.220 (5)	1	0.06 (2)					
H2	0.517 (6)	-0.011 (4)	0.280 (4)	1	0.05 (1)					
H3	0.549 (4)	-0.193 (3)	0.596 (3)	1	0.013 (8)					
H4	0.421 (6)	-0.317 (4)	0.545 (4)	1	0.04 (1)					
H5	0.587 (5)	-0.308 (4)	0.642 (4)	1	0.03 (1)					
H6	0.443 (6)	-0.246 (4)	0.672 (4)	1	0.04 (1)					
H7	0.428 (5)	-0.800 (3)	-0.087 (3)	1	0.018 (8)					
H8	0.561 (4)	-0.672 (3)	-0.069 (3)	1	0.018 (8)					
H9	0.467 (7)	-0.737 (5)	-0.188 (5)	1	0.06 (1)					
H10	0.579 (7)	-0.794 (5)	-0.121 (4)	1	0.05 (1)					
H11	0.134 (6)	-0.631 (5)	0.453 (5)	1	0.05 (1)					
H12	0.141 (6)	-0.712 (5)	0.562 (4)	1	0.05 (1)					
H13	0.126 (5)	-0.581 (4)	0.558 (4)	1	0.03 (1)					
H14	0 (n.s.)	-0.680 (4)	0.487 (3)	1	0.03 (1)					
H15	0.137 (5)	0.363 (4)	-0.040 (4)	1	0.03 (1)					
H16	0.127 (5)	0.284 (4)	0.059 (4)	1	0.04 (1)					
H17	-0.016 (6)	0.334 (4)	-0.026 (4)	1	0.03 (1)					
H18	0.126 (5)	0.417 (4)	0.063 (4)	1	0.03 (1)					
H19	0.112 (6)	-0.130 (5)	0.222 (5)	1	0.05 (1)					
H20	0.143 (4)	-0.087 (3)	0.332 (3)	1	0.014 (8)					

Table 4.26 – continued

Atom	x	y	z	Occ.	$U_{11}/Uiso$	U_{22}	U_{33}	U_{12}	U_{13}	U_{23}
H21	-0.012 (7)	-0.170 (4)	0.264 (4)	1	0.04 (1)					
H22	0.127 (5)	-0.216 (4)	0.313 (3)	1	0.021 (9)					
H23	0.141 (6)	-0.224 (4)	-0.173 (4)	1	0.03 (1)					
H24	0.116 (5)	-0.128 (4)	0.273 (4)	1	0.022 (9)					
H25	0.009 (7)	-0.167 (5)	-0.218 (4)	1	0.05 (1)					
H26	0.170 (5)	-0.073 (4)	-0.163 (4)	1	0.04 (1)					

Table 4.27: Bond distances (Å) and angles (°) in TAHS-V.

S1–O1	1.500 (2)	N5–H21	0.80 (5)	H4–N1–H6	107 (4)
S1–O3	1.477 (2)	N5–H22	0.79 (4)	H5–N1–H6	111 (4)
S1–O5	1.468 (2)	N6–H23	0.89 (4)	H7–N2–H8	108 (3)
S1–O7	1.471 (2)	N6–H24	0.84 (4)	H7–N2–H9	114 (4)
S2–O2	1.554 (2)	N6–H25	0.76 (5)	H7–N2–H10	117 (4)
S2–O4	1.457 (2)	N6–H26	0.88 (4)	H8–N2–H9	106 (4)
S2–O6	1.450 (2)	O1–S1–O3	108.0 (1)	H8–N2–H10	110 (4)
S2–O8	1.464 (2)	O1–S1–O5	109.4 (1)	H9–N2–H10	101 (5)
S3–O9	1.505 (2)	O1–S1–O7	108.5 (1)	H11–N3–H12	124 (5)
S3–O11	1.477 (2)	O3–S1–O5	110.0 (1)	H11–N3–H13	105 (4)
S3–O13	1.469 (2)	O3–S1–O7	110.3 (1)	H11–N3–H14	109 (4)
S3–O15	1.464 (2)	O5–S1–O7	110.7 (1)	H12–N3–H13	105 (4)
S4–O10	1.546 (2)	O2–S2–O4	106.8 (1)	H12–N3–H14	104 (4)
S4–O12	1.457 (2)	O2–S2–O6	105.2 (1)	H13–N3–H14	110 (4)
S4–O14	1.458 (2)	O2–S2–O8	106.7 (1)	H15–N4–H16	119 (4)
S4–O16	1.452 (2)	O4–S2–O6	112.5 (1)	H15–N4–H17	102 (4)
N1–H3	0.76 (3)	O4–S2–O8	112.2 (1)	H15–N4–H18	108 (4)
N1–H4	0.95 (4)	O6–S2–O8	112.8 (1)	H16–N4–H17	115 (4)
N1–H5	0.91 (4)	O9–S3–O11	107.7 (1)	H16–N4–H18	105 (4)
N1–H6	1.00 (5)	O9–S3–O13	108.8 (1)	H17–N4–H18	107 (4)
N2–H7	0.90 (4)	O9–S3–O15	108.5 (1)	H19–N5–H20	104 (4)
N2–H8	0.95 (3)	O11–S3–O13	110.3 (1)	H19–N5–H21	107 (5)
N2–H9	0.81 (5)	O11–S3–O15	110.5 (1)	H19–N5–H22	118 (5)
N2–H10	0.78 (5)	O13–S3–O15	110.9 (1)	H20–N5–H21	116 (4)
N3–H11	0.84 (5)	O10–S4–O12	107.2 (1)	H20–N5–H22	106 (3)
N3–H12	0.86 (5)	O10–S4–O14	107.0 (1)	H21–N5–H22	107 (4)
N3–H13	0.84 (4)	O10–S4–O16	105.8 (1)	H23–N6–H24	120 (4)
N3–H14	0.78 (1)	O12–S4–O14	111.7 (1)	H23–N6–H25	101 (4)
N4–H15	0.82 (4)	O12–S4–O16	112.3 (1)	H23–N6–H26	116 (4)
N4–H16	0.83 (4)	O14–S4–O16	112.4 (1)	H24–N6–H25	104 (4)
N4–H17	0.87 (4)	H3–N1–H4	116 (4)	H24–N6–H26	96 (3)
N4–H18	0.86 (4)	H3–N1–H5	105 (4)	H25–N6–H26	119 (5)
N5–H19	0.80 (5)	H3–N1–H6	115 (4)		
N5–H20	0.82 (3)	H4–N1–H5	101 (4)		

Table 4.28: N–H···O bond distances (Å) and angles(°) in NH_4 groups of TAHS-V.

N–H··· O	N–H	H···O	N–O	angle
N1–H3···O16	0.76 (3)	2.15 (3)	2.843 (4)	152 (5)
N1–H4···O5	0.95 (4)	1.90 (4)	2.813 (4)	160 (5)
N1–H5···O3	0.91 (4)	1.98 (4)	2.877 (4)	171 (5)
N1–H6···O8	1.00 (5)	2.42 (5)	3.069 (4)	122 (5)
N2–H7···O13	0.90 (4)	1.91 (4)	2.810 (4)	174 (5)
N2–H8···O6	0.95 (3)	2.07 (3)	2.827 (4)	135 (5)
N2–H9···O14	0.81 (5)	2.46 (5)	2.991 (4)	124 (5)
N2–H10···O11	0.78 (5)	2.14 (5)	2.901 (4)	165 (5)
N3–H11···O3	0.84 (5)	2.00 (5)	2.840 (4)	173 (5)
N3–H12···O14	0.86 (5)	2.08 (5)	2.933 (4)	170 (5)
N3–H13···O8	0.84 (4)	2.05 (4)	2.894 (4)	174 (5)
N3–H14···O12	0.78 (5)	2.36 (5)	2.966 (4)	136 (5)
N3–H14···O8’	0.78 (5)	2.43 (5)	2.934 (4)	123 (5)
N4–H15···O4	0.82 (4)	2.08 (4)	2.897 (4)	172 (5)
N4–H16···O15	0.83 (4)	2.06 (4)	2.884 (4)	174 (5)
N4–H17···O7	0.87 (4)	2.14 (4)	2.852 (4)	140 (5)
N4–H18···O7’	0.86 (4)	2.00 (4)	2.861 (4)	180 (5)
N5–H19···O11	0.80 (5)	2.06 (5)	2.845 (4)	167 (5)
N5–H20···O16	0.82 (3)	2.07 (3)	2.888 (4)	173 (5)
N5–H21···O14	0.80 (5)	2.31 (5)	2.933 (4)	136 (5)
N5–H21···O4	0.80 (5)	2.44 (5)	2.997 (4)	128 (5)
N5–H22···O5	0.79 (4)	2.08 (4)	2.864 (4)	175 (5)
N6–H23···O6	0.89 (4)	2.04 (4)	2.923 (4)	174 (5)
N6–H24···O12	0.84 (4)	2.04 (4)	2.860 (4)	164 (5)
N6–H25···O15	0.76 (5)	2.23 (5)	2.878 (4)	143 (5)
N6–H26···O13	0.88 (4)	2.06 (4)	2.905 (4)	161 (5)

Chapter 5

Structural phase transitions in $(NH_4)_3H(SO_4)_2$

The detailed crystal structure analysis using neutron and X-ray single-crystal diffraction for each phase was presented in chapter 4. The successive phase transitions of TAHS were characterized with various methods and are presented in this chapter. As mentioned before, a group-subgroup relationship between space group symmetries is a necessary prerequisite for a second-order phase transition, whereas a first-order phase transition may have such a group-subgroup relation, though it is not essential. In the case of TAHS, the following group-subgroup relations between the different phases exist:

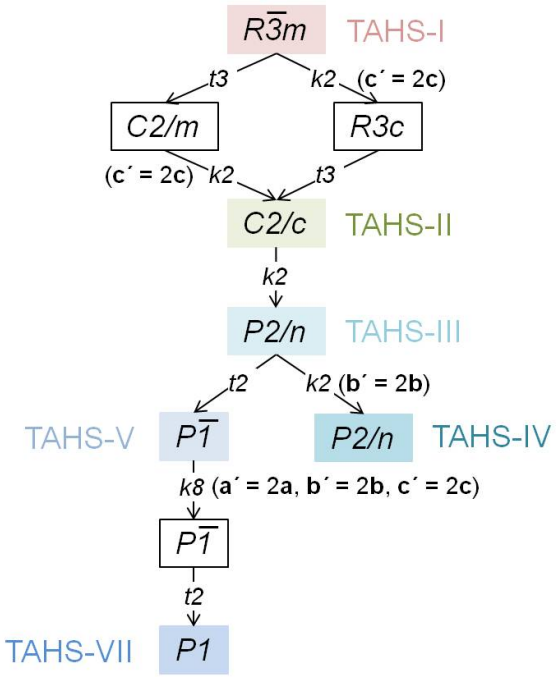

From the rhombohedral high-temperature phase I there are two possible ways of symmetry reduction to the monoclinic subgroup $C2/c$ of index 6. The $\bar{3}$-axis disappears at the I/II-phase transition and one out of three symmetry equivalent twofold axes becomes the monoclinic unique axis. With the doubling of the unit cell, the volume of the C-centred monoclinic unit cell refers to: $V_{Cm} = \frac{4}{3}V_R$. The klassengleiche phase transition from phase II to III transforms a C-centred unit cell to a primitive one. Phase IV has the same space group symmetry as phase III with a doubling of the unit cell in **b** direction. Triclinic $P\bar{1}$ is a translationengleiche subgroup of monoclinic $P2/n$ (phase III) of index 2. The transformation matrices for the I/II- and IV/V-phase transitions are:

$$\text{I} \rightarrow \text{II}; \quad \begin{pmatrix} \frac{1}{3} & \frac{2}{3} & \frac{2}{3} \\ \bar{1} & 0 & 0 \\ \bar{1} & \bar{2} & 0 \end{pmatrix} \begin{pmatrix} \mathbf{a}_r \\ \mathbf{b}_r \\ \mathbf{c}_r \end{pmatrix} = \begin{pmatrix} \mathbf{a}_m \\ \mathbf{b}_m \\ \mathbf{c}_m \end{pmatrix}$$

$$\text{IV} \rightarrow \text{V}; \quad \begin{pmatrix} \frac{1}{2} & \frac{1}{4} & 0 \\ 0 & 0 & 1 \\ 0 & \bar{1} & 0 \end{pmatrix} \begin{pmatrix} \mathbf{a}_m \\ \mathbf{b}_m \\ \mathbf{c}_m \end{pmatrix} = \begin{pmatrix} \mathbf{a}_t \\ \mathbf{b}_t \\ \mathbf{c}_t \end{pmatrix}$$

Different experiments have been carried out for an observation of a hysteresis and to distinguish between sudden or continuous changes of physical/chemical properties at the phase transitions.

5.1 Differential scanning calorimetry/Thermogravimetry

There has been a certain ambiguity about the high-temperature phase transition of TAHS. Some additional anomalies were reported in the past through dielectric and DSC measurements [13, 16] at higher temperatures than the well known I/II-phase transition at 413 K. To clarify this uncertainty, corresponding DSC/TG measurements were carried out in the temperature range RT – 493.0 (5) K with polycrystalline samples prepared in a glove box. To avoid time-dependent thermal decompositions of TAHS, a heating rate of 3 K/min was chosen. The first measurement (Fig. 5.1) showed only one phase transition at 413.5 (5) K on heating and at 412.5 (5) on cooling. The heating cycle was immediately stopped after the endothermic signal of the phase transition was observed and the sample was then directly cooled down. This measurement up to $\sim$ 428 K delivered reproducible results on repeated heating and cooling cycles. However, a different measurement, where the sample was heated up to 493.0 (5) K, kept at this temperature for two hours and cooled down again, indicated additional anomalies on

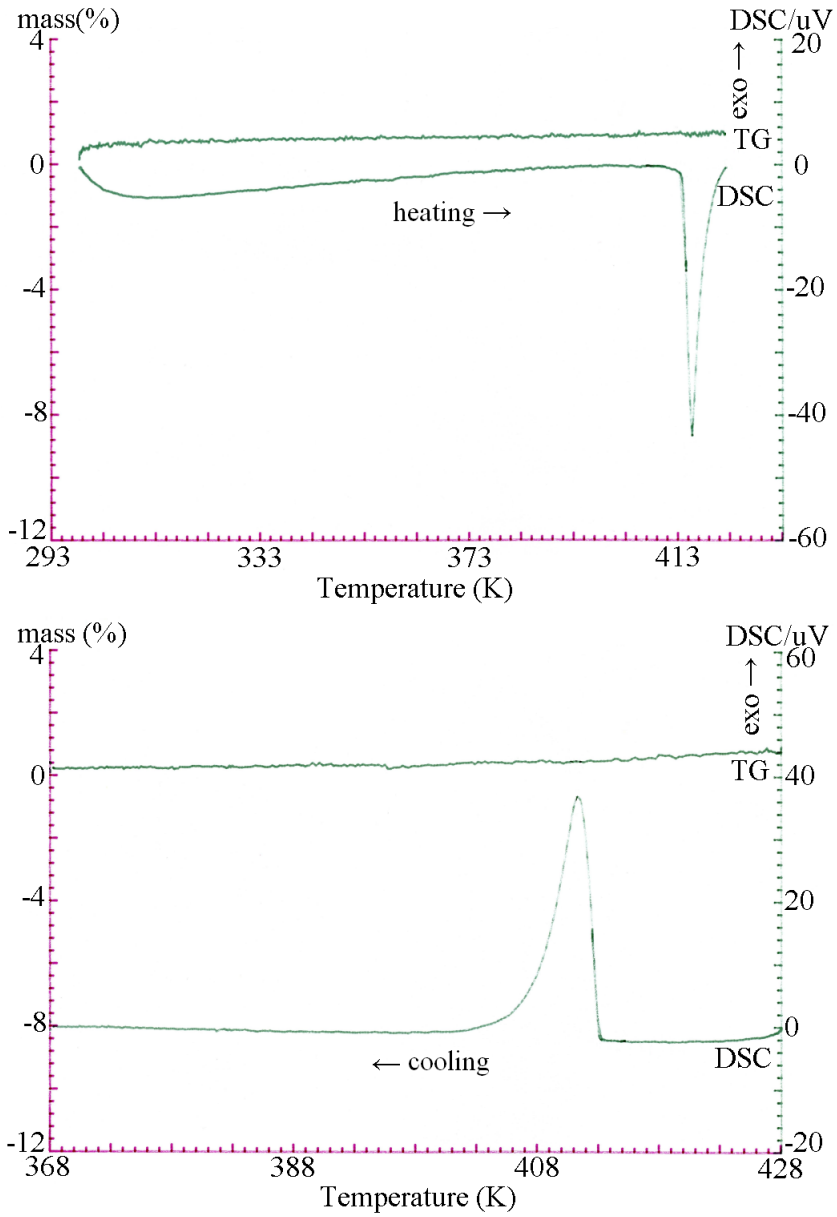

Figure 5.1: DSC/TG measurements of TAHS on heating and cooling.

cooling (Fig. 5.2). After this DSC/TG measurement the powder sample was checked for those additional anomalies using X-ray powder diffraction. In addition to the dominant volume fraction of TAHS, some minor parts of $(NH_4)H(SO_4)$ and $(NH_4)_2(SO_4)$ were detected. Hence, a beginning of a thermal decomposition took place at temperatures above the structural phase transition and the DSC/TG measurement was not reproducible. With the DSC measurements only one structural high-temperature phase transition was observed and confirmed up to 493.0 (5) K.

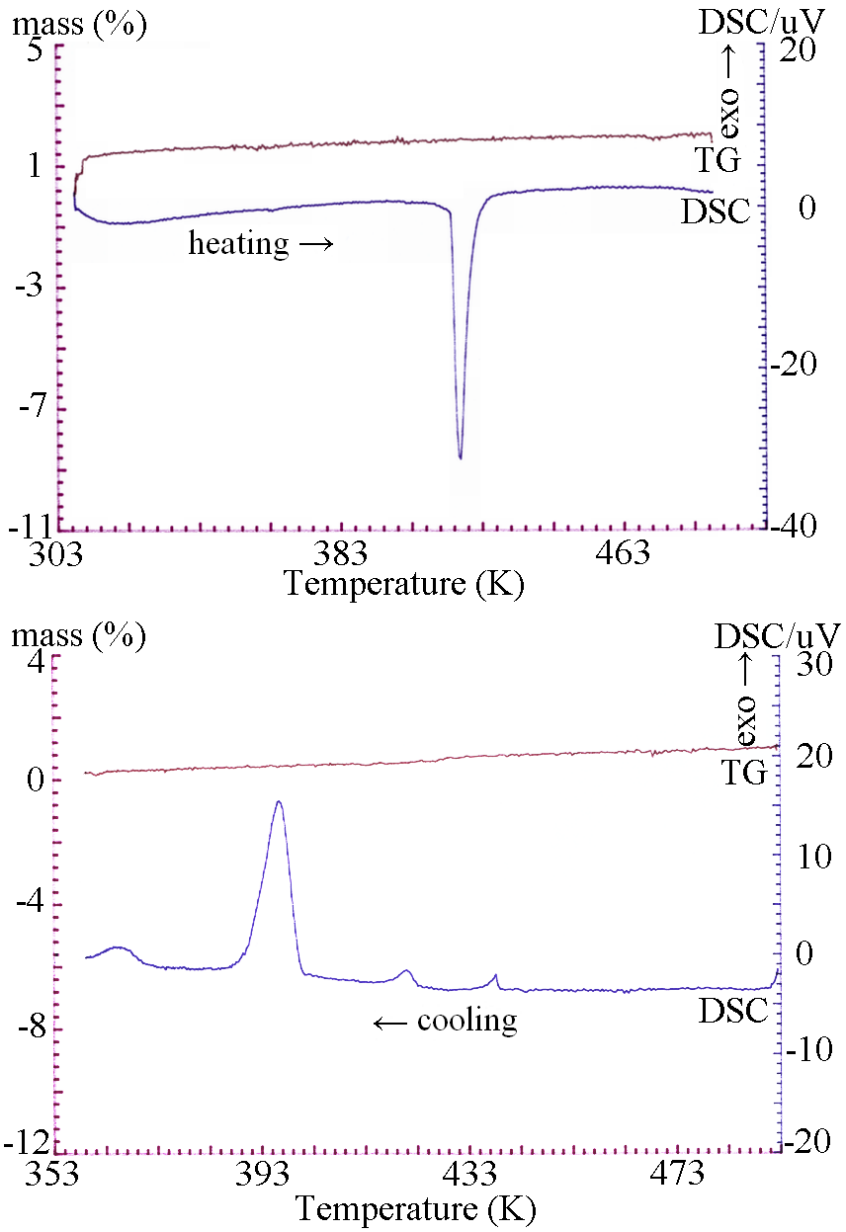

Figure 5.2: DSC/TG measurements up to 493.0 (5) K. On heating there is only one phase transition visible and several new anomalies appear on cooling after the sample was kept at 493.0 (5) K for two hours.

5.2 Temperature-dependent X-ray powder diffraction

A temperature-dependent X-ray powder diffraction study was carried out on TAHS for the whole temperature range between 8 and 427 K. Since the powder diffraction method provides accurate lattice parameters, these were used for the crystal structure refinements in this dissertation. Changes of the crystal structure can be recognized

by X-ray powder diffraction corresponding to the following phenomena: i) if a crystal structure transforms to a new space group symmetry at the phase transition, the pattern of the powder diffractograms alters, for example, observed peaks vanish or additional peaks appear as well as peaks merge or split at the phase transition (see Fig. 5.3); ii) on heating and cooling of the powder sample the crystal lattice experiences volume

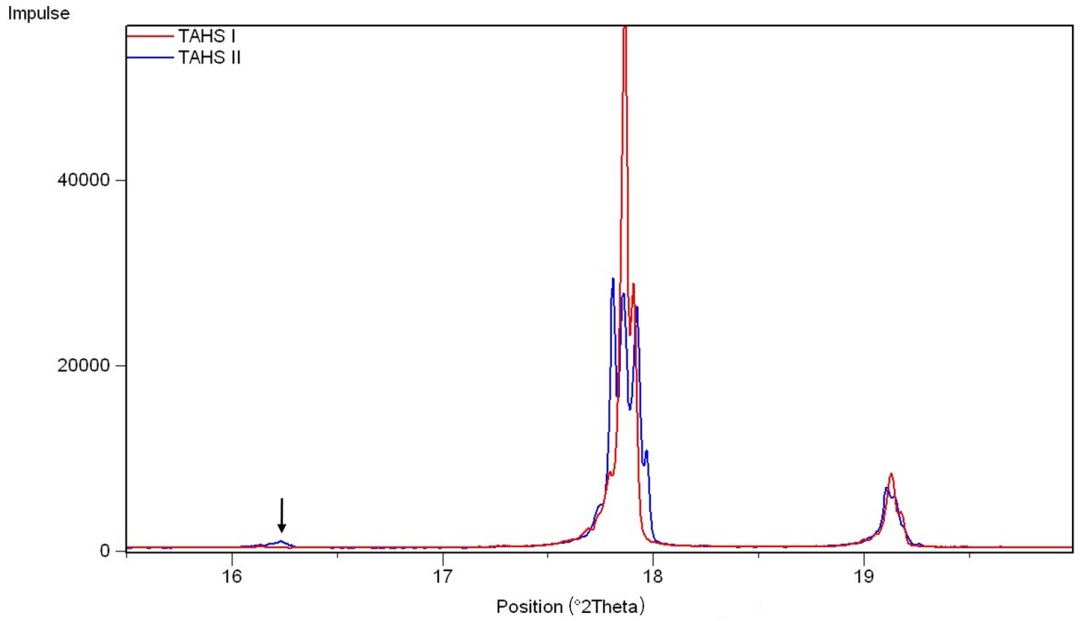

Figure 5.3: Disappearance (arrow) and merging of reflections at the I/II-phase transition.

expansion or contraction. Therefore a shift of peak positions in 2Θ occurs (Fig. 5.4); iii) the profile matching of the whole powder pattern yields very accurate peak positions, from which precise lattice parameters can be obtained. The development of lattice parameters as a function of temperature can give information about the characteristics of phase transitions. For example, an abrupt change and an observation of a clear hysteresis characterize a first-order phase transition, whereas a continuous change is expected for a second-order phase transition. In Fig. 5.5 the temperature dependence of the lattice parameters of TAHS is shown in the temperature range of 8 – 427 K on heating and cooling. At the phase transitions, I/II, IV/V and V/VII, there exists a clear hysteresis with drastic changes of lattice parameters. Hence these phase transitions are characterized as being first-order transitions. Below the V/VII-phase transition, additional peaks were first observed on cooling at 70 K (see Fig. 5.6). These additional reflections could be explained by a doubling of the unit cell in all crystallographic directions. On heating, those additional peaks remained up to 85 (1) K and vanished

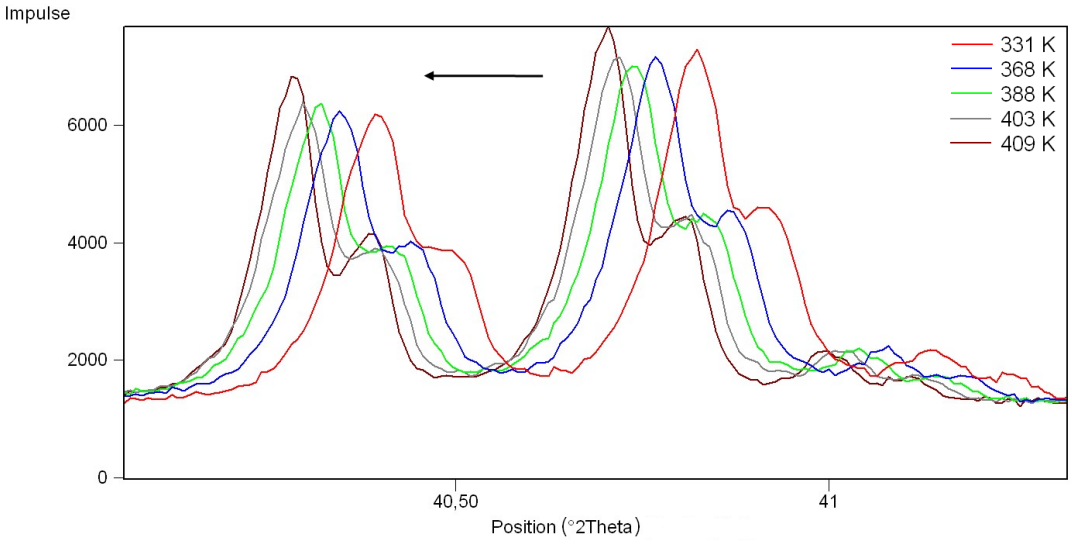

Figure 5.4: Shift of reflection positions to lower 2Θ-values on heating TAHS-II.

again. The rest of the X-ray powder measurements gave reproducible results on heating up to room-temperature. The refinement of measured powder diffraction data was especially challenging below 85 (1) K where there exist both phases V and VII. In the case of first-order phase transitions, a coexistence of both phases is common at the phase transition as can be seen in Fig. 5.7. On the other hand, the II/III- and III/IV-phase transitions show neither hysteresis nor abrupt variation of the lattice parameters and the curves change rather continuously. These transitions are of second-order. The observed phase transition temperatures from X-ray powder diffraction are given in Table 5.1 together with corresponding literature values.

Table 5.1: Phase transition temperatures (K) of TAHS on cooling and heating.

Phase transition	Literature *	Cooling	Heating
I ↔ II	413 [18]	402.6 (1)	412.9 (1)
II ↔ III	265 [2]	265.0 (1)	265.0 (1)
III ↔ IV	141 [2]	141.0 (1)	141.0 (1)
IV ↔ V	133 [2]	133.0 (1)	138.0 (1)
V ↔ VII	63 [3]	70 (1)	85 (1)

* [18] on heating, [2] on cooling, [3] mean value from 46 K on cooling and 78 K on heating.

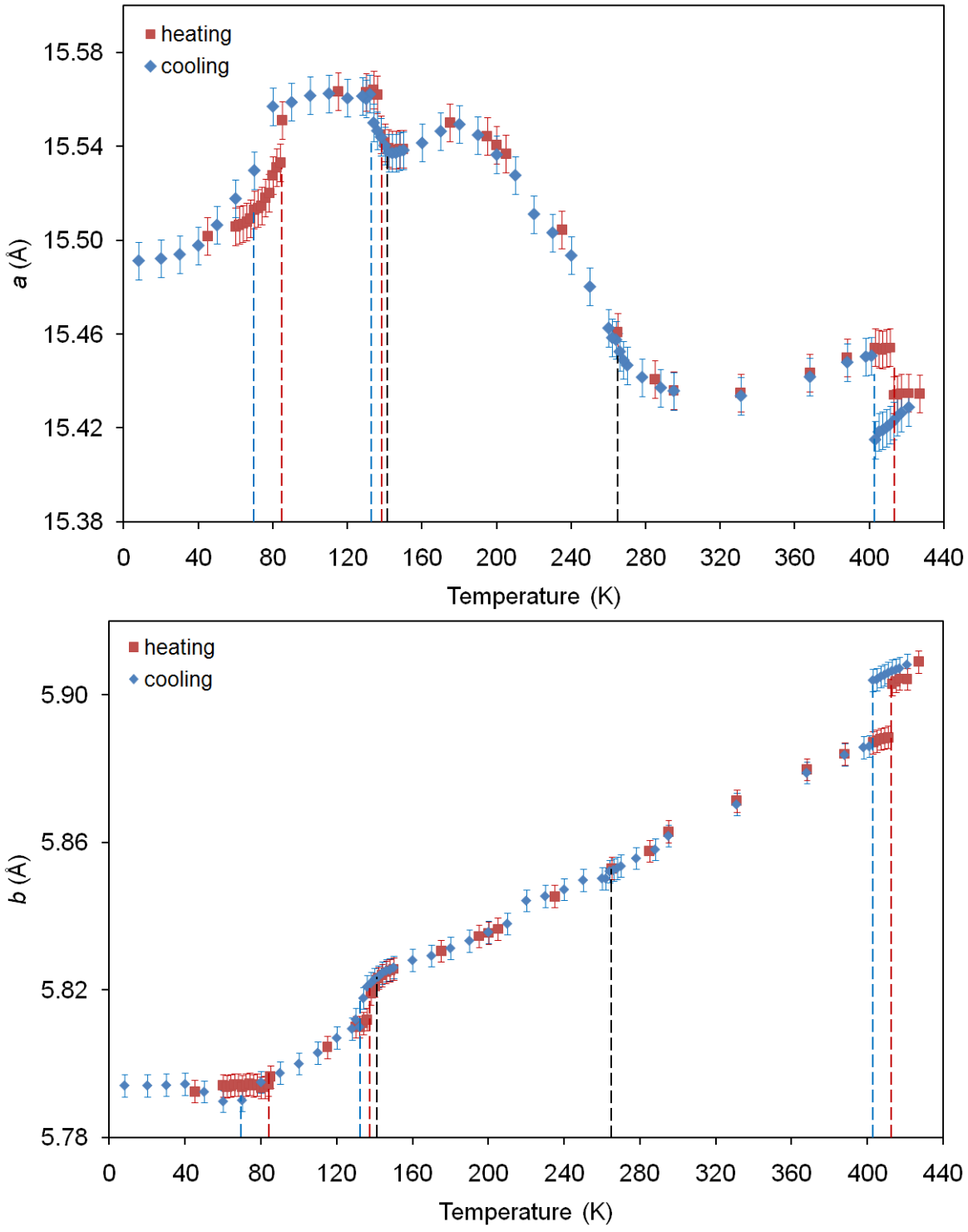

Figure 5.5: Temperature dependence of lattice parameters of TAHS (normalized to the unit cell of TAHS-II) in the temperature range 8 to 427 K on heating and cooling. The vertical dashed lines mark the phase transition temperatures: red on heating, blue on cooling and black for the second-order phase transition.

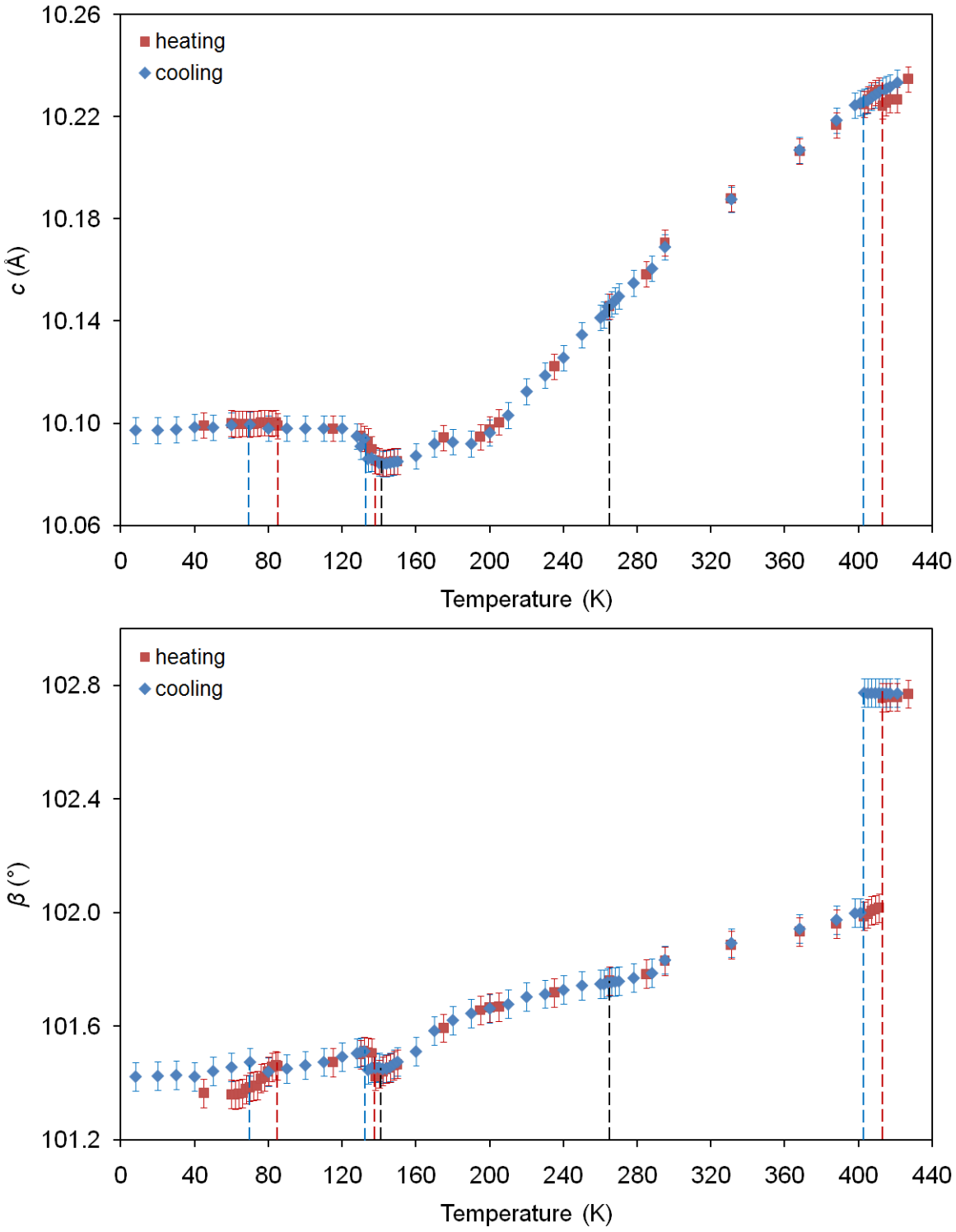

Figure 5.5 - continued

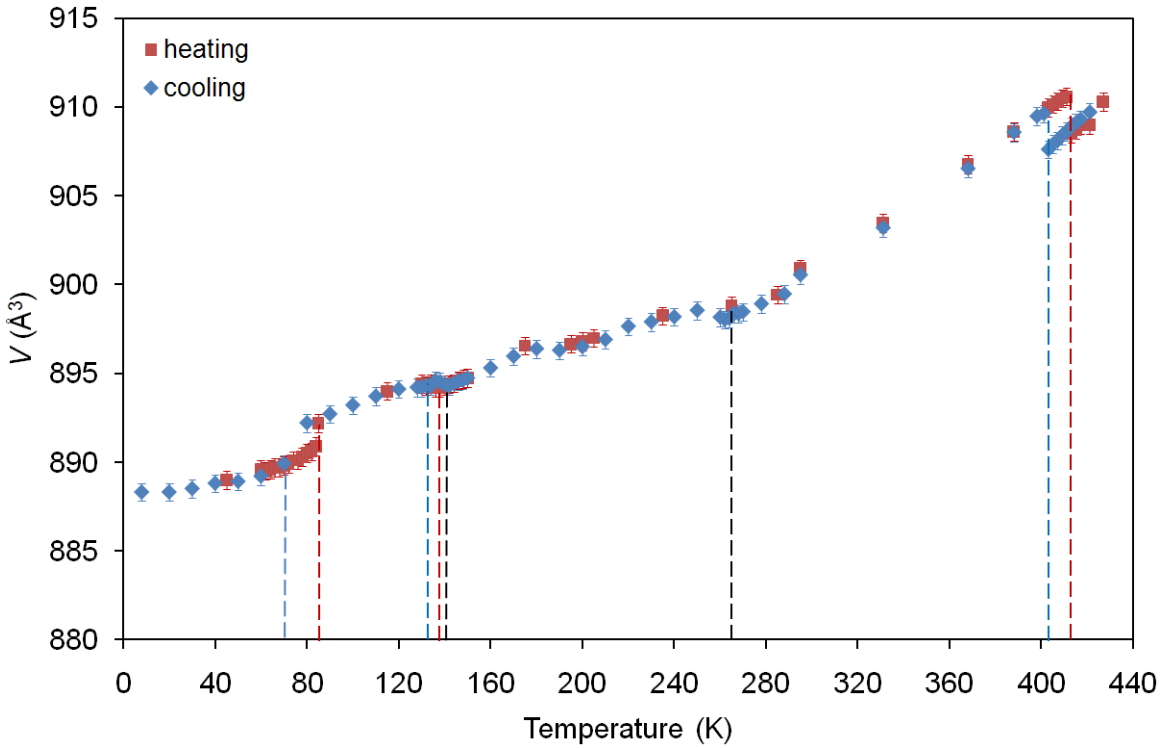

Figure 5.5 - continued

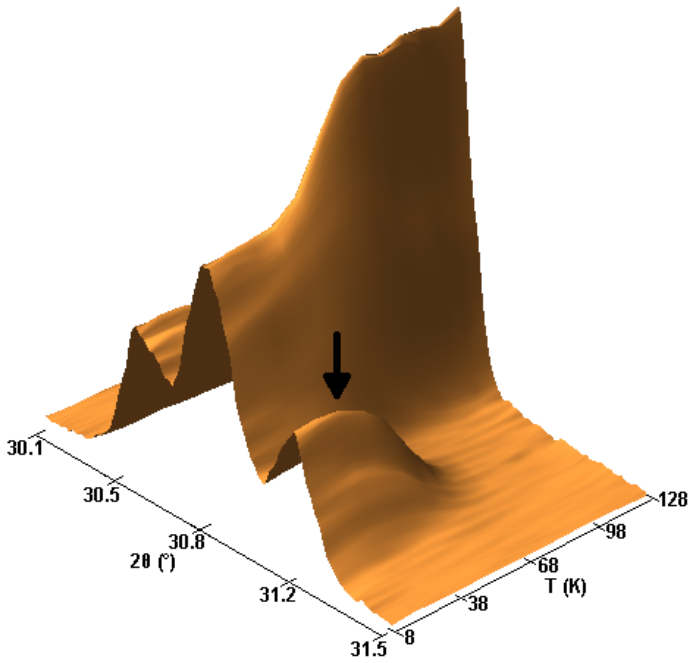

Figure 5.6: An additional peak (marked with an arrow) in TAHS-VII on cooling.

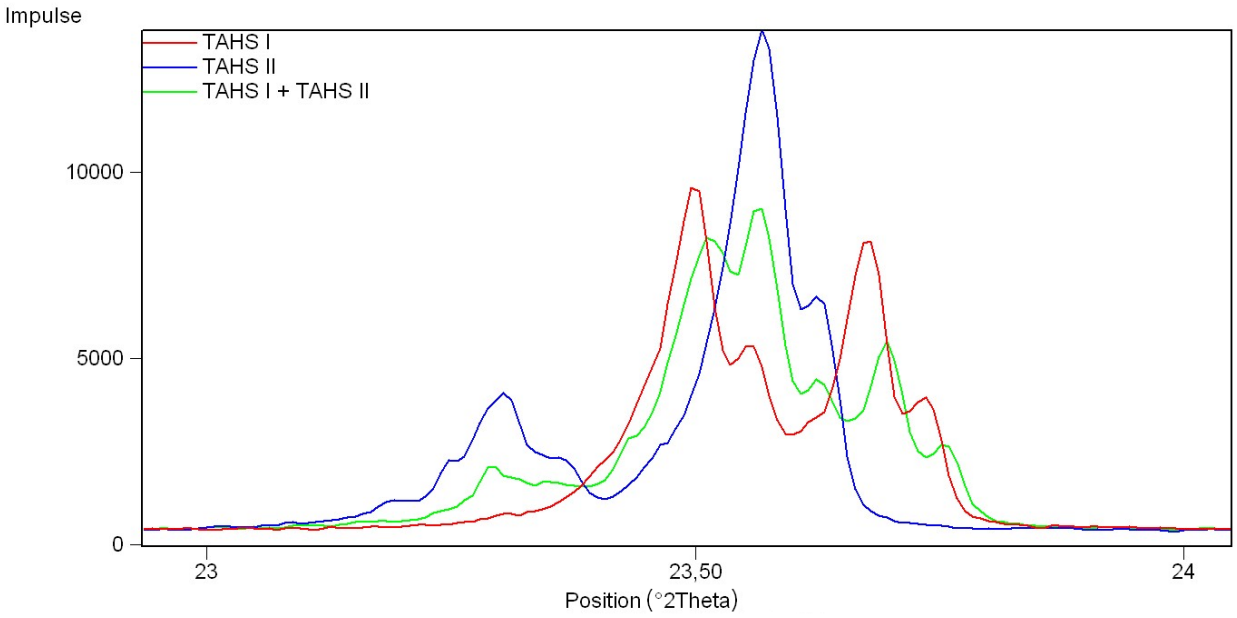

Figure 5.7: Coexistence of the rhombohedral phase I and the monoclinic phase II of TAHS at 403 K.

5.3 Temperature-dependent neutron single-crystal diffraction

To detect a phase transition with neutron single-crystal diffraction, certain Bragg reflections were chosen beforehand which vanish or appear at the transition. Fig. 5.8 shows the integral intensity of the monoclinic $\bar{2}21$-reflection as a function of temperature. A sudden fall in the Bragg reflection intensities as well as an abrupt increase of the FWHM (full width at half maximum) were observed on heating at the I/II-phase transition (see Fig. 5.9). Both phenomena start at a lower temperature of $\sim$ 403 K than the reported 413 K.

The II/III-phase transition has a second-order character and could be confirmed through the continuous increase of Bragg reflection intensities of some selected superstructure reflections on cooling (see Fig. 5.10). The order parameter could be derived from the development of the superstructure reflection intensities together with the refinement of the order/disorder-features in TAHS-III using the following equations:

$$I(T) = const. \cdot (T_c - T)^{2\beta} \rightarrow O_i(T) = a \cdot (T_c - T)^{\beta} + b$$

where the critical exponent, $\beta = 0.218\,(5)$. The degree of order as a function of tem-

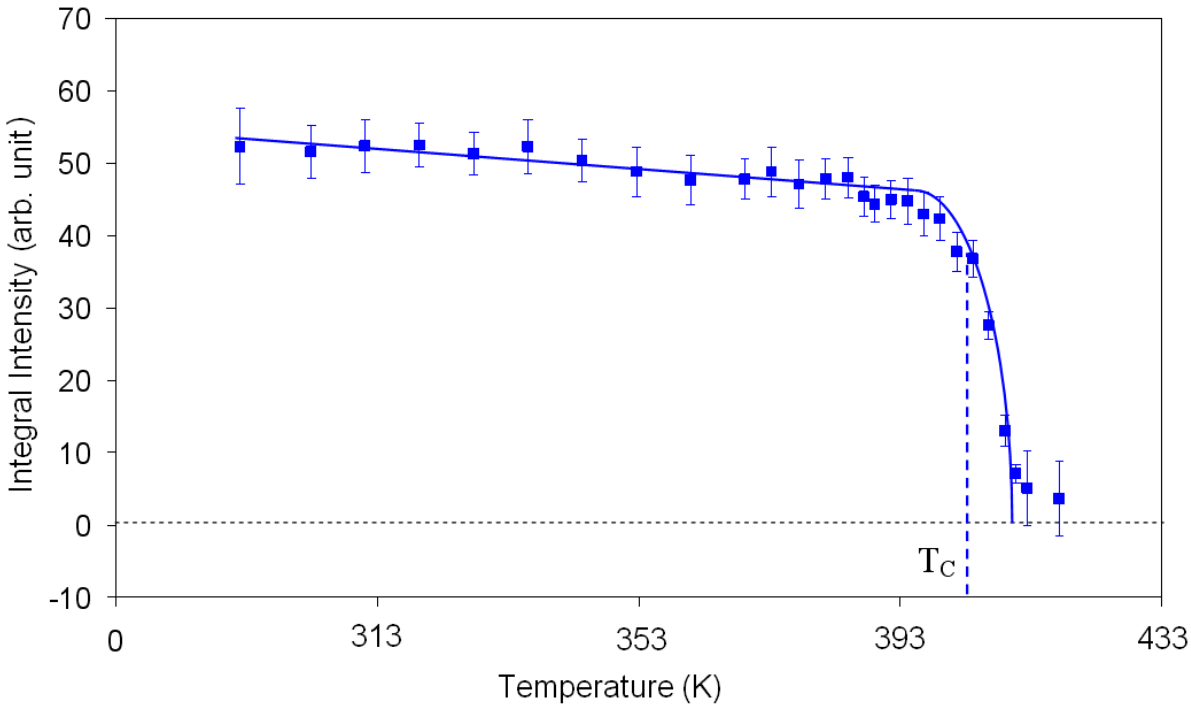

Figure 5.8: The $\bar{2}21$-reflection of the monoclinic phase II of TAHS vanishes at the I/II-phase transition.

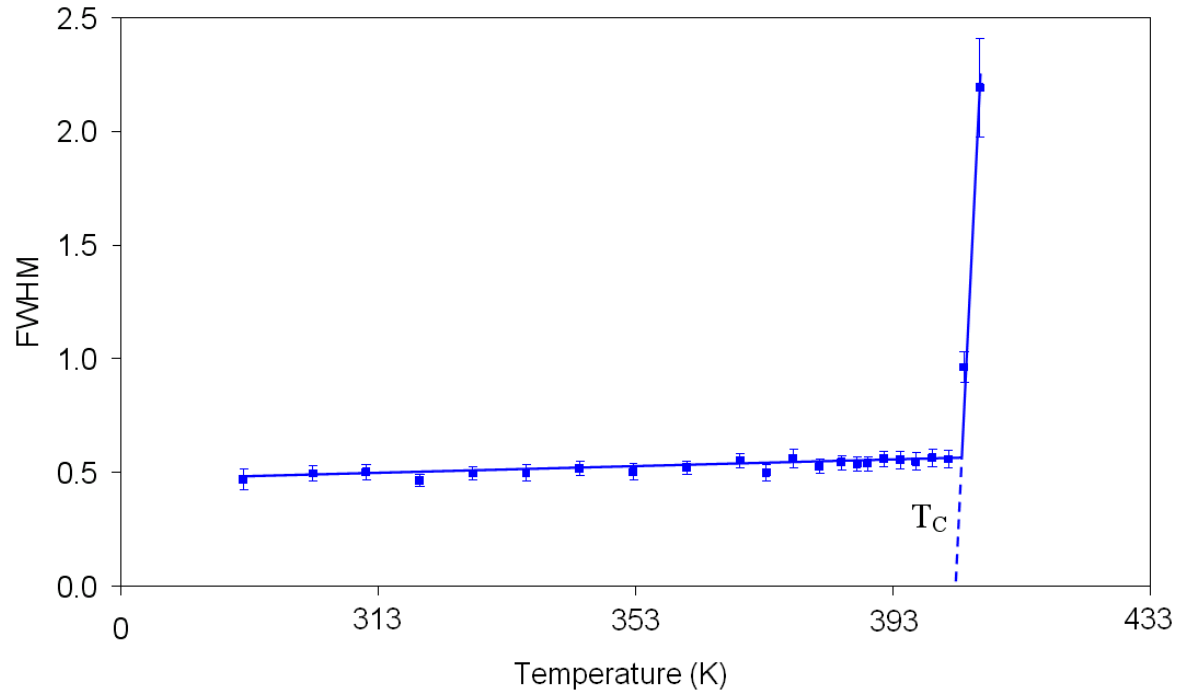

Figure 5.9: A drastic increase in FWHM of the $\bar{2}21$-reflection from the monoclinic TAHS-II at the I/II-phase transition.

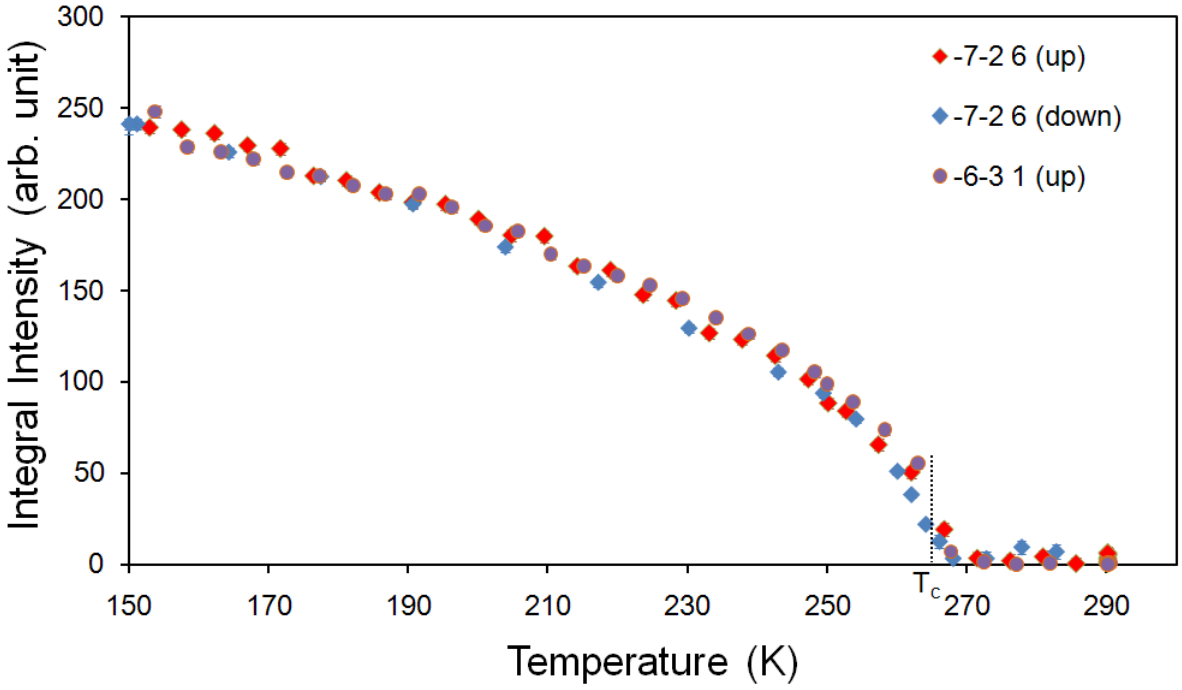

Figure 5.10: A continuous change of integral intensities for the chosen superstructure reflections on heating and cooling in TAHS-III.

perature, extrapolated down to 0 K, has been illustrated in chapter 4 (Fig. 4.16). It is remarkable that the degree of order never reaches 100 % even at 0 K. This supports the idea of dynamical H-disorder in TAHS, in which the ordering process increases with decreasing temperature and freezes at low temperatures.

The doubling of the unit cell in TAHS-IV could also be observed with some additional superstructure reflections that appear at the III/IV-phase transition. Fig. 5.11 depicts the integral intensity of the $91\bar{2}$-reflection and its FWHM on heating as a function of temperature. The intensity develops continuously and a fitting curve has been calculated as shown in Fig. 5.11a). The calculated critical exponent, β, and T_c are 0.24 (2) and 141.9 (2), respectively.

As mentioned in the previous chapter, splitting of some reflections was observed at the IV/V-phase transition using single-crystal neutron diffraction. Moreover, a distinct hysteresis of ~ 4 K was found. As shown in Fig. 5.12, two split reflection positions were observed in phase V with the ω-scan technique. In Fig. 5.13 the integral intensity of the 040-reflection is plotted as a function of temperature. For the phase V the integral intensity represents the sum of the split reflections.

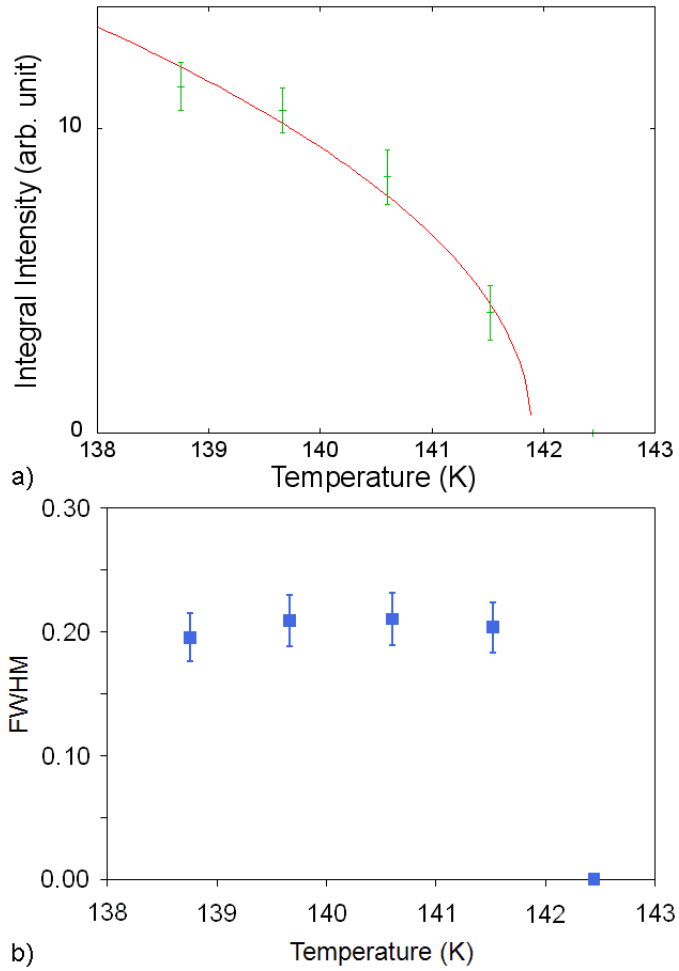

Figure 5.11: Superstructure reflection at the III/IV-phase transition: a) Integral intensity of the $91\bar{2}$-reflection on heating as a function of temperature. The green bars mark measured intensities with errors and the red curve has been derived from the fitted function to the intensities using the critical exponent $\beta = 0.24\,(2)$. b) The FWHM of the $91\bar{2}$-reflection on heating corresponds to the width of the main reflections.

Mechanism of structural phase transitions of TAHS

On the basis of structural investigations carried out with X-ray and neutron diffraction, a better understanding of the mechanism of the structural phase transitions in TAHS was obtained. The first-order I/II-phase transition is accompanied by a symmetry reduction, in which the $\bar{3}$-axis of the rhombohedral phase disappears. The SO_4–H–SO_4 hydrogen bonds in the high-temperature phase I form a network in the (001) plane. This is possible, since the O atoms involved in the hydrogen bonds are disordered and are located on three symmetry equivalent positions. From each oxygen an O–H–O hydrogen bond is formed with the neighbouring oxygens, in this way spanning a two-dimensional

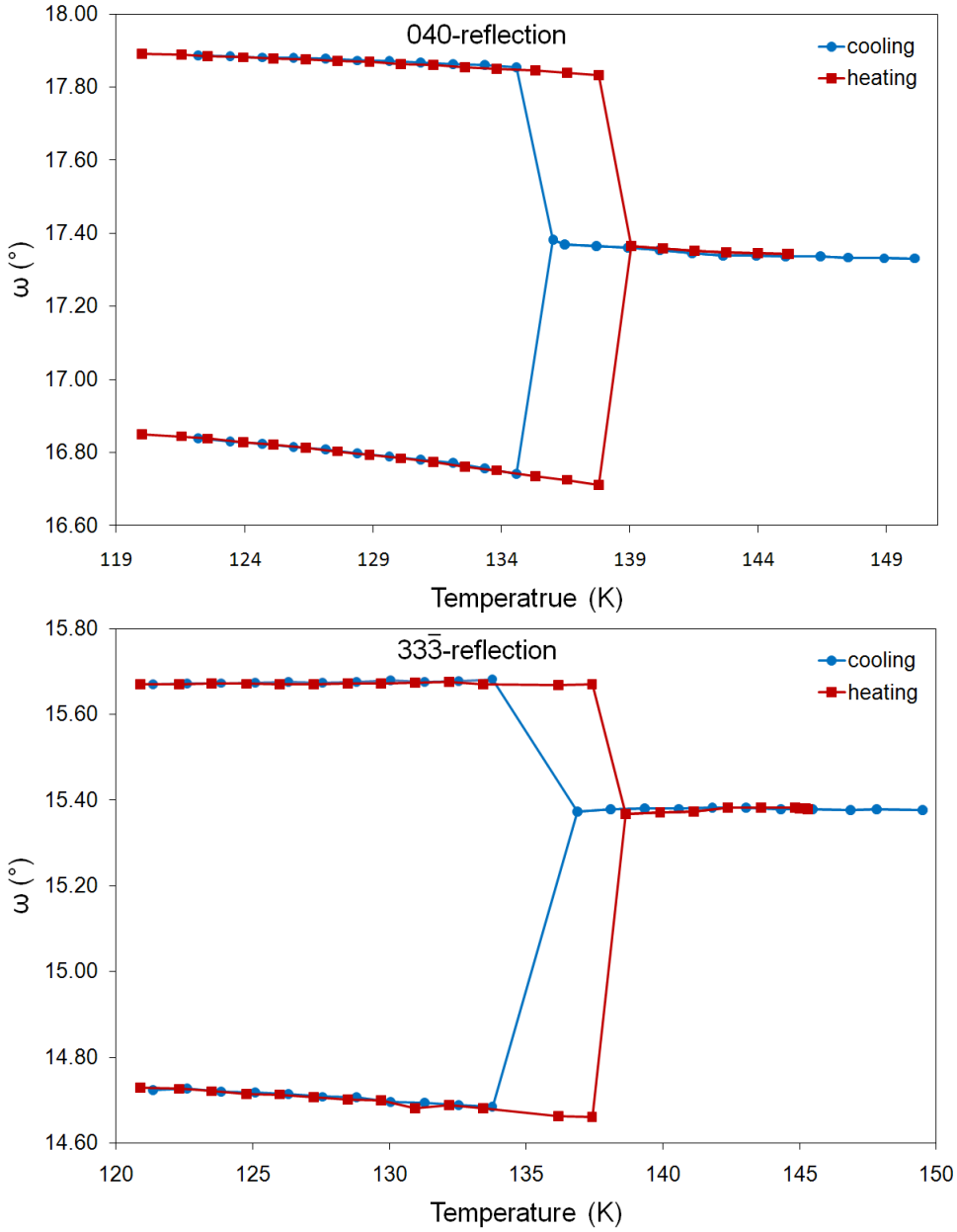

Figure 5.12: Peak positions of ω-scans of split reflections in TAHS-V as a function of temperature. The splitting of reflections is observable on cooling and disappears on subsequent heating.

pseudo-hexagonal network perpendicular to the crystallographic **c** direction. The occupation probability of each hydrogen bond is only one third, and according to the split-atom model, the proton can jump between six energetically equivalent sites. With the loss of the $\bar{3}$-axis, every S and O atoms occupy general positions in the room-temperature phase II and thus isolated $(SO_4)H(SO_4)$ dimers are formed. The O–H–O

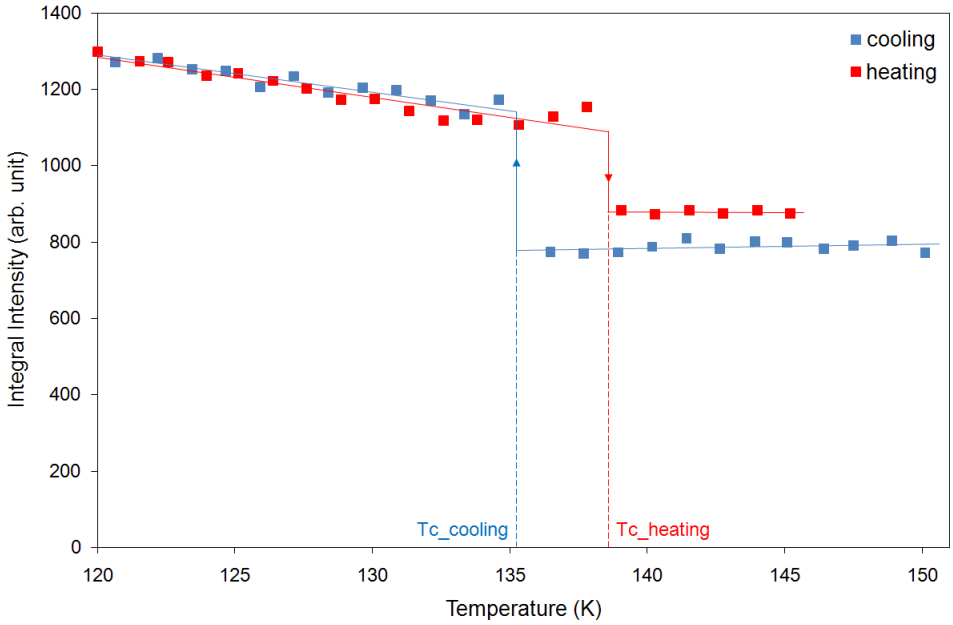

Figure 5.13: Integral intensity of the 040-reflection as a function of temperature. The errors lie within the filled square boxes.

hydrogen bond of each dimer is fully occupied. There still remains a double minimum potential for the H atom on applying the split-atom model. Furthermore, the NH_4 tetrahedral groups in phase I are strongly disordered due to their high site symmetry. There are six different possible orientations of these groups and the hydrogen-atom positions are not fully occupied. On the other hand, at the I/II-phase transition one of the NH_4 groups moves to a general and the two other still remain on special positions, though with a lower site symmetry (from $\bar{3}m$ to 2). The NH_4 groups in the high-temperature phase could best be described with the orientational disorder. N atoms are located on special positions with high site symmetries ($\bar{3}m$ and $3m$). In addition, there are bifurcated N–H$\cdots$O hydrogen bonds with surrounding oxygens, giving rise to the H split-atom positions. This splitting again causes more than one possible orientation for the NH_4 group. According to the symmetry reduction, each NH_4 group forms an ordinary tetrahedron in phase II, however, the competing situation of the N–H$\cdots$O hydrogen bonds with the neighbouring O atoms still exists. Therefore, the reorientational behaviour of the ammonium groups still exists in the room-temperature phase II. As was reported and postulated earlier [17], the successive ordering of reorientational behaviour of ammonium groups is very closely related to the further structural phase transitions in TAHS at lower temperatures. This phenomenon could be verified with neutron single-crystal diffraction. Beside the precise localization of the protons

around each nitrogen, the anisotropic displacement parameters of the protons could also be refined in the crystal structure analyses. Fig. 5.14 illustrates the development of the equivalent U-values of both nitrogen and corresponding protons in each ammonium group as a function of temperature. The denotation of the N atoms refers to that of the low temperature phase III. The equivalent U-values for the protons of the ammonium groups on special positions (N1 and N2) are larger than those of NH_4 on general positions. This result was interpreted as a stronger librational motion of the NH_4 groups on special positions. As can be seen in the illustration, the protons of the ammonium groups on special positions do not show any distinct changes of their equivalent U-values at the II/III-phase transition, whereas those of NH_4 on general positions show a clear decrease. This points to an ordering of the ammonium groups on general positions at the II/III-phase transition. Between $N3H_4$ and $N4H_4$ groups, the "freezing" of the latter one is more pronounced. Moreover, at the III/IV-phase transition, a sudden reduction of the equivalent U-values of the $N2H_4$ group is noticeable. Considering the N–H$\cdots$O bond distances and angles of this particular ammonium group, the stronger N–H$\cdots$O hydrogen bonds become even stronger in phase IV and the weaker one even weaker. Thus, a localization of this group on a well defined position can be assumed at the III/IV-phase transition. Since the low-temperature phase IV exists only within a very narrow temperature range and the following low-temperature phase transition takes place directly after a few K, the driving force that causes the IV/V-phase transition may be very similar to that for the III/IV-phase transition. The slight decrease of the equivalent U-values for H4 at the III/IV-phase transition, as shown in Fig. 5.14, can be interpreted as a beginning of an ordering of this group. Unfortunately, no direct comparison between the phases IV and V could be made due to the different diffraction methods used, especially concerning the evaluation of the protons. All the ammonium groups in phase V are located on general positions of a completely ordered crystal structure. Hence, it can be concluded that the "freezing" of the $N1H_4$ group is responsible for the IV/V-phase transition. From the observation of the equivalent U-values for the protons as well as from the structural information regarding the bond distances and angles of each ammonium group (described in chapter 4), the successive freezing of the individual groups was recognized and their specific roles for the different phase transitions could be distinguished.

An additional remark can be taken from the development of the equivalent U-values of N and S. As shown in Fig. 5.15, there is a harmonic behaviour (linear) of the equivalent U-values below $\sim$ 300 K. At T $>$ 300 K the behaviour becomes non-linear,

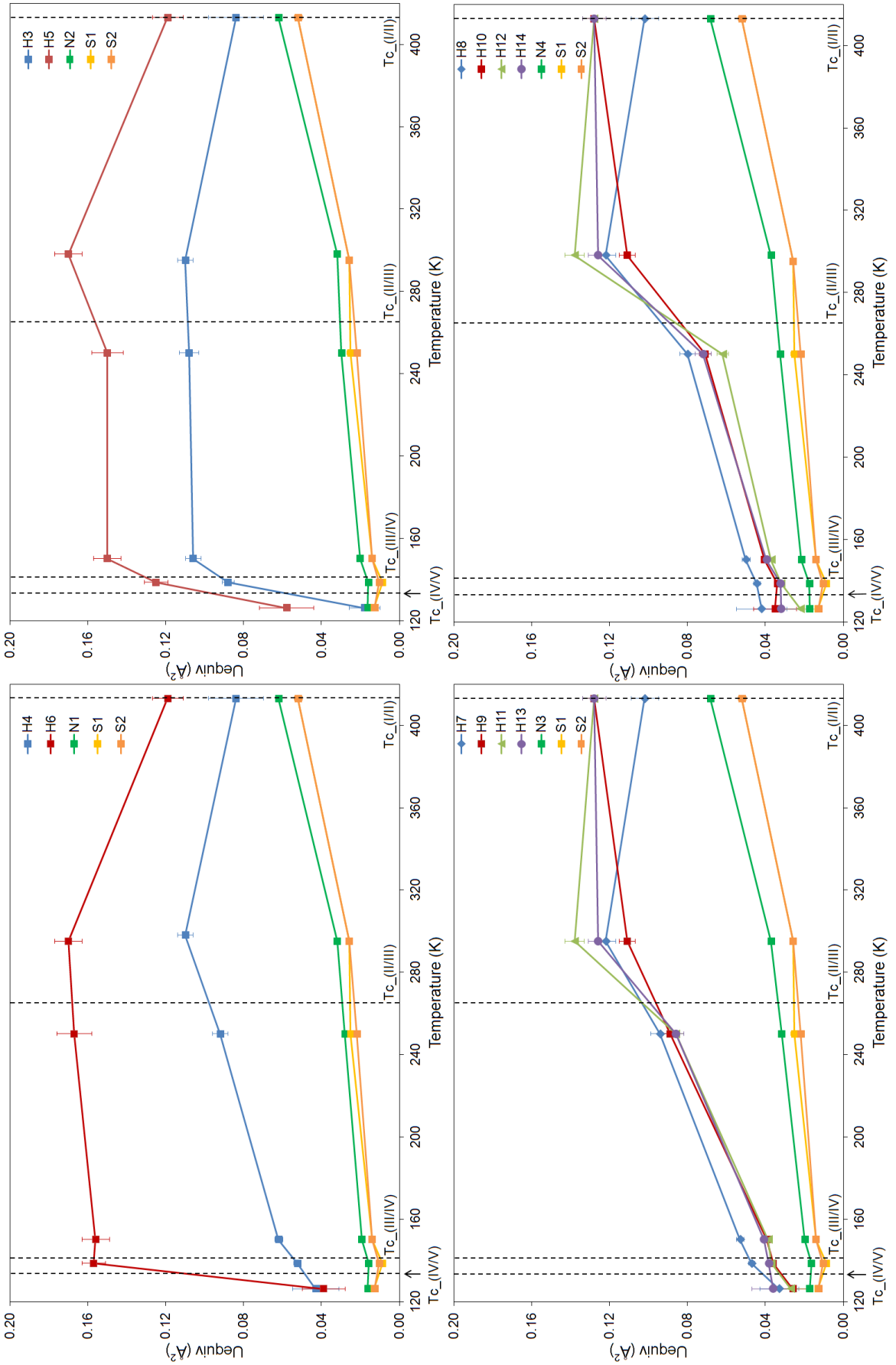

Figure 5.14: Equivalent U-values of nitrogen and corresponding protons for the different ammonium groups as a function of temperature. The phase transition temperatures are marked by vertical dashed lines. Equivalent U-values of sulphur are also illustrated for a comparison.

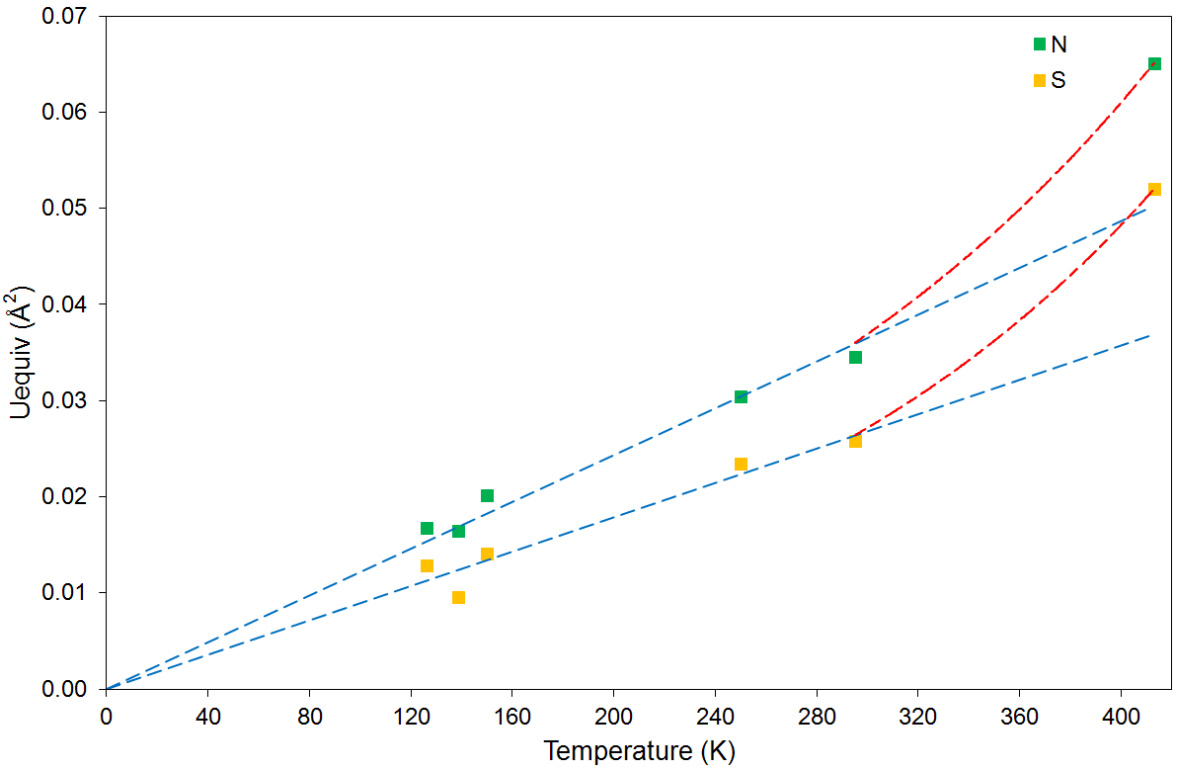

Figure 5.15: Development of the equivalent U-values (N and S) as a function of temperature. Harmonic (linear) behaviour below $\sim$ 300 K and anharmonic (curve) contribution for T $>$ 300 K.

indicating anharmonic potential that is contributed to the protonic conductivity. Complementary to this behaviour, an increase of background intensity was observed at T $>$ 300 K with the X-ray powder diffraction.

Chapter 6

Conductivity measurements on $(NH_4)_3H(SO_4)_2$

For the conductivity measurements on TAHS, three single-crystal samples with different orientations (monoclinic **a, b, c**) were used. The experimental impedance Cole-Cole plots were obtained at different temperatures with the frequency range of 1 Hz – 500 kHz (see Fig. 6.1). From these plots the real parts at the local minimum of the imaginary

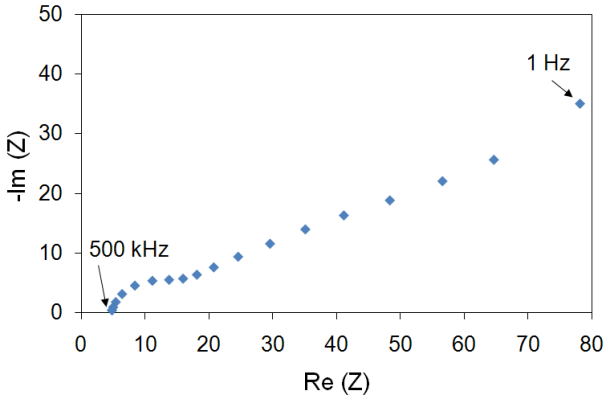

Figure 6.1: The Cole-Cole plot of the frequency dependent impedance measurement along the monoclinic **b**-axis of TAHS at 377 K.

parts are read as the electrical resistance, R (Ω) of the sample. The conductivity, σ is then calculated with the following equation with the electrode's area and the distance between two electrodes which is the thickness of the sample:

$$\sigma\ (\Omega^{-1}\ \mathrm{cm}^{-1}) = \text{length (cm)}\ /\ \text{R}\ (\Omega) \times\ \text{area}\ (\mathrm{cm}^2)$$

In general, the temperature dependent conductivity of a crystal is expressed by the following Arrhenius equation:

$$\sigma T = A \exp(-H/k_B T)$$

where A is the pre-exponential factor, H the activation enthalpy and k_B the Boltzmann constant. The logarithmic Arrhenius plot of σ versus 1/T is shown in Fig. 6.2 for the

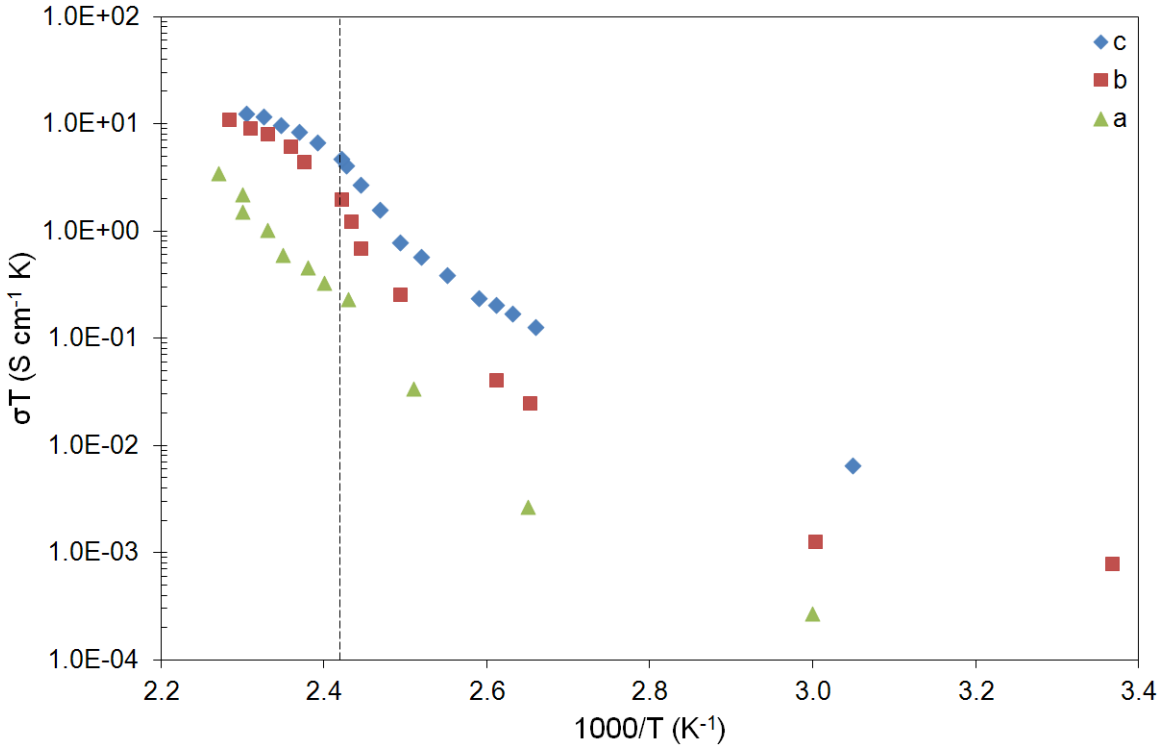

Figure 6.2: Temperature-dependent Arrhenius plot of σ in different crystallographic axes. The I/II-phase transition of TAHS is marked with a vertical dashed line at 413 K.

different crystallographic axes of TAHS. From the slope of this plot the activation enthalpy, H can be calculated and the y-axis intercept corresponds to the value of the pre-exponential factor, A. They are given in Table 6.1 for the different crystallographic directions (parallel to monoclinic **a, b, c**) and for the temperature ranges below and above the I/II-phase transition temperature of 413 K. The values in the Table 6.1 are though limited in the analysis, because the whole conductivity measurement needed a relatively long time for the temperature setting. This probably caused a slight change of the sample in its quality, especially in the high-temperature range. According to the direct contact of the sample surface with the electrodes, it is rather critical to prevent

Table 6.1: Activation enthalpy, H and pre-exponential factor, A of the Arrhenius equation.

Temperature [K]	monoclinic axes	H [eV]	A [S cm^{-1} K]
	a	0.81	$5.3{\cdot}10^8$
< 413	**b**	0.75	$2.7{\cdot}10^8$
	c	0.67	$1.1{\cdot}10^8$
	a	0.45	$3.9{\cdot}10^5$
> 413	**b**	0.23	$4.5{\cdot}10^3$
	c	0.23	$5.6{\cdot}10^3$

chemical reaction at the surface, which can easily affect the results of the conductivity measurement. The X-ray powder diffraction of the sample after the conductivity measurement (Fig. 6.3) showed a minor amount of $(NH_4)_2(SO_4)$ beside the silver-peaks (contact material for the electrodes). From this, a beginning of thermal decomposition could have occurred at high temperatures.

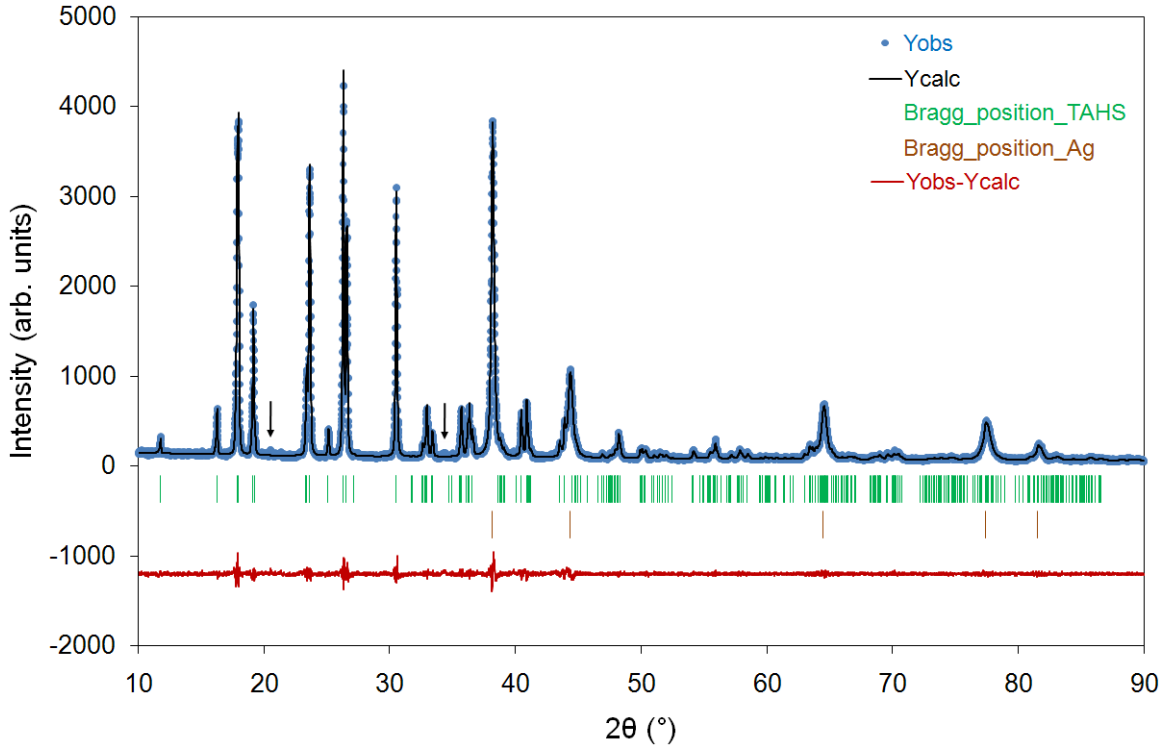

Figure 6.3: X-ray powder diffraction of the TAHS-sample after the conductivity measurement (profile matching). Small additional peaks from $(NH_4)_2(SO_4)$ are marked with arrows.

The geometrical relation between the monoclinic and rhombohedral axes (hexagonal setting) is illustrated in Fig. 6.4 according to the following transformation matrix:

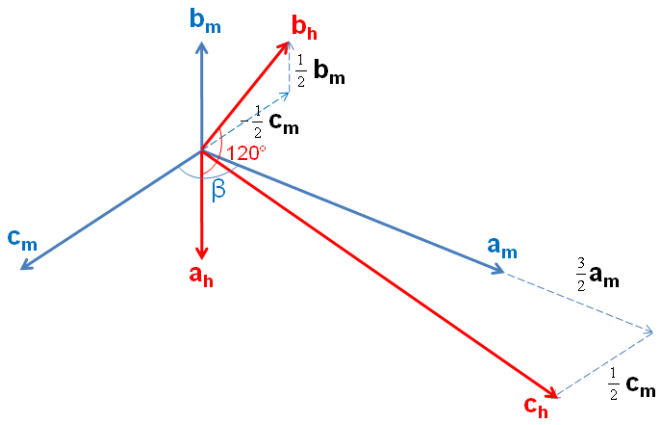

Figure 6.4: Geometrical relation between the monoclinic and hexagonal axes.

$$\begin{pmatrix} 0 & \bar{1} & 0 \\ 0 & \frac{1}{2} & \frac{\bar{1}}{2} \\ \frac{3}{2} & 0 & \frac{1}{2} \end{pmatrix} \begin{pmatrix} \mathbf{a}_m \\ \mathbf{b}_m \\ \mathbf{c}_m \end{pmatrix} = \begin{pmatrix} \mathbf{a}_h \\ \mathbf{b}_h \\ \mathbf{c}_h \end{pmatrix}$$

The monoclinic **b**-axis becomes the hexagonal **a**-axis in opposite direction and the monoclinic **a** direction refers approximately to the rhombohedral **c** direction and hence the conductivity in that direction is the lowest. Above the I/II-phase transition temperature, the conductivity in the monoclinic **b** and **c** direction yields a very similar development, since the conductivity of the high-temperature phase allows an isotropic character in the hexagonal (001) plane due to the point group symmetry. They have the value of $\sim 10^{-2}$ S cm^{-1}, which is typical for superionic conductors.

As shown in Fig. 4.9 (chapter 4.1 High-temperature phase I), the two-dimensional O–H–O hydrogen bond network with the partially occupied H-atom positions enables proton conductivity in the (001) plane. The conductivity is apparently supported by the ammonium groups lying in the middle of the six-membered ring, from which proton diffusion can occur. The nuclear density map of the single-crystal neutron diffraction analysis illustrated the possible pathways for proton conduction in the (001) plane of TAHS-I. The proton conduction in the high-temperature phase is due to the highly-disordered crystal structure, in which proton can migrate through the symmetrically equivalent sites. Whereas every O–H–O hydrogen bond site in the high-temperature phase is only one third occupied, it is fully occupied in the room-temperature phase and isolated $(SO_4)H(SO_4)$ dimers are built in the monoclinic (**b**,**c**) plane (see Fig. 6.5). The

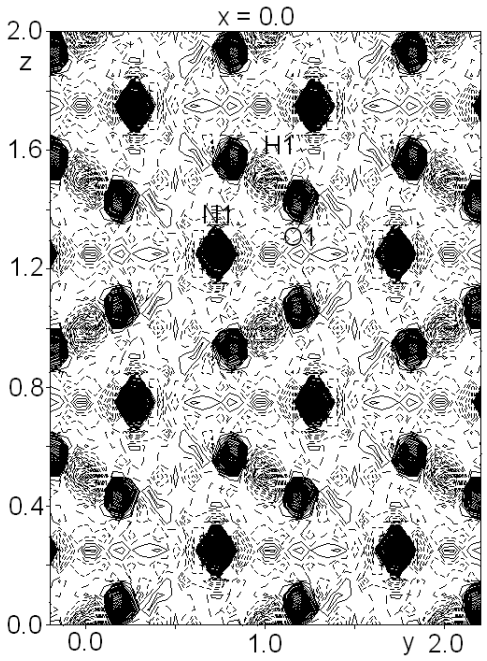

Figure 6.5: Nuclear density map F_{obs} of hydrogen bonds in the monoclinic (**b**,**c**) plane (TAHS-II at 295 K). Positive contours (solid line) and negative contours (dotted line) are drawn in steps of 0.5 fm·Å^{-3}.

results of the conductivity measurements show a clear anisotropy with respect to the different monoclinic directions. The proton conduction in the monoclinic **c** direction is the highest and the possible pathway is illustrated in Fig. 6.6 by solid lines. The O–H–O hydrogen bond builds a zig-zag path along the monoclinic **c** direction and the $N1H_4$ group is located between two hydrogen bonds. The librational motion of this ammonium group is the strongest around the monoclinic **a** direction as shown in Table 4.10. This means, that they strongly reorientate in the (**b**,**c**) plane and can therefore very easily allow the proton diffusion along the zig-zag forming hydrogen bonds. On the other hand, along the **b** direction, the hydrogen bonds are aligned parallel to each other within the layer of $(SO_4)H(SO_4)$ dimers. In this context, the proton conduction in the monoclinic **c** direction should be more pronounced than in **b**. Along the **a** direction, which shows the lowest conductivity, the distance between $(SO_4)H(SO_4)$ hydrogen bonds is the longest forming double layers of $(SO_4)H(SO_4)$ dimers which are again separated by double layers of $N2H_4$ groups.

The results of the conductivity measurements on TAHS in different crystallographic axes support the idea of possible pathways and mechanism of the proton conduction with respect to the crystal structure.

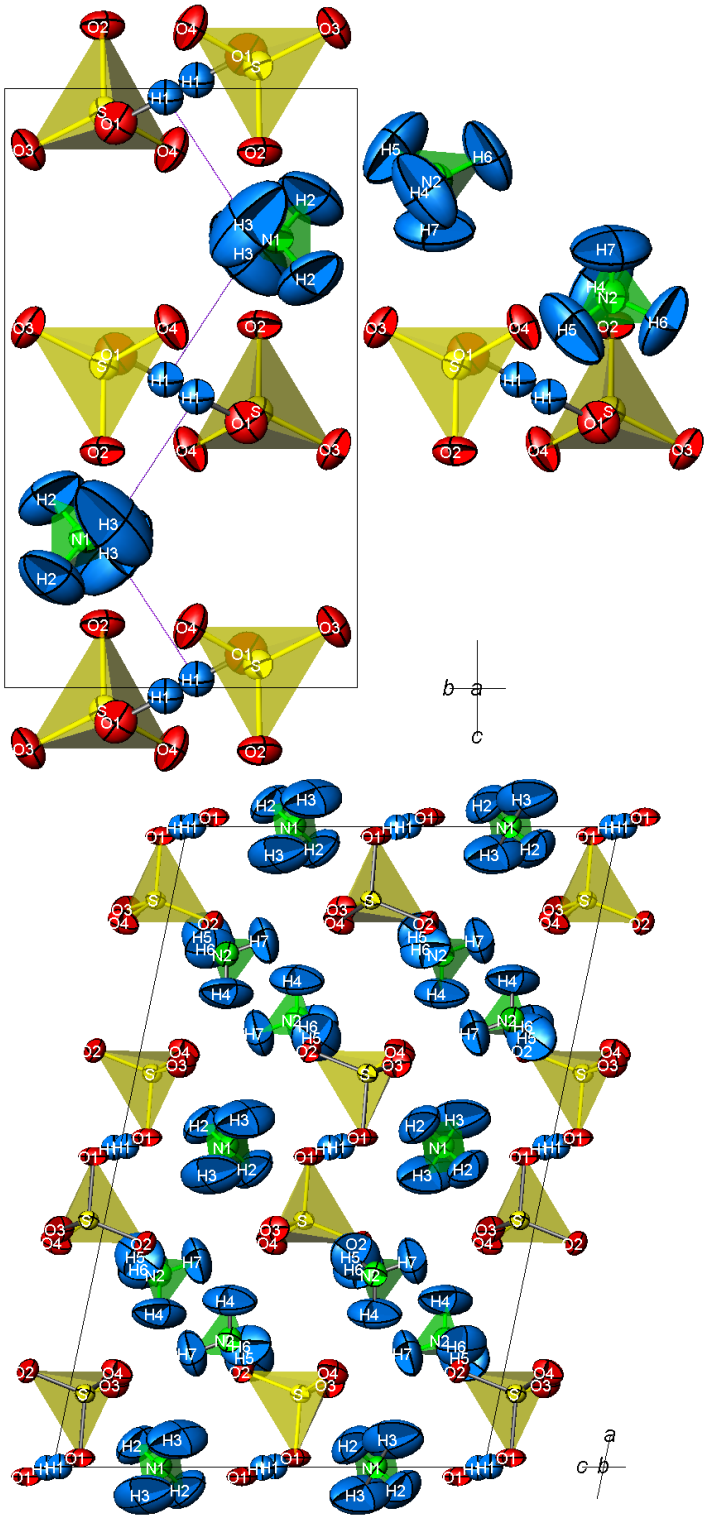

Figure 6.6: Possible pathways of proton conduction according to the different monoclinic directions. Some of the atoms are not illustrated for the simplification of the picture. Displacement ellipsoids are drawn at the 50 % probability level.

Chapter 7

Investigation on the reference system, $K_3H(SO_4)_2$

Analogical crystal structures are expected for TAHS and TKHS, according to the similar ionic radii of NH^+ (1.43 Å) and K^+ (1.38 Å). Especially at high temperatures, the NH^+ ion behaves like a spherical species corresponding to an almost free rotation. There exist many different statements concerning the high-temperature phase transition of TKHS as described in chapter 1. Therefore, corresponding measurements using DSC/TG and X-ray powder diffraction have been performed in the framework of this dissertation in order to verify the high-temperature phase transition of TKHS.

7.1 Differential scanning calorimetry/Thermogravimetry

The equivalent sample preparation method and experiment conditions as those for TAHS have also been applied for the DSC/TG measurements on TKHS. X-ray powder diffractograms were taken before and after each measurement for a detection of any changes in the sample. At the first heating cycle up to 548.0 (5) K, two endothermic signals were observed at 462.7 (5) and 493.4 (5) K, and the TG decreased a little at the second signal (Fig. 7.1). Afterwards, the sample was cooled down without delay and there were two exothermic signals with a continuous decrease of TG. The X-ray powder diffractograms before/after these DSC/TG measurements up to 548.0 (5) K are illustrated in Fig. 7.2. The two diffractograms are clearly different with many additional peaks after the heating cycle which can be attributed to K_2SO_4 and $K_2S_2O_7$. This result was caused by a thermal decomposition which took place at high temperatures, though the sample had not completely transformed yet and the TKHS-phase still exists.

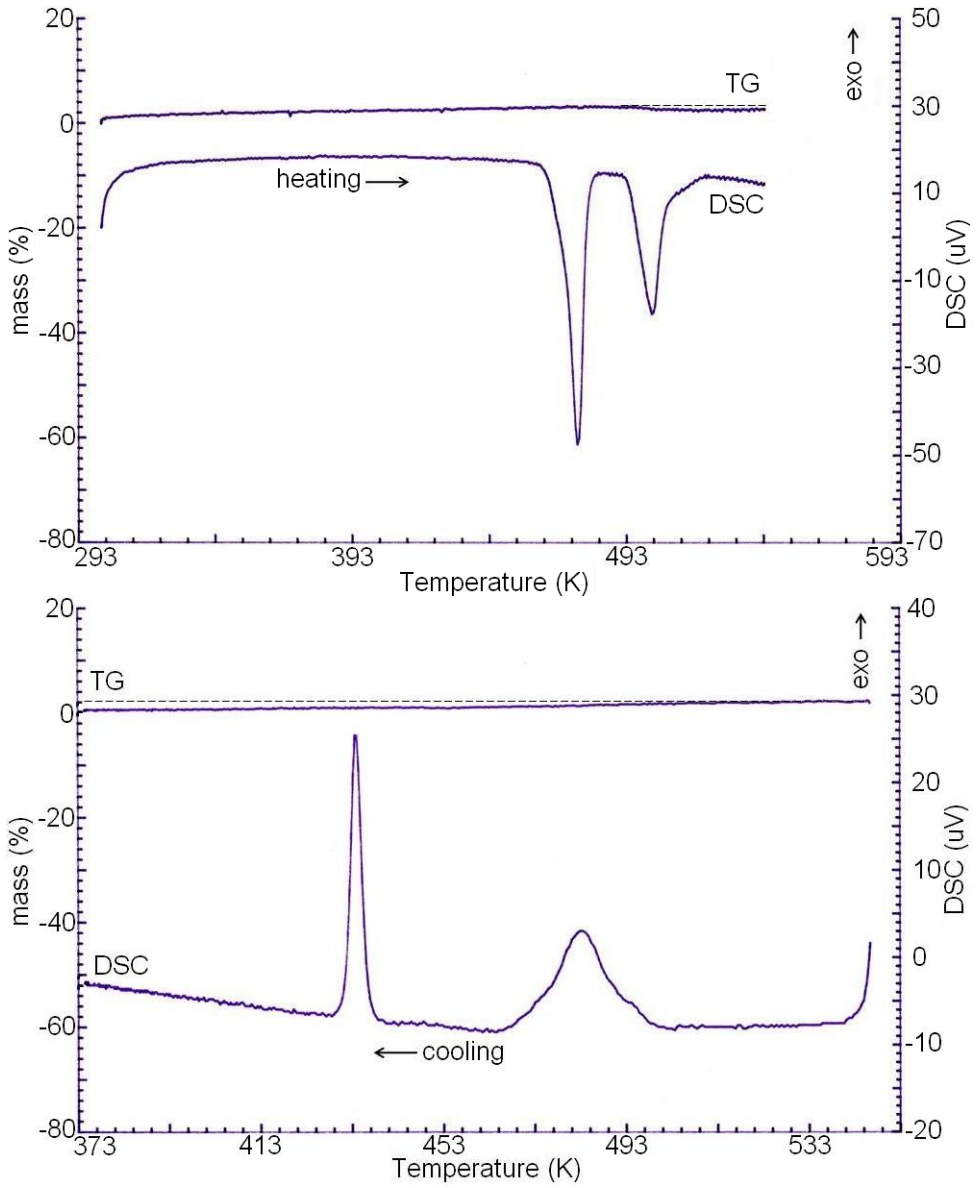

Figure 7.1: DSC/TG measurements of TKHS in the temperature range of RT – 548 K on heating and cooling.

In order to examine the final compounds produced from complete thermal decomposition of TKHS, a powder sample was annealed in a furnace at 553 K for three days and investigated afterwards by X-ray powder diffraction. This time, the sample was completely decomposed and only two phases, K_2SO_4 and $K_2S_2O_7$ could be identified. The thermal decomposition occurs with the following process:

$$2K_3H(SO_4)_2 \rightarrow 2K_2SO_4 + K_2S_2O_7 + H_2O$$

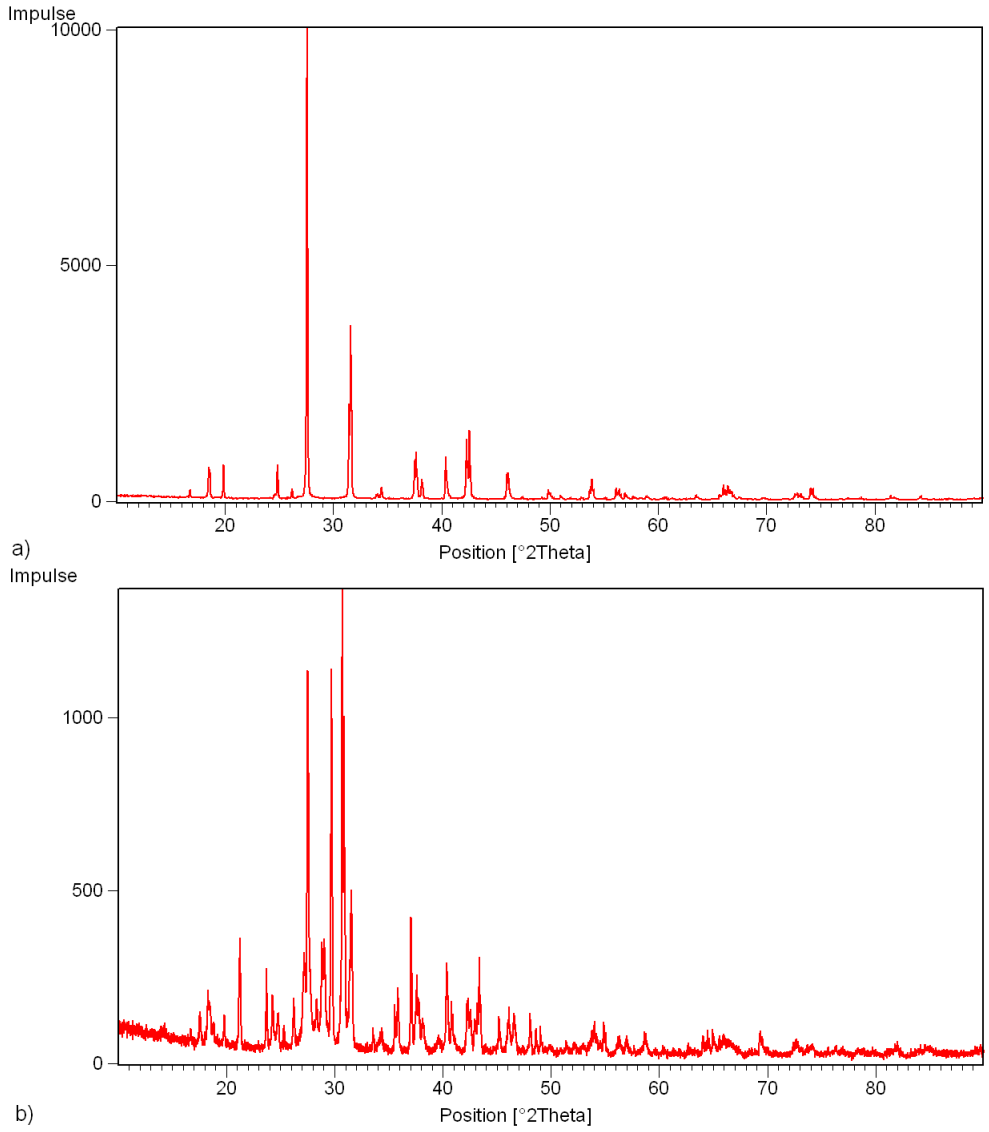

Figure 7.2: X-ray powder diffractograms of TKHS a) before and b) after the first DSC/TG measurements.

where H_2O evaporates during the thermal decomposition of TKHS. For the next DSC/TG experiment, the sample was heated only up to the temperature of the first signal (488 K) and then cooled down immediately. This time only one anomaly at 453.2 (5) K was observed on cooling (Fig. 7.3). In the subsequent X-ray powder measurements, an almost unchanged diffractogram was obtained except for a few very weak additional reflections which hardly raised from the background (Fig. 7.4). According to this, the first endothermic signal is supposed to be the signature of the high-temperature phase transition of TKHS, however, a slow beginning of thermal decomposition cannot be totally excluded. Those minor peaks observed in the powder diffractogram can be

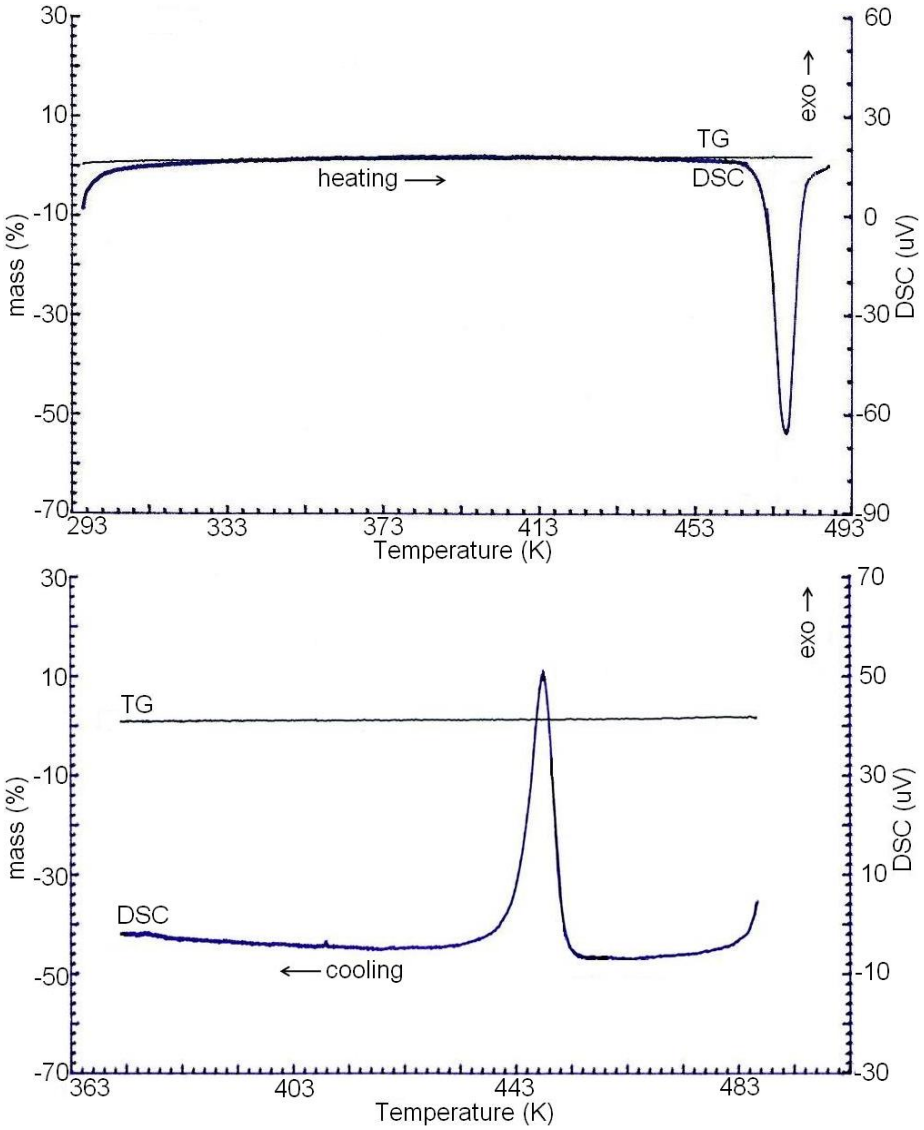

Figure 7.3: DSC/TG measurements of TKHS in the temperature range of RT – 488 K on heating and cooling.

attributed to $KHSO_4$ and K_2SO_4. These compounds are also possible products of the thermal decomposition of TKHS, though, the decomposition process is different from that described above. The presence of the component $KHSO_4$ can be derived from the following decomposition process:

$$K_3H(SO_4)_2 \rightarrow KHSO_4 + K_2SO_4$$

Since this process does not lose any fraction of components, there is no change in the TG line. When this sample was reheated again, a small additional anomaly below the assumed high-temperature phase transition temperature was detected, which reap-

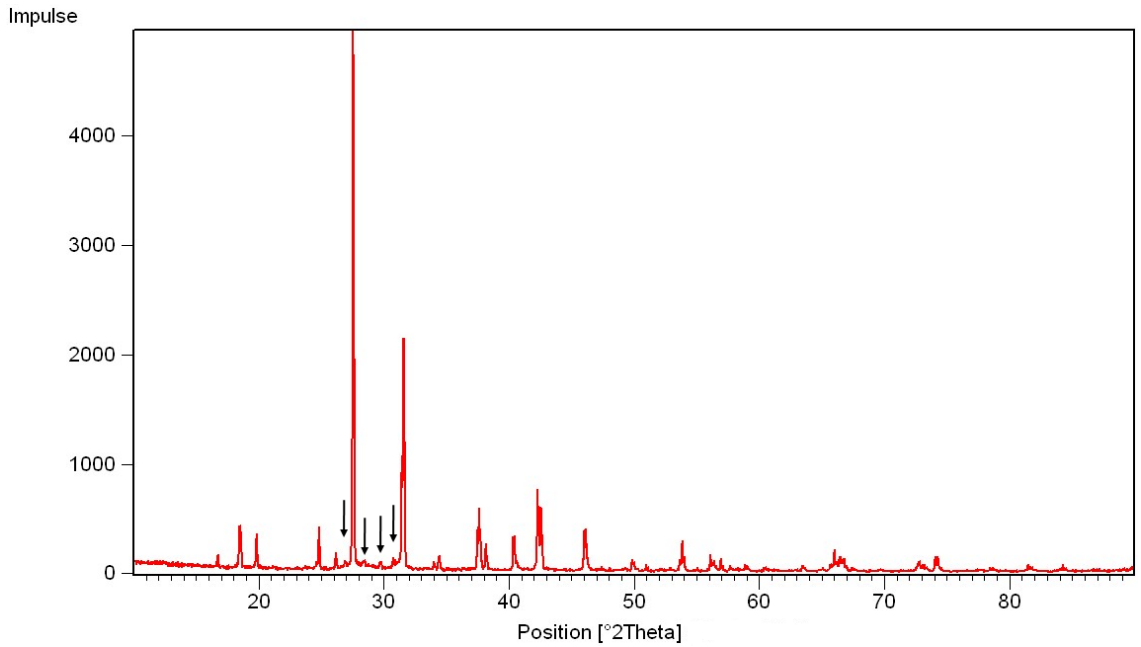

Figure 7.4: X-ray powder diffractograms of TKHS after the DSC/TG measurements up to 488 K. Minor additional peaks of $KHSO_4$ and K_2SO_4 are marked with arrows.

peared on cooling. From a separate DSC/TG measurement on $KHSO_4$, the additional signal was attributed to the phase transition temperature of this substance. Out of the DSC/TG measurements on TKHS the following steps in the thermal decomposition process could be verified:

$$K_3H(SO_4)_2 \rightarrow KHSO_4 + K_2SO_4$$
$$2KHSO_4 \rightarrow K_2S_2O_7 + H_2O$$

The slight decrease of TG at the second endothermic signal on heating can be therefore understood as loss of water. The X-ray powder diffractograms in each stage detected the relevant products of the decomposition. Hence, after the first decomposition step, no $K_2S_2O_7$ could be found and when the sample had reached higher temperatures the water evaporated from the sample and the next thermal decomposition step took place. This stepwise thermal decomposition was not observable with the annealing process where the sample stayed at higher temperatures for several days. In this case, only the final decomposition products could be detected with X-ray powder diffraction. Nevertheless, the first distinctive endothermic signal at ~ 463 K on heating and at ~ 453 K on cooling with almost the same sample quality indicates a possible high-temperature phase transition. This result was then further investigated with temperature-dependent X-ray powder diffraction measurements.

7.2 Temperature-dependent X-ray powder diffraction

The purpose of X-ray powder diffraction experiments was to verify the high-temperature phase transition of TKHS. In order to avoid the thermal decomposition the sample was heated up to 463 K in the first attempt. The powder sample ground in a glove box was mounted on a sample holder and the sample surface was covered with a thin Kapton foil. At 463 K, repeated scans were collected for several hours to observe any changes in the powder diffractograms. Additional peaks were firstly observed after almost four hours and these new reflections were attributed to the rhombohedral high-temperature phase of TKHS [44]. Through the multiphase Rietveld refinement, the ratio of the room- and high-temperature phases was determined, whereas with increasing measuring time the fraction of the high-temperature phase rose. The ratio of the RT-/HT-phases was approximately equal to 71%: 29% after $\sim$ 12 hours heating at constant 463 K (Fig. 7.5). For some reason, perhaps dependent on the temperature, the sample did not

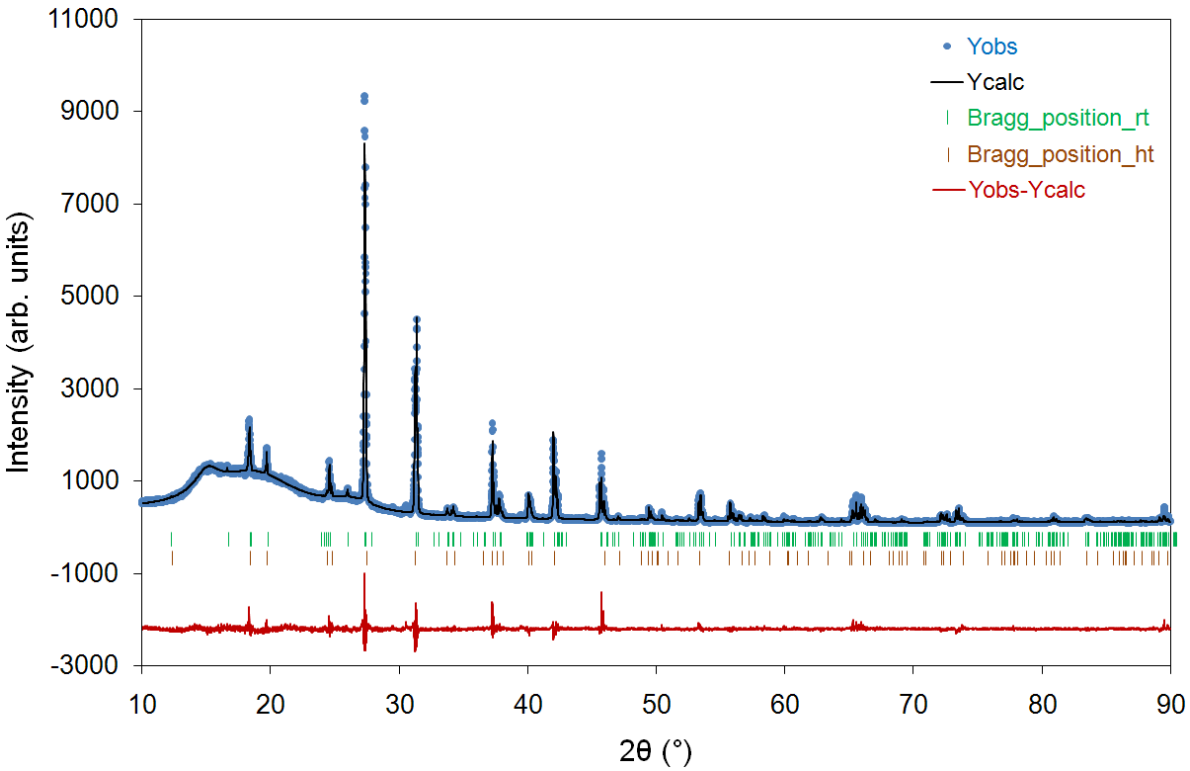

Figure 7.5: Rietveld refinement of X-ray powder diffraction data on TKHS after $\sim$ 12 hours at 463 K.

undergo the high-temperature phase transition completely and only a part of the sample changed to the rhombohedral high-temperature phase. On cooling, a smaller 2Θ

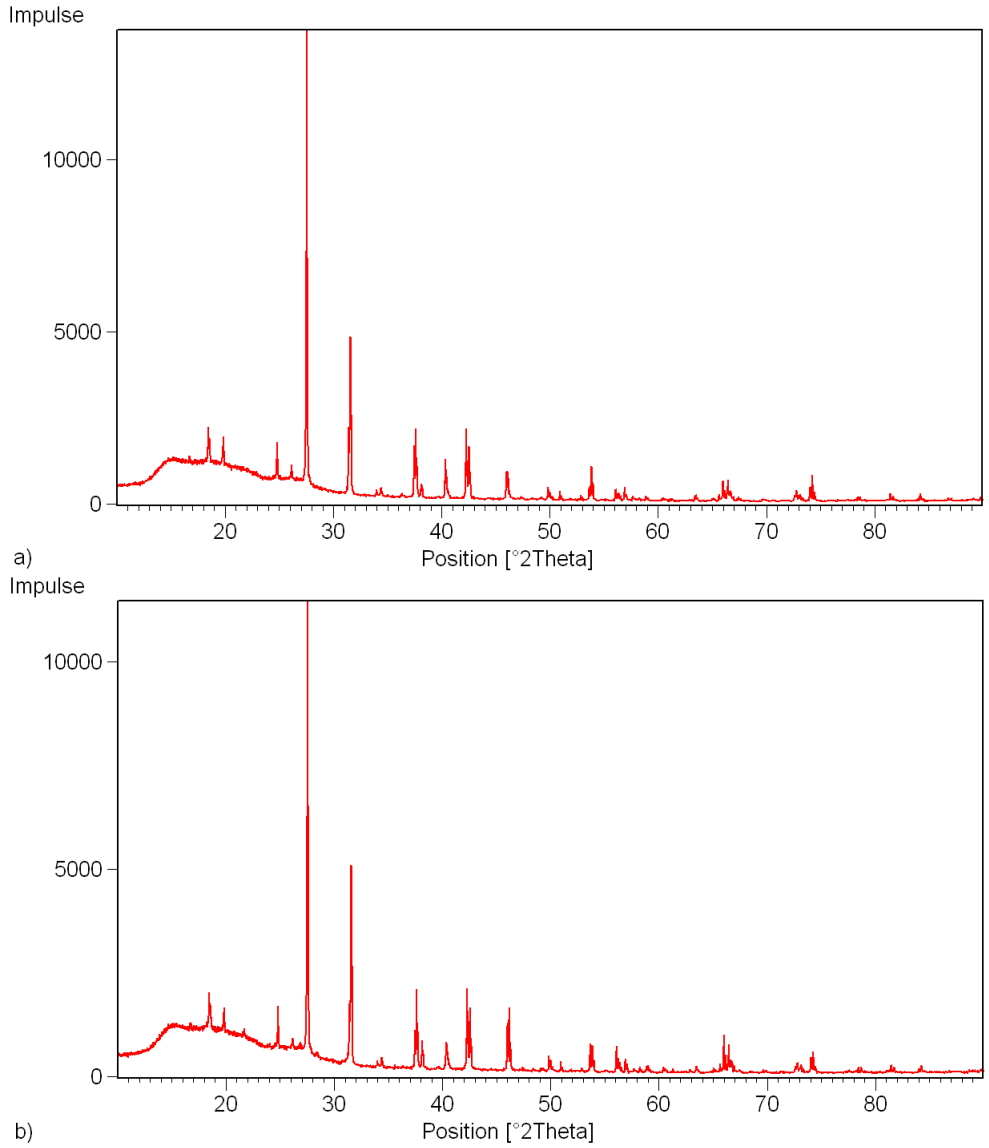

Figure 7.6: X-ray powder diffractograms of TKHS at room temperature a) before and b) after the first heating/cooling cycle up to 463 K.

range ($16° \leq 2\Theta \leq 32°$) was scanned. The fraction of the high-temperature phase decreased rather continuously with falling temperatures and the complete disappearance of the phase took place at $\sim$ 373 K. The fact that the rhombohedral phase of TKHS was observed over a very large temperature range on cooling may result from the fast cooling rate where there had not been enough time for the sample to fully alternate to the monoclinic room-temperature phase again. The measurement at room temperature after the first heating and cooling cycle did not indicate any distinctive changes of the sample quality as shown in Fig. 7.6. Assuming that the sample had already lost some

humidity at higher temperatures, the second heating cycle was performed without the Kapton foil. This time, the sample was brought to the temperature of 467 K, and repeated scans were collected for several hours at constant temperature. Although, the amount of the HT-phase was increased to $\sim$ 43 %, the monoclinic RT-phase still coexisted at this temperature. Thereafter, the sample was successively heated up to 479 K. On heating the HT-phase gained in intensity to some extent, however, the RT-phase did not completely vanish. At the same time, the decomposition products (K_2SO_4 and $K_2S_2O_7$) increased correspondingly with rising temperatures. As the peak intensities of the decomposition phases had grown considerably, the sample was cooled down again. The control-measurement at room temperature was not reversible any more and the thermal decomposition of the TKHS sample did occur parallel to the high-temperature phase transition.

From the DSC/TG and X-ray powder diffraction measurements, the appearance of the high-temperature phase transition of TKHS could be observed starting at $\sim$ 463 K. This phase transition is accompanied by the thermal decomposition of the sample, which developed slower than the HT-phase transition below 473 K. The observed phase transition from monoclinic to rhombohedral did not occur completely throughout the powder sample. Hence, only a part of the sample underwent the HT-phase transition. This phenomenon was also reported earlier using polarizing microscope [18], where only a few areas of the sample remained uniaxial under crossed nicoles at high temperatures and built twin domains on cooling. The HT-phase transition of TKHS seems to be a kinetic one, so that a longer heating time at a constant temperature brought a larger amount of the high-temperature phase to a certain extent. However, the temperature had to be increased when no changes were visible any more in the powder diffractograms. This, on the other hand, speeded up the thermal decomposition of the sample. Therefore, with the measurement conditions performed in this dissertation, no complete phase transformation of TKHS could be observed.

Chapter 8

Conclusion

$(NH_4)_3H(SO_4)_2$ (TAHS) is well known for five successive phase transitions and shows extremely high proton conductivity at high temperature above 413 K. The crystal structure analysis of TAHS was carried out regarding the hydrogen ordering which plays a significant role for the structural phase transitions. First of all, single crystals of TAHS were grown from aqueous solution for X-ray and neutron diffraction. Well defined sample quality was needed for the envisaged experiments to obtain reproducible results. Since humidity influences the sample quality and thus the results of experiments, polycrystalline samples were prepared in a glove box. For the neutron single-crystal measurements at high temperature, a cracking of single-crystal samples was observed during test experiments. To overcome this strain-induced phenomenon, a twinned sample at room temperature was used and slowly heated towards the high-temperature phase transition. At the phase transition, the twinned sample became monodomained, and single-crystal neutron diffraction data could be collected with this sample. Using DSC/TG measurements as well as the temperature-dependent X-ray powder diffraction, the high-temperature phase transition was confirmed and the thermal decomposition of the sample could be verified. It was important to exclude thermal decomposition of the sample in the high-temperature phase for structure analysis and conductivity measurements, since there has been certain ambiguity in reported results throughout the literature.

The phase transition temperatures were defined on cooling and heating using X-ray powder diffraction. A clear hysteresis as well as a sudden change in the lattice parameter developments was observed at the first-order phase transitions (I/II, IV/V and V/VII). On the other hand, the II/III- and III/IV-phase transitions with rather continuous changes of reflection intensities and lattice parameters at the phase transition were

characterized as being of second-order.

The crystal structure analysis of $(NH_4)_3H(SO_4)_2$ (TAHS) was performed for the different phases using single-crystal X-ray and neutron diffraction. The envisaged advantage of neutron diffraction was to obtain precise locations of the protons and to describe their thermal behaviour more accurately, since H-disorder plays an important role in the rich polymorphism of TAHS. Using neutron diffraction, the important effect of H-ordering for the different phases could be investigated in detail. The characteristic O–H–O hydrogen bonds between two SO_4 tetrahedral groups are symmetric in high- and room-temperature phases and become asymmetric in the other phases. A split-atom model was used for the H-atom positions in the O–H–O bonds and an increase of ordering was found with decreasing temperature. The temperature-dependent thermal ellipsoids of H atoms in the O–H–O bonding indicate a dynamic hydrogen disorder. Moreover, a successive ordering of different ammonium groups with decreasing temperature was observed, on the basis of changes in their thermal ellipsoids as well as by a rigid-body analysis. The orientational ordering basically shows an altered situation of N–H$\cdots$O hydrogen bonds in different phases. Whereas bifurcated, thus competing hydrogen bonds are formed between NH_4 and SO_4 at room- and high-temperature phases, shorter, hence stronger, single bonds are dominant at low temperatures.

The high-temperature phase I that is known for superprotonic conductivity [12, 13], has rhombohedral space group $R\bar{3}m$ above 413 K. According to the disordering of the O atom in the SO_4–H–SO_4 hydrogen bond, a two-dimensional pseudo-hexagonal O–H–O network is formed in the (001) plane. A difference Fourier map suggested a splitting of O- and H-atom positions in the O–H–O hydrogen bond and hence, a split-atom model was used in the refinement. The split H-atom positions are not fully occupied, enabling proton diffusion in the network. Supporting the idea of proton diffusion between ammonium groups and the O–H–O hydrogen bonds [14], almost the same atomic distances were found for the H atoms between neighbouring O–H–O hydrogen bonds (2.27 (2) Å) and for the H atoms between the ammonium groups and the hydrogen bonds (2.26 (1) Å). A nuclear density map around $N1H_4$ was presented, with different z-parameters for a visualization of this possible supplementary proton exchange. In the high-temperature phase, the ammonium groups are located on special positions with high site symmetries ($\bar{3}m$ and $3m$). Considering the strongly enlarged anisotropic mean-square displacements of H atoms, both ammonium groups were refined using a split-atom model. The split H-atom positions are only partially occupied, and hence, a reorientational movement of the ammonium groups is suggested. Their translational

and librational motional behaviour was analysed using a rigid-body model. The $N1H_4$ group moves almost isotropically, being at the centre of the pseudo-hexagonal network of the O–H–O hydrogen bonds. On the other hand, the $N2H_4$ groups form a double layer perpendicular to the **c** direction, and show an anisotropic motional behaviour (stronger in **a**/**b** directions). Throughout the whole unit cell, the ammonium groups and SO_4 groups are linked by sharing the same O atoms forming N–H···O hydrogen bonds.

The crystal structure of the room-temperature phase II is monoclinic, $C2/c$. While a two-dimensional hydrogen bond network is formed in the high-temperature phase, isolated $(SO_4)H(SO_4)$ dimers are characteristic for phase II. Using single-crystal neutron diffraction, the H atoms on an inversion centre in the middle of the dimer are refined with a split-atom model. As a result, two potential minima with 1/2 site occupancy factor are found in the symmetric O–H–O bond. The two symmetrically independent NH_4 groups exhibit well localized N atoms (small and almost isotropic displacement ellipsoids) with disordered H atoms (large anisotropic displacement ellipsoids). Taking into account its environment, the $N1H_4$ group on a special position (twofold axis) was described with a split-atom model. The splitting of H-atom positions around N1 gives rise to single N–H···O hydrogen bonds instead of the bifurcated ones. In the case of the $N2H_4$ groups on a general position, there are equally distributed O atoms in the vicinity, and hence, competing N–H···O hydrogen bonds are formed. The rigid-body analysis showed distinct librational motion of $N1H_4$ around the **a**-axis (towards the bifurcated N–H···O hydrogen bonds).

In the low-temperature phase III between 265 and 141 K, TAHS has the primitive monoclinic space group $P2/n$. Crystal structure analysis in this phase was carried out with respect to the proton ordering. Hence, the site occupancy of the split H-atom positions in the $(SO_4)H(SO_4)$ dimer was refined assuming an order-disorder II/III-phase transition. As a result, an increase of H-ordering was found with decreasing temperature. Moreover, the ammonium groups on general positions begin to "freeze" in this phase, showing a clear decrease in their displacement ellipsoids. Whereas there were equivalent bifurcated N–H···O hydrogen bonds at room temperature, stronger single bonds are formed in phase III. Besides, the ammonium groups on special positions showed almost unchanged large displacement ellipsoids, still having rather competing N–H···O hydrogen bonds with surrounding O atoms. However, as temperature decreases, weaker bonds get weaker and stronger bonds even stronger, indicating a possible "freezing" of these ammonium groups at lower temperatures. The additional

rigid-body analysis confirmed a clear decrease in librational motion for the ammonium groups on general positions.

Below 141 K, TAHS-IV exists in a relatively small temperature range. Using single-crystal X-ray diffraction with an image-plate detector (STOE-IPDS II), additional reflections (0 $^{k}/_{2}$ 0) were found, and hence, a doubling of the unit cell in **b** direction was suggested. The complete dataset obtained by single-crystal neutron diffraction was then analysed with respect to the doubling of the unit cell. Since the superstructure reflections showed weak intensities, some restraints were made in the structure refinement. As a result, slightly reoriented SO_4 and NH_4 groups were observed along the **b** direction. In the case of NH_4 groups, shorter N–H$\cdots$O hydrogen bonds were found with respect to phase III. Therefore, an increase of H-ordering with decreasing temperature could also be confirmed for phase IV.

The crystal structure of TAHS in phase V between 133 and 70 K (on cooling) is triclinic, $P\bar{1}$. In the triclinic unit cell, all the ammonium groups are located on general positions, and they seemed to be completely ordered in their orientation. Furthermore, no indication of H-disorder in the asymmetric O–H$\cdots$O bond was found, though, the precision of the H distribution was limited to some extent, using X-ray diffraction only.

The conductivity measurements were carried out along the three monoclinic basis vectors on TAHS with an impedance spectrometer. The results show an anisotropy of conduction in the monoclinic room-temperature phase and a high proton conduction ($\sigma \sim 10^{-2}$ S $\cdot$ cm^{-1}) in the (001) plane in the high-temperature phase I. The pseudo-hexagonal hydrogen bond network in the (001) plane, with only partially occupied H-atom positions, allows for proton diffusion in the plane. Furthermore, the idea of supplementary proton conduction through the ammonium groups in the middle of the pseudo-hexagonal network was supported by the short distance between two H atoms and by the nuclear density map around these involved ammonium groups.

For the reference system $K_3H(SO_4)_2$ (TKHS), the existence of the rhombohedral high-temperature phase was confirmed by X-ray powder diffraction. However, the high-temperature phase transition shows a pronounced transition kinetics and, at the same time, is accompanied by thermal decomposition.

References

[1] Baranov, A. I. *Crystallography Reports* **48**, 1012–1037 (2003).

[2] Gesi, K. *Phys. Status Solidi* (A)**33**, 479–482 (1976).

[3] Gesi, K. *Jpn. J. Appl. Phys* **19**, 1051–1053 (1980).

[4] Osaka, T., Makita, Y., and Gesi, K. *J. Phys. Soc. Jpn.* **49**, 593–598 (1980).

[5] Gesi, K. and Ozawa, K. *J. Phys. Soc. Jpn.* **43**, 570–574 (1977).

[6] Gesi, K. *J. Phys. Soc. Jpn.* **43**, 1941–1948 (1977).

[7] Swain, D. and Guru Row, T. N. *Inorg. Chem.* **46**, 4411–4421 (2007).

[8] Dominiak, P. M., Herold, J., Kolodziejski, W., and Woźniak, K. *Inorg. Chem.* **42**, 1590–1598 (2003).

[9] Friese, K., Aroyo, M. I., Schwalowsky, L., Adiwidjyjy, G., and Bismayer, U. *J. Solid State Chem.* **165**, 136–147 (2002).

[10] Sohn, Y. J. *Strukturelle Untersuchungen des Hochtemperaturphasenübergangs von Triammoniumhydrogendisulfat ($(NH_4)_3H(SO_4)_2$)* , Diplomarbeit, Institut für Kristallographie, RWTH Aachen University (2007).

[11] Hahn, T. *International Tables for Crystallography* , Vol. A. Dordrecht: Kluwer Academic Publishers. (2002).

[12] Schwalowsky, L., Vinnichenko, V., Baranov, A., Bismayer, U., Merinov, B., and Eckold, G. *J. Phys. Condens. Matter* **10**, 3019–3027 (1998).

[13] Chen, R. H., Chen, T. M., and Shern, C. S. *J. Phys. Chem. Solids* **61**, 1399–1406 (2000).

[14] Fechtelkord, M., Engelhardt, A., Buhl, J. C., Schwalowsky, L., and Bismayer, U. *Solid State Nuclear Magnetic Resonance* **17**, 76–88 (2000).

[15] Merinov, B., Bourenkov, G., and Bismayer, U. *Phys. Status Solidi* (B)**218**, 365–378 (2000).

[16] Fukami, T., Tobaru, K., Kaneda, K., Nakasone, K., and Furukawa, K. *J. Phys. Soc. Jpn.* **63**, 2006–2007 (1994).

[17] Smirnov, L. S., Baranov, A. I., Shuvalov, L. A., Bobrowicz-Sarga, L., Natkaniec, I., and Waplak, S. *Phys. Solid State* **43**, 115–123 (2001).

[18] Gossner, B. *Zeitschr. f. Kr.* **38**, 110–168 (1904).

[19] Chisholm, C. R. I. and Haile, S. M. *Solid State Ionics* **145**, 179–184 (2001).

[20] Matsuo, Y., Hatori, J., Nakashima, Y., and Ikehata, S. *Solid State Communications* **130**, 269–274 (2004).

[21] Chen, R. H., Chang, R. Y., Shern, C. S., and Fukami, T. *J. Phys. Chem. Solids* **64**, 553–563 (2003).

[22] Novacović, L., Dojčilović, J., Spasović, S., and Nikolić, A. S. *XVI National Symposium on Condensed Matter Physics, Sokobanja* (2004).

[23] Lim, A. R., Jang, T. G., Chang, J. H., and Jeong, S. Y. *J. Phys. Soc. Jpn.* **73**, 2863–2867 (2004).

[24] Makarova, I. P., Chernaya, T. S., Filaretov, A. A., Vasil'ev, A. L., Verin, I. A., Grebenev, V. V., and Dolbinina, V. V. *Crystallography Reports* **55**, 393–403 (2010).

[25] Baranov, A. I., Grebenev, V. V., Bismayer, U., and Ludwig, J. *Ferroelectrics* **369**, 108–116 (2008).

[26] Noda, Y., Uchiyama, S., Kafuku, K., Kasatani, H., and Terauchi, H. *J. Phys. Soc. Jpn.* **59**, 2804–2810 (1990).

[27] Noda, Y. *J. Korean. Phys. Soc.* **27**, S156–S160 (1994).

[28] Noda, Y., Kasatani, H., Watanabe, Y., and Terauchi, H. *J. Phys. Soc. Jpn.* **61**, 905–915 (1992).

[29] Furuta, H., Endo, S., Kobayashi, M., Watanabe, J., Kasahara, M., and Yagi, T. *Ferroelectrics* **242**, 37–45 (2000).

[30] Sohn, Y. J., Loose, A., Merz, M., Sparta, K., Klapper, H., and Heger, G. *Acta Cryst.* B**65**, 36–44 (2009).

[31] *X-AREA* , Stoe & Cie GmbH, Germany (2003).

[32] Sheldrick, G. M. *Acta Cryst.* A**64**, 112–122 (2008).

[33] Rodriguez-Carvajal, J. *CPD Newsl.* **26**, 12–19 (2001).

[34] Heger, G., Mullen, D., and Knorr, K. *Phys. Status Solidi* (A)**31**, 455–462 (1975).

[35] Scherf, C. *PRON* , Revised Stoe version. Institute of crystallography, Aachen, Germany (1998).

[36] Petricek, V., Dusek, M., and Palatinus, L. *JANA2006* , The crystallographic computing system. Institute of Physics, Praha, Czech Rebuplic (2006).

[37] Becker, P. J. and Coppens, P. *Acta Cryst* A**30**, 129–147 (1974).

[38] Zachariasen, W. H. *Acta Cryst.* **23**, 558–564 (1967).

[39] Schomaker, V. and Trueblood, K. N. *Acta Cryst.* B**24**, 63–76 (1968).

[40] Fechtelkord, M., Diekmann, A., and Bismayer, U. *American Mineralogist* **92**, 1821–1826 (2007).

[41] Tamura, I., Noda, Y., and Morii, Y. *J. Phys. Chem. Solids* **60**, 1411–1414 (1999).

[42] Jennissen, H. D. *Phasenumwandlungen und Defektstrukturen in Kristallen mit tetraedrischen Baugruppen* , Dissertation, RWTH Aachen University (1990).

[43] Burla, M. C., Camalli, M., Carrozzini, B., Cascarano, G. L., Giacovazzo, C., Polidori, G., and Spagna, R. *J. Appl. Cryst.* **36**, 1103 (2003).

[44] Makarova, I. P., Chernaya, T. S., Verin, I. A., Simonov, A. A., Grebenev, V. V., and Dolbinina, V. V. *Phys. Solid State* **51**, 1431–1434 (2009).

Lebenslauf

Persönliche Angaben

Name	Yoo Jung Sohn
Geburtsdatum	12. Februar 1977
Geburtsort	Seoul
Staatsangehörigkeit	koreanisch
Familienstand	verheiratet, zwei Kinder

Schulbildung

1983 – 1989	Grundschule Gwacheon, Südkorea
1989 – 1992	Mittelstufe Gwacheon, Südkorea
1992 – 1995	Gymnasium Oberursel (Taunus)
1995 – 1997	Oberstufe Gwacheon, Südkorea mit Abitur

Studium

1997 – 2002	Studium an der Korea University Bachelor of Science, Schwerpunkt Earth and Environmental Sciences
2000	Sprachaufenthalt in Eastbourne, England
2002 – 2007	Studium der Mineralogie an der RWTH Aachen mit Diplomabschluss

Promotionsstudium und berufliche Tätigkeiten

2007 – 2011	Promotionsstudium am Institut für Kristallographie der RWTH Aachen
2007 – 2009	Wissenschaftliche Mitarbeiterin im Institut für Kristallographie der RWTH Aachen
2009 – 2011	Stipendiatin der RWTH Graduiertenförderung
seit April 2011	Wissenschaftliche Mitarbeiterin im Institut für Kristallographie der RWTH Aachen